UNIVERSITY OF CALIFORNIA, SAN DIEGO

Metallic Nanotexturing via RF Plasma Processing for Advanced Biomedical Devices: Antibiofouling Neural Electrodes and Hybrid Drug-Eluting Bare-Metal Stents

A dissertation submitted in partial satisfaction of the
requirements for the degree Doctor of Philosophy

in

Engineering Sciences (Engineering Physics)

by

Calvin James Gardner

Committee in Charge:

Professor Sungho Jin, Chair
Professor Renkun Chen, Co-Chair
Professor Ratneshwar Lal
Professor Zhaowei Liu
Professor Yu Qiao

2015

The Dissertation of Calvin James Gardner is approved, and it is acceptable in quality and form for publication on microfilm and electronically:

_____

_____

_____

_____
Co-Chair

_____
Chair

University of California, San Diego

2015

DEDICATION

This work is dedicated to

my wife Emma

&

our son Sawyer.

Thank you for making this journey such an enjoyable adventure.

I love you.

EPIGRAPH

It is the man of science,
eager to have his every opinion regenerated,
his every idea rationalized,
by drinking at the fountain of fact,
and devoting all the energies of his life to the cult of truth,
not as he understands it,
but as he does not yet understand it,
that ought properly to be called a philosopher.

Charles Sanders Peirce

TABLE OF CONTENTS

LIST OF FIGURES

LIST OF TABLES

ACKNOWLEDGEMENTS

I sincerely express my gratitude to my advisor, Professor Sungho Jin, for his guidance, support, and mentorship throughout my time at UCSD. I thank my committee co-chair, Professor Renkun Chen, and committee members, Professor Ratneshwar Lal, Professor Zhaowei Liu, and Professor Yu Qiao for their willingness to guide and assess my dissertation work.

I gratefully acknowledge fellow members of Professor Jin's lab group past and present for their support and friendship. I thank Leon Chen for his training and advice on myriad research projects; Mariana Loya for her initial work on RF Plasma texturing of MP35N which enabled so much of this work; Edward Choi for his assistance with sample preparation; Jonathan Trisnadi for his assistance with sample preparation and impedance characterization; Karla Brammer, Laura Connelly, and Gary Johnston for their help with cell culture and viability tests; Jennifer He for her assistance with stent sample preparation and drug delivery measurements; Stanley Kim for help with materials; Justin Kim and Cyrus Rustomji for their expertise in electrode impedance measurements; Jeanne Khamwannah for electrochemical sharpening of MP35N; Isaac Liu and Sarah Zong for microscopy on textured copper; Young Jin Kim for his assistance in prototyping, and every other member of the group for discussion and ideas. I also am grateful to Professor Lina Reiss and the Oregon Hearing Research Center for collaboration on in vivo antibiofouling cochlear implants.

I am thankful for the opportunity to work with and learn from many other people on the UCSD campus including the Nano3 cleanroom personnel for their

training and assistance in sample processing and characterization techniques; MAE staff for their assistance in graduation procedures, material orders, financial work, and all the other work they do; the CRMS crew for their precision and alacrity in finishing any order I submitted; and everyone else who assists the progression of research at UCSD.

I would also like to thank those who provided financial support for my graduate studies including the National Defense Science and Engineering Graduate Fellowship; the Iwama Fund at UC San Diego; the National Science Foundation through Grant No. DMR-1006081; and the Navy STTR program. I am also appreciative of the opportunity to collaborate with Carl Edwards and team at Space Micro Inc.

Chapters 2, 3, and 4, in part, are reproduced or adapted from material as it appears in Acta Biomaterialia, "Controlled Metallic Nanopillars for Low Impedance Biomedical Electrode" Volume 10, Issue 5, Pages 2296-2303 (May 2014). Jonathan Trisnadi, Tae Kyoung Kim, Karla Brammer, Lina Reiss, Li-han Chen, and Sungho Jin are co-authors. The dissertation author was the primary investigator and author of this paper.

Chapters 4, in part and 5, in full, are adaptations of material being prepared for publication as "Antibiofouling Neural Electrodes by RF-Plasma Nanotexturing and Selective Hydrophobic Coating" with intended submission to Acta Biomaterialia. Laura Connelly, Chulmin Choi, Sungho Jin, and Renkun Chen are co-authors. The dissertation author is primary investigator and author of this material.

Chapter 6, in full, is from material being prepared for publication as "Extended Release of Paclitaxel and Sirolimus from Bare-Metal Stent Surface by RF-Plasma Nanotexturing and Subsequent Deformation" with intended submission to the Journal of Controlled Release. Jennifer He, Gary W. Johnston, Sungho Jin, and Renkun Chen are co-authors. The dissertation author is the primary investigator and author of this material.

Finally, I am tremendously grateful to my family and friends for their constant and ongoing encouragement and support. I could never thank you enough.

VITA

2010 Bachelor of Science, Mechanical Engineering, emphasis Materials Science
Additional Major: Applied Physics, emphasis Mechanics
Additional Major: Philosophy, emphasis Logic
Minor: Mathematics
Brigham Young University

2011 Master of Science, Engineering Sciences (Engineering Physics)
University of California, San Diego

2014 Candidate of Philosophy, Engineering Sciences (Engineering Physics)
University of California, San Diego

2015 Doctor of Philosophy, Engineering Sciences (Engineering Physics)
University of California, San Diego

PUBLICATIONS

Calvin J. Gardner, Laura Connelly, Chulmin Choi, Sungho Jin, and Renkun Chen. "Antibiofouling Neural Electrodes by RF-Plasma Nanotexturing and Selective Hydrophobic Coating," Acta Biomaterialia. (Preparing for submission April 2015)

Calvin J. Gardner, Jennifer He, Gary W. Johnston, Sungho Jin, and Renkun Chen. "Extended Release of Paclitaxel and Sirolimus from Bare-Metal Stent Surface by RF-Plasma Nanotexturing and Subsequent Deformation," Journal of Controlled Release. (Preparing for submission April 2015)

Ying Zhong, Fenghua Zhang, Calvin J. Gardner, Gunwoo Kim, Jinsong Leng, Chunqing Wang, Renkun Chen, and Sungho Jin. "Humidity-Sensitive Smart Textiles Augment Personal Thermoregulation to Reduce HVAC Energy Consumption," Advanced Energy Materials. (Preparing for submission April 2015)

Tae Kyoung Kim, Jaeyun Moon, Bryan VanSaders, Dongwon Chun, Calvin J. Gardner, Jae-Young Jung, Gang Wang, Renkun Chen, Zhaowei Liu, Yu Qiao, and Sungho Jin. "Si boride-coated Si nanoparticles with improved thermal oxidation resistance," Nano Energy 9 (2014), 32-40.

Calvin J. Gardner, Jonathan Trisnadi, Tae Kyoung Kim, Karla Brammer, Lina Reiss, Li-han Chen, and Sungho Jin. "Controlled Metallic Nanopillars for Low Impedance Biomedical Electrode," Acta Biomaterialia 10:5 (2014), 2296-2303.

Hyunsu Kim, Jirapon Khamwannah, Chulmin Choi, Calvin J. Gardner, and Sungho Jin. "Formation of 8nm TiO2 nanotubes on a three dimensional electrode for enhanced photoelectrochemical reaction," Nano Energy, 2:6 (2013), 1347-1353.

John A. Basinger, Caroline Sorensen, Calvin J. Gardner, David T. Fullwood, and Brent L. Adams. "Pattern Center Sensitivity in High Resolution Electron Backscatter Diffraction," Metallurgical and Materials Transactions A - David Field Symposium Special Edition (2013).

Hyunsu Kim, Jongjin Park, Kunbae Noh, Calvin J. Gardner, Seong Deok Kong, Jongmin Kim, and Sungho Jin. "An X-Y Addressable Matrix Odor-Releasing System Using an On-Off Switchable Device," Angewandte Chemie, 123 (2011), 1-6.

Calvin J. Gardner, Josh Kacher, John Basinger, Brent L. Adams, Muin S. Oztop, and Jeffrey W. Kysar. “Techniques and Applications of the Simulated Pattern Adaptation of Wilkinson’s Method for Advanced Microstructure Analysis and Characterization of Plastic Deformation,” Experimental Mechanics, 51:8 (2010), 1379-1393.

Calvin J. Gardner, Brent L. Adams, John A. Basinger, and David T. Fullwood. “EBSD-based Continuum Dislocation Microscopy,” International Journal of Plasticity, 26 (2010), 1234-1247.

Brent L. Adams, Calvin J. Gardner, and David T. Fullwood. “EBSD-based Dislocation Microscopy,” Solid State Phenomena, 160 (2010), 3-10.

Oliver K. Johnson, Calvin J. Gardner, David T. Fullwood, Brent L. Adams, Nathan Hansen, and George Hansen. “The Colossal Piezoresistive Effect in Nickel Nanostrand Polymer Composites and a Quantum Tunneling Model,” Computers, Materials and Continua, 15 (2010), 87-112.

Oliver K. Johnson, Calvin J. Gardner, Daniel B. Seegmiller, Nathan A. Mara, Andrew M. Dattelbaum, Phillip J. Rae, George C. Kaschner, Thomas A. Mason, and David T. Fullwood. “Multiscale Model for the Extreme Piezoresistivity in Silicone/Nickel Nanostrand Nanocomposites,” Metallurgical and Materials Transactions A, 42:13 (2010), 3898-3906.

Oliver K. Johnson, Calvin J. Gardner, David T. Fullwood, Brent L. Adams, and George Hansen. "Deciphering the Structure of Nano-Nickel Composites,” Los Alamos National Laboratory Public Release, SAMPE, 54 (2009).

PATENTS AND TECHNOLOGY DISCLOSURES

Sungho Jin, Calvin J. Gardner, and Stewart Matthew. "Article Comprising Improved Switchable Scent, Vapor and Liquid Release and Delivery Systems, and Methods and Applications Thereof." (UCSD Docket No. SD2015-240)

Sungho Jin, Calvin J. Gardner, Ying Zhong, and Gunwoo Kim. "Thermally Adaptive Textile." (UCSD Docket No. SD2015-125)

Calvin J. Gardner, Laura Connelly, Sungho Jin, and Lina Reiss. "Anti-Biofouling, Low-Impedance Electrodes for Implants including Neural Devices, Method of." (UCSD Docket No. SD2014-124)

Steven Foerster and Calvin J. Gardner. "A Minimal Knowledge Online Communications Network and Economy." (2014 App. 61971494)

Sungho Jin, Calvin J. Gardner, and Stewart Matthew. "Scalable, Rapidly Switchable Gas and Liquid Release and Delivery Apparati, Methods for Making, and Applications Thereof." (UCSD Docket No. SD2013-269) (PCT/US14/035054)

Calvin J. Gardner and Sungho Jin. "Article comprising Self-Healing and Solidifying Conducting Lines, Method Thereof." (UCSD Docket No. SD2012-223)

PRESENTATIONS

Calvin J. Gardner, Isaac Liu, Young Jin Kim, Edward Choi, Leon Chen, and Sungho Jin. "Adding Another Dimension to Communication and Entertainment Technologies," CMRR Research Review 2014: San Diego, California.

Carl Edwards, Calvin J. Gardner, Cyrus Rustomji, and Sungho Jin. "Nanofabricated Electronic Components," IMAPS 2014: San Diego, California.

David Strobel, Carl Edwards, and Calvin J. Gardner. "New Process for Space Qualified Electronic Components," in Outbrief: SBIR Phase II Project at Space Micro, 2013: San Diego, California.

Calvin J. Gardner, Hyunsu Kim, and Sungho Jin, "Smell-O-Vision: remotely on-off switchable odor-releasing capsules," UCSD Research Expo 2012: La Jolla, California.

David Strobel, Carl Edwards, Calvin J. Gardner, and Michelle Petty. "New Process for Space Qualified Electronic Components," in Outbrief: SBIR Phase I Project at SPAWAR, 2012: San Diego, California.

Calvin J. Gardner, Brent L. Adams, and David T. Fullwood. "Extending the Effective Range of Wilkinson's Method Via a Geometry-Based Pattern Center Correction Algorithm," TMS 2011: San Diego, California.

Calvin J. Gardner, Brent L. Adams, David T. Fullwood, John A. Basinger, and Stuart Rogers. "Dislocation Density Evolution and Strain Accumulation during an In-Situ Tensile Test," EBSD. 2010: Madison, Wisconsin.

Calvin J. Gardner, Brent L. Adams, David T. Fullwood, Josh Kacher, Scott Lemon, Daniel Seegmiller, and John Basinger. "Correlation of Grain Size with Dislocation Density in Polycrystals," MS&T 2009: Pittsburgh, Pennsylvania.

Calvin J. Gardner, Oliver K. Johnson, George Hansen, Brent L. Adams, and David T. Fullwood. "Colossal Piezoresistive Effect in Nickel Nanostrand/Polymer Composites," TMS 2009: San Francisco. California.

Calvin J. Gardner, Oliver K. Johnson, George Hansen, Brent L. Adams, and David T. Fullwood. "The Colossal Piezoresistive Effect in Nickel Nanostrand Polymer Composites and a Preliminary Quantum Tunnelling Model," SAMPE Utah 2009: Salt Lake City, Utah.

Brent L. Adams, Calvin J. Gardner, and David T. Fullwood. "EBSD-Based Dislocation Microscopy," in International Conference on Texture and Anisotropy of Polycrystals. 2009: Gottingen, Germany.

Oliver K. Johnson, Calvin J. Gardner, David T. Fullwood, Brent L. Adams, George. Hansen, and Surya Kalidindi. "Textures of Dispersion of Nickel Nanostrand Composites, and Modeling of Piezoresistive Behavior," MS&T 2009: Pittsburgh, Pennsylvania.

Oliver K. Johnson, Calvin J. Gardner, David T. Fullwood, Brent L. Adams, and George Hansen, "Deciphering the Structure of Nano-Nickel Composites," SAMPE 2009: Baltimore, Maryland.

ABSTRACT OF THE DISSERTATION

Metallic Nanotexturing via RF Plasma Processing for Advanced Biomedical Devices: Antibiofouling Neural Electrodes and Hybrid Drug-Eluting Bare-Metal Stents

by

Calvin James Gardner

Doctor of Philosophy in Engineering Sciences (Engineering Physics)

University of California, San Diego, 2015

Professor Sungho Jin, Chair
Professor Renkun Chen, Co-Chair

Metallic nanopillar/nanowire radial surface structures may by formed on alloy wire via a controlled capacitively coupled radio frequency plasma processing technique. Fully metal nanotexturing of sufficient depth and flexibility allows for enhanced performance biomedical implants, but prior to this work exploration on the technique had been limited to simple wire geometries, few materials, and exhibited a self-limiting structure depth of ~1-2 μm precluding applications dependent on increased surface area. The objective of this research was to improve and extend the RF plasma metal nanotexturing technique with the intention to develop advanced surface morphologies for biomedical implant applications, particularly antibiofouling neural electrodes and hybrid drug-eluting bare-metal stents.

Systematic review of the texturing technique included investigation into alternative plasma materials and variation of process power, chamber pressure, and exposure duration to obtain an optimal combination for maximizing surface structure depth. Experimentation led to successful texturing of diverse materials including multi-phase, single-phase, and pure metals. Procedures were developed to nanotexture additional geometries including foils, plates, and electrochemically sharpened tips. A multi-step process repetition in the parameter-controlled RF environment increased nanopillar height to at least 10 μm, a 400% expansion over previous results.

Textured MP35N wire, Pt-Ir wire, and 316L stainless steel foil electrodes were produced by repetitive RF plasma processing; each exhibited decreased surface impedance opening the possibility for improved neural recording or stimulation. Low-impedance electrodes selectively coated with hydrophobic polytetrafluoroethylene resulted in conductive antibiofouling surfaces resistant to cell adhesion. Subsequent human aortic endothelial cell culture revealed a nearly 90% decrease in cell coverage compared to an untreated electrode.

Sets of hybrid bare-metal drug-eluting stents were created from repetitively textured MP35N wires loaded with sirolimus or paclitaxel anti-restenosis agents by mechanically deforming the textured drug-loaded surface to physically confine the agents. Over the course of a 40 day in vitro release trial, the initial drug release burst upon injection was statistically suppressed and elution from the hybrid stent surface continued until at least the 20th day of the trial. Further developments potentially extend release over periods similar to commercial stents approved for clinical use.

Chapter 1: Introduction and Background

Surface modification of biomedical implants is a well established strategy to manipulate foreign body response at the material interface. For metallic devices, both macro- and micro-scale texturing in a variety of techniques have been studied and manufactured. However, true nano-scale conformal texturing of a bare metal structure has proven to be difficult with little research reported on fully metallic nanowire formations from rapid processing[1,2]. The potential for a scalable, bare metal nanotexturing technique includes but is not limited to electrodes such as pacemaker leads or cochlear implants[3]; antibiofouling structures to prevent encapsulation of devices by biological material[4,5]; enhanced endothelialization of cardiac stents to diminish late stent thrombosis[6]; and controlled drug release profiles without the necessity of any additional matrix material which could lead to ancillary complications. This dissertation explores and confirms the prospect of radio-frequency (RF) plasma nanotexturing as a viable approach for biomedical implant surface modifications.

1.1 Metallic Texturing Background

Metallic texturing techniques are too varied and numerous to possibly review in full but may be grouped broadly into as-produced surfaces which are not modified following part manufacture; mechanically textured surfaces which are modified by processing such as physical grinding, brushing, or polishing; surfaces produced by subtractive processes such as chemical etching, reactive ion etching, electron beam

texturing, or laser texturing[7]; and surfaces produced by additive processes such as sputter deposition, evaporative deposition, or electroreduction[8].

The RF plasma nanotexturing technique examined and extended in this work is a subtractive process in which material is etched away from the metal surface as the texture is formed. The process is conformal, does not require patterned masks, has minimal consumables, and could potentially be expanded into a continuous manufacturing environment. The metal nanostructure produced may consist of nanowires, nanopores, or some mix of the two and is fully integrated with the underlying metal surface.

1.2 Radio Frequency Plasma Texturing of Metal Wires

As first reported by Loya et al., metal nanowires can be produced radially on the surface of metal alloy wires[1,6]. The wires begin with an electropolished smooth surface but exposure to RF plasma while connected to a cathode plate etches nanotexture into the surface. Figure 1.1 presents a cross section of the chamber configuration with sample wires mounted vertically to a cathode base-plate such that electrical connection is maintained during processing. Generally, five wire samples have been processed simultaneously with 2.5 cm spacing between wires and produced samples exhibiting highly similar properties within processing runs. As initially reported, Argon gas at a base operating pressure of 20 millitorr was ionized to form the plasma operating at 100-200 watts power. The temperature rise was monitored by both visual inspection of the processed wires' incandescence and IR thermometer. Typical sample temperature during processing was approximated at 800-1000 °C.

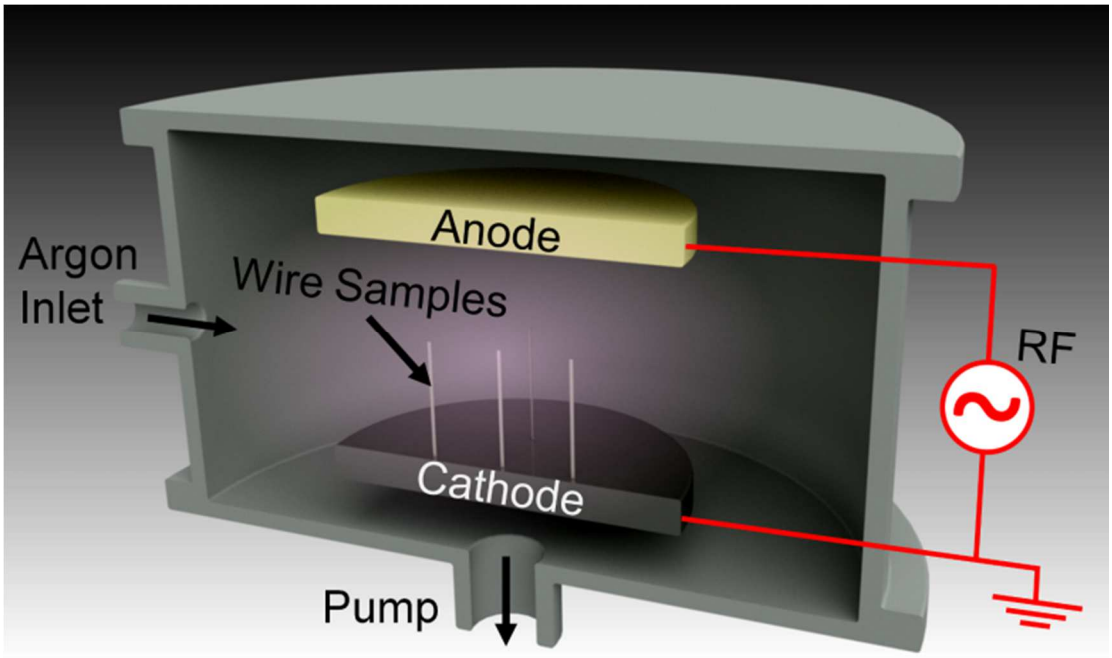

Figure 1.1. Cross-section illustration of RF plasma processing of alloy wire samples for nanotextured surface. Wires are mounted vertically to the cathode base plate and positioned between the anode and cathode. Argon plasma powered at 100-200 watts by an RF signal etches texture into the sample surfaces.

1.2.1 Materials Textured by RF plasma

A variety of materials have been shown to be susceptible to RF plasma texturing. Figure 1.2 presents a sampling of micrographs for assorted sample materials. MP35N, a medical grade alloy consisting of 35% cobalt, 35% nickel, 20% chromium, and 10% molybdenum by weight, was particularly susceptible to texturing. Platinum-iridium (both 90/10 and 80/20), nickel-chromium (80/20), copper, tantalum, platinum, inconel, and stainless steel (304 and 316L) have all been shown as texturable. Chapter 3 will discuss the methods used to extend texturing to additional materials as well as a variety of sample geometries.

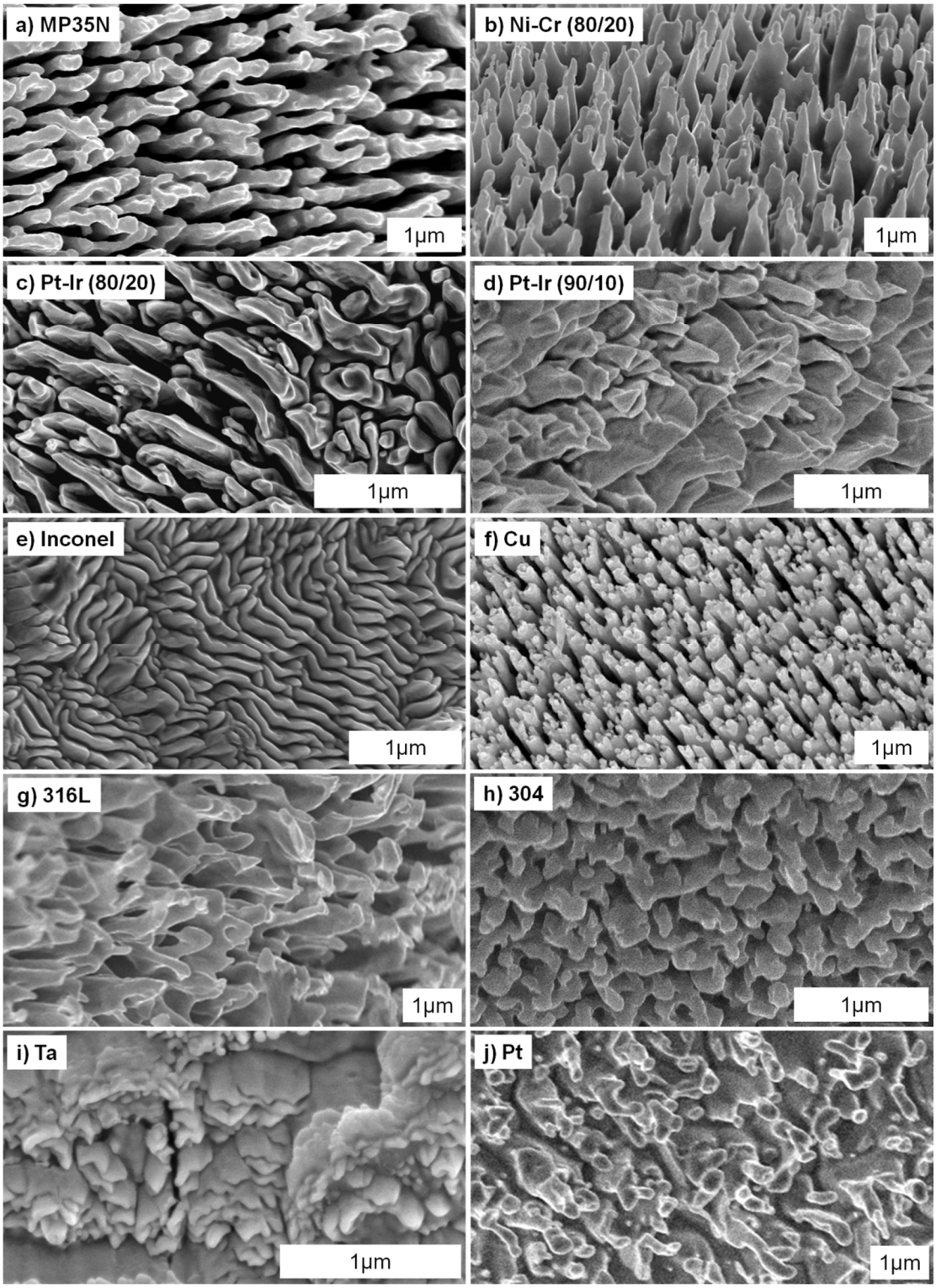

Figure 1.2.SEM micrographs of RF plasma surface texture on various materials:
a) MP35N; b) nickel-chromium 80/20; c-d) platinum-iridium 80/20 & 90/10;
e) inconel, f) copper; g-h) stainless steel 316L & 304, i) tantalum, and j) platinum.

1.2.2 Structure Evolution during RF Processing

Surface morphology changes gradually during RF plasma processing as shown in figure 1.3 for a typical 250 µm diameter MP35N. During the initial stage, shallow pockets and ripples form quickly on the surface. As the structure develops the pores continue to spread and widen interconnecting with neighboring pores. The process continues and more material is etched away until eventually the pores merge entirely leaving separated rough structures. In the final stage, nanowires form on the surface with cleaner edges and a maximally deep structure for single-run processing.

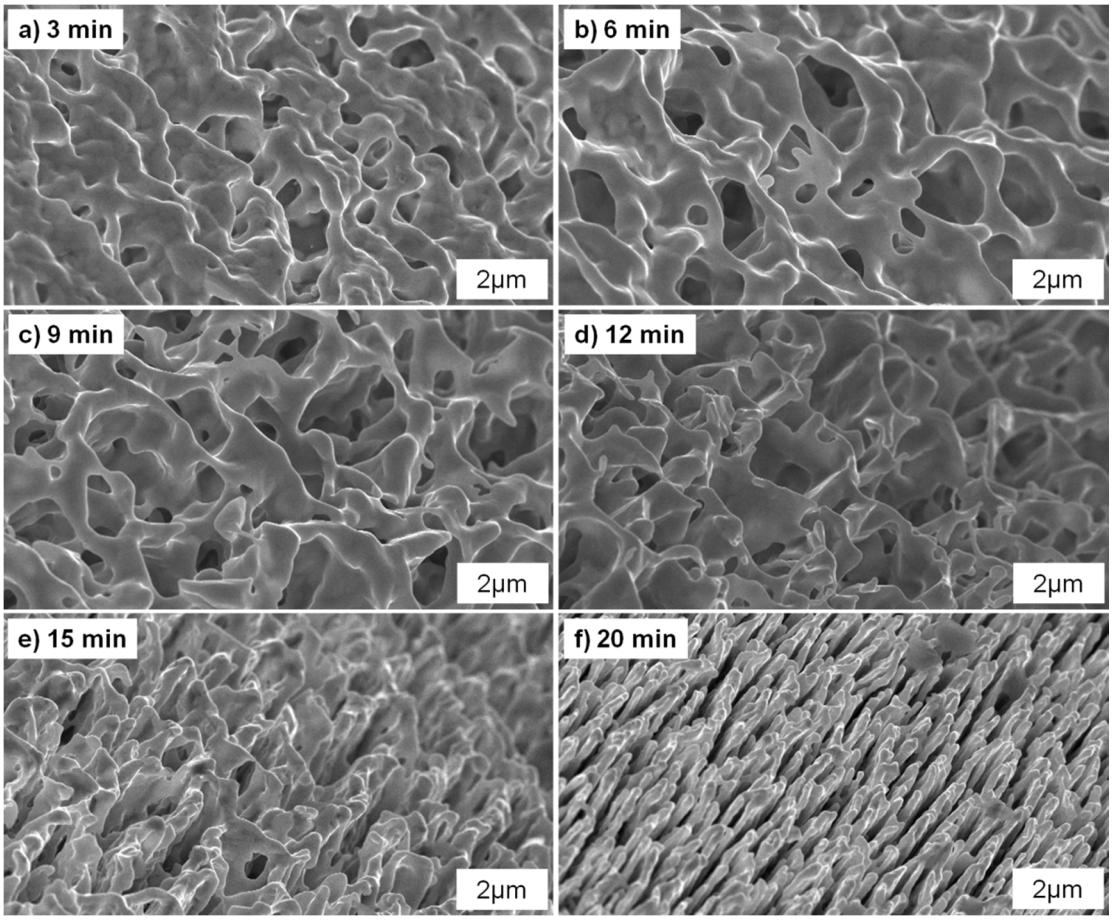

Figure 1.3. SEM micrographs of surface morphology development for MP35N in RF plasma at 200 watts and 20 millitorr Ar gas for a duration of a) 3 minutes, b) 6 minutes, c) 9 minutes, d) 12 minutes, e) 15 minutes, and f) 20 minutes.

1.2.3 Transmission Electron Microscopy of Surface Morphology

Cross-sectional transmission electron microscopy (TEM) of RF plasma textured MP35N samples has previously shown microstructural differences between the bulk material and the textured edges. Figure 1.4 presents a representative result with a single crystal diffraction pattern from the bulk material portion of a cross-section whereas areas near the tip are revealed to be polycrystalline or amorphous[9]. The disturbance of regular grain structure near the surface is not unusual but could indicate increased localized disorder near the edges from impinging ions.

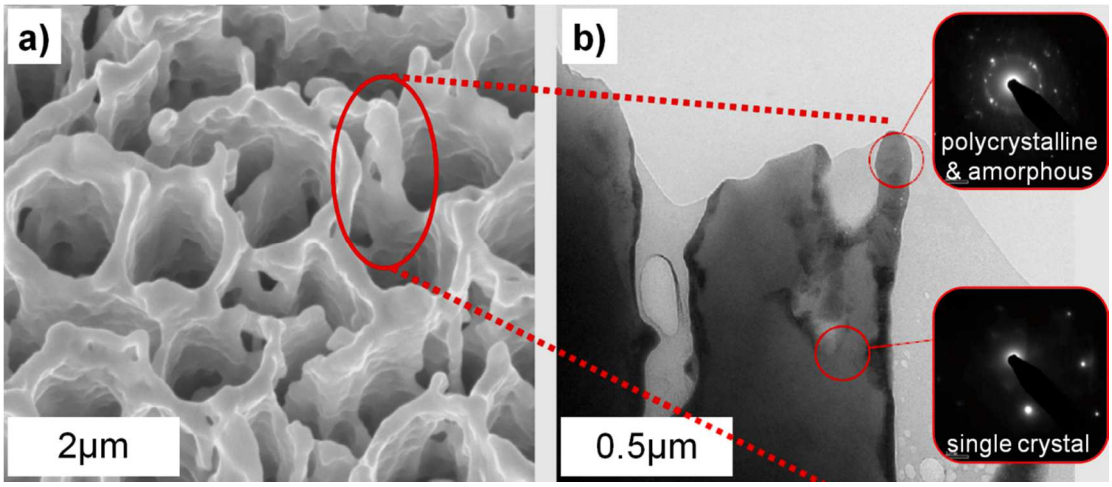

Figure 1.4. a) SEM micrograph of textured MP35N. b) Prepared thin cross-section from textured MP35N for TEM analysis with insets showing TEM diffraction patterns to indicate crystallinity.

1.2.4 Energy-Dispersive X-ray Spectroscopy of Textured Samples

Elemental analysis of MP35N samples textured in argon RF plasma at 200 watts and 20 millitorr revealed a substantial change in component concentrations. Energy-dispersive x-ray spectroscopy (EDS) data was collected from both the bulk material and the surface before and after processing. As presented in table 1.1 both the

bulk and surface measurements of element concentrations are near the specified manufacture ratios prior to processing. Following RF plasma texturing the surface EDS measurements indicate a significant decrease in nickel concentration along with a significant increase in molybdenum concentration.

Table 1.1. Energy-dispersive x-ray spectroscopy before and after RF plasma texturing of MP35N wires.

Before RF Processing			**After RF Processing**		
Element	Bulk wt%	Surface Wt %	Element	Bulk wt%	Surface Wt %
Co	35	34	Co	35	30
Ni	34	34	Ni	34	18
Cr	20	20	Cr	20	18
Mo	11	12	Mo	11	34

These measurements suggest a preferential etching of the surface in which nickel atoms are ejected more frequently and molybdenum less frequently leading to altered concentration measurements at the interacting face. Previously this buildup has been attributed to differences in sputter etch rates. However, additional results cast doubt on that possibility. Chapters 2 and 3 will delve deeper into the theoretical reason for concentration differences at the surface and the interaction with surface morphology.

1.2.5 Electron Backscatter Diffraction of Textured MP35N Cross-Section

One possible mechanism of surface texturing is etching susceptibility where grain boundaries intersect the sample surface. If the sample grain structure were revealed to be sufficiently diminutive to allow for the observed texture scale, grain boundary etching may represent a feasible mechanism. However, as demonstrated in

figure 1.5, which presents a previously collected electron backscatter diffraction (EBSD) orientation map of an RF plasma textured MP35N sample, the grains are far too large and the grain boundaries too separated to account for the surface texture[9]. Also notable is the lack of a preferred grain orientation for etching. It would appear that grain size and orientation is not a determining factor for the surface texture.

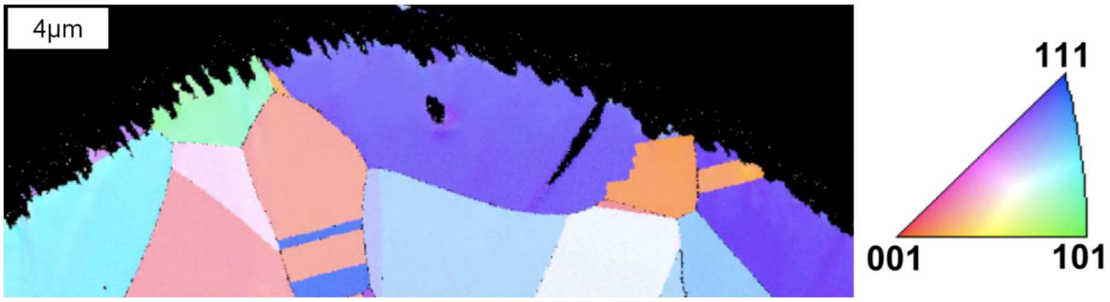

Figure 1.5. Electron backscatter diffraction orientation map of a polished cross-section from an RF plasma textured MP35N alloy sample. Diffraction patterns were compared against Nickel structure. Step size: 40 nm.

1.2.6 Phases and Preferential Etch Rates

In the MP35N system, the number of components increases the difficulty in determining the mechanism driving surface texturing. As shown on the left side of figure 1.6, the difference in sputter rates of molybdenum and nickel may contribute to the concentration shift but the low rate of chromium remains unexplained. Another alloy offers more insight: platinum-iridium is both a widespread biomedical material and a useful opportunity to test the hypothesis of preferential etch rates among phases within a material. Again, the left side of figure 1.6 presents the higher sputter rate of platinum when compared to iridium. If the difference in sputter rates is a determining factor, the percentage of platinum near the surface would be expected to decrease with RF plasma processing as the iridium weight percent increases.

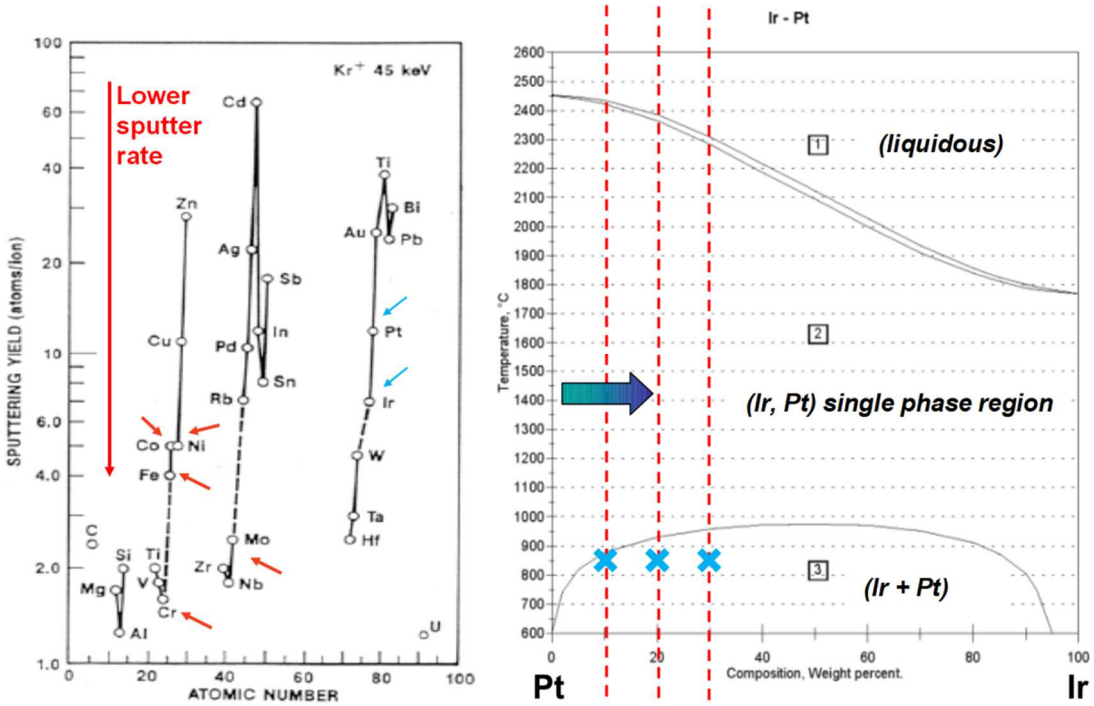

Figure 1.6. Left: Elemental sputtering yields with arrows indicating compositional elements of MP35N and Pt-Ir. Right: Pt-Ir phase diagram portraying the two phase region for RF plasma processing of Pt-Ir 90/10, 80/20, and 70/30.

Three compositions of platinum-iridium, 90/10, 80/20, and 70/30, were etched by argon RF plasma at 200 watts and 20 millitorr. The Pt-Ir phase diagram on the right side of figure 1.6 verifies that at the relevant temperature and concentrations these samples remained in a two phase region where differential sputter rates could take effect. Figure 1.7 confirms the expected increase in iridium concentration in surface EDS measurements with an increase in weight percent iridium for each composition. The surface of the 90/10 Pt-Ir doubled in Iridium concentration, 80/20 quadrupled though possibly in part due to an artificially low initial measurement, and the 70/30 increased one and a half times.

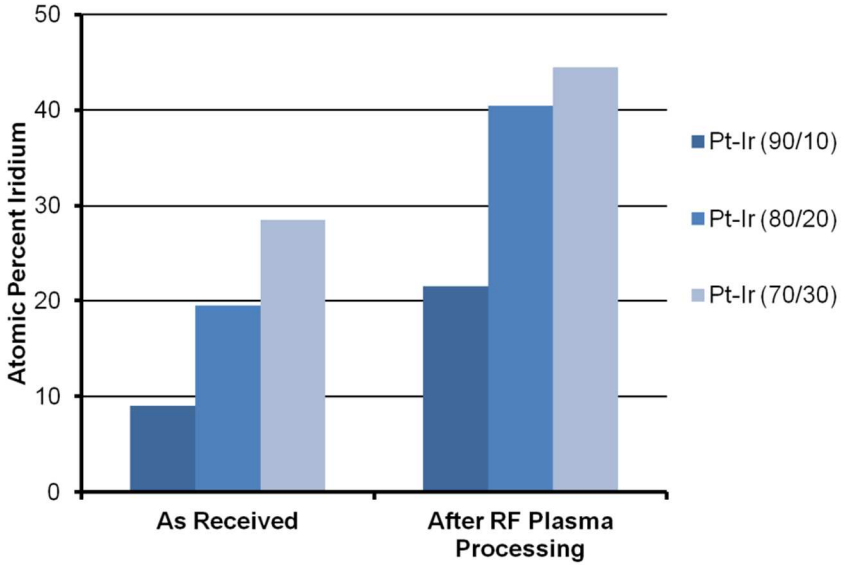

Figure 1.7. Energy-dispersive x-ray spectroscopy for surface element concentrations before and after RF plasma processing of Pt-Ir 90/10, 80/20, and 70/30.

Further evidence in support of preferential sputter etch rates in multi-phase alloys being the deterministic factor for the RF plasma texturing process comes from the Fe-Cr system. For a composition consisting of 20% chromium by mass, the processing would fall in a single phase region as indicated in figure 1.8. For such a material, if multiple phases are required for texturing, then no texturing should occur and indeed as the inset post-processing micrograph depicts there is no texturing when a sample is processed at 200 watts for 20 minutes in a 20 millitorr argon RF plasma.

Evidence seemed to be building for a simple sputter etch rate mechanism among multi-phase alloys. However, in Chapter 2 of this work some contravening examples are presented and the implications to this suggested texturing mechanism are explored including discussions of phases, ion bombardment, and microstructure irregularities[10].

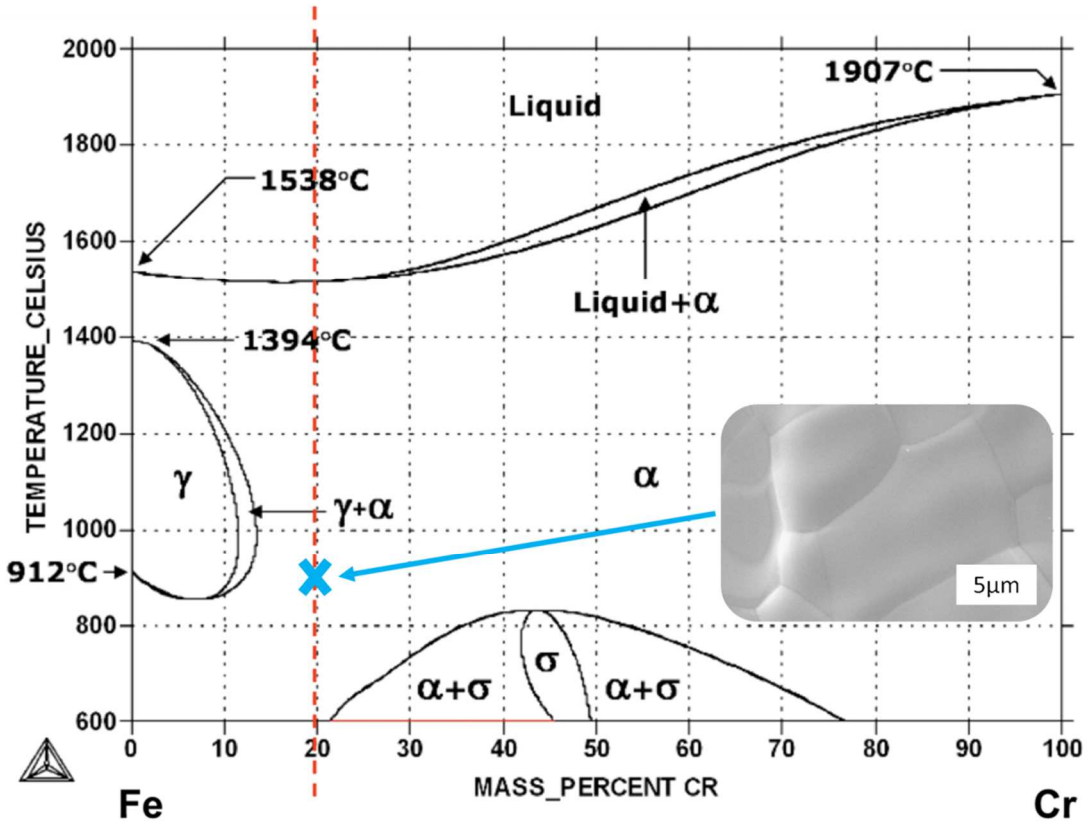

Figure 1.8. Phase diagram of the Fe-Cr system indicating the 20% Cr composition falls within a single phase region at RF plasma processing temperature. Inset shows SEM micrograph of surface following processing with no texture present.

1.2.7 Langmuir Probe Diagnostics of RF Plasma

A single tip probe was used to characterize the plasma properties as a function of position within the chamber. Variations correlate with structural changes in surface texturing and indicate that the plasma ions impinging on the surface are likely directly responsible for texture development. For argon RF plasma operating at 200 watts from a base pressure of 20 millitorr, the most pertinent results from Langmuir probe diagnostics are presented in table 1.2. These results confirm earlier measurements and show increased ion density near the cathode plate[9]. Observationally, the decreased ion density matches well with decreased overall texturing for samples positioned further

from the cathode plate and gradient texturing as sample geometries are positioned outside of the area of high ion density.

Table 1.2. Langmuir probe diagnostic results for argon plasma at 200 watts and 20 millitorr with positional variation along the vertical axis between cathode and anode.

Vertical Distance from Cathode	Electron Temperature (eV)	Density of Ions
2 cm	0.35	1.88E+11
4 cm	0.34	1.92E+11
6 cm	0.34	1.80E+11
8 cm	0.35	1.73E+11
10 cm	0.33	1.58E+11
12 cm	0.32	1.49E+11
14 cm	0.33	1.35E+11
16 cm	0.33	1.25E+11

1.2.8 Proposed Improvements to Structure Depth and Geometry

Chapters 2 and 3 of this dissertation will explore a variety of techniques and approaches that may be used to enhance the previously reported RF plasma surface texturing as well as extend it to a variety of materials and geometries. Processing parameters will be optimized for maximal structure development and then altered to overcome the self-limiting structure depth samples exhibit during continuous processing runs. Single phase materials will be textured both by the conventional method and by incorporating an additive material processing step. Samples beyond simple wire form factors will be textured including ribbons, sharpened tips, and plate geometries.

1.3 Biomedical Electrode Background

Electrical signaling between neurons is the fundamental characteristic of the nervous system and is linked to some of society's most tragic and widespread conditions[11]. Alzheimer's Disease, heart disease, hearing loss and head trauma, for example, are all related to neural misfiring, insufficiencies, and/or dysfunction[12–15]. In absence of proper neural connectivity and signaling, life inhibiting symptoms such as loss of memory, cognition, dexterity, and movement have been reported. The regeneration and reconnection of damaged neuronal pathways naturally or with surgery and medication is limited[13,14,16]. In many cases, nerve damage from disease, genetic disorders, or trauma is permanent and life threatening. However, through the combination of nanotechnology and biomaterials, small implantable electrodes offer a means to treat some neuronal conditions by providing a synthetic device that can send and receive electrical signals, normally only sent between healthy nerves[17–24].

Implantable neural electrodes have the potential to revolutionize the treatment of neuron damage and the prognosis of neurodegenerative disorders. Moreover, a greater understanding of communication between neurons can be achieved through neural electromodulation[25]. However, the effectiveness of this technology has been severely limited due to the biofouling effect of cellular growth on the surface of implanted electrodes[12,26–29]. The growth of endothelial cells on the surface of a biocompatible implanted devices is a normal biological process and for many implants regarded as essential for successful integration into the body[30–35]. But, in the case of neural electrodes cellular growth on the implant surface is detrimental to the overall

function of the electrode. The presence of a sheath of encapsulating cells limits the radial distance that an electrode is capable of sending and receiving neural electric signals[12,14,26,28,36,37].

With greater control over the distance and direction of encapsulation, fewer and more accurate and precise electrodes may be developed and incorporated into the body. Additionally, an electrode, unaffected by cellular biofouling may provide care to a larger age demographic, cut down on the number of replacement surgeries, and as result lower overall cost of neuromodulation treatments. For example, determining the minute differences between the neuronal misfiring of age related dementia and Alzheimer's Disease is a challenge whose solution has remained elusive and also a major challenge in understanding the pathology of Alzheimer's disease[38–41]. Through early and accurate diagnosis of neurodegenerative disorders, proper treatment and preventative treatments may be administered adding years onto lives with the ultimate goal of finding cures for these ailments.

In the nearer future, existing implanted neural electrodes, such as those utilized in cochlear implants and pacemakers could be made with extended lifetimes. Cutting back on the number of replacement surgeries cuts back on cost as well as risk of permanent damage and infection.

1.3.1 Biomedical Electrode Varieties

Beyond the more simple stimulating geometry of a pacemaker lead or deep brain stimulation lead, biomedical electrodes which interface with the nervous system to both record and signal are often grouped into three broad categories by their

position when implanted into the body: central nervous system electrodes, peripheral nervous system electrodes, and spinal cord electrodes. Electrodes to interface with the central nervous system include superficial arrays to be affixed to the surface of the brain[29], penetrating shafts or shaft arrays which are positioned to measure signals deeper into the brain[42], and planar electrodes with multiple recording sites which are positioned against the brain with multiple electrodes penetrating into the brain tissue[43]. For the peripheral nervous system, cuff electrodes are wrapped around the exterior of a nerve or bundle of nerves[44], sieve electrodes interface with multiple nerves that pass through separated channels[45], and intrafascicular electrodes[46]. For the dense nerve structure of the spinal cord, book electrodes are placed interleaved into the nerve tissue.

Common materials for electrodes include platinum, iridium, gold, and others. The variety of shapes and applications of biomedical electrodes necessitates a texturing process adaptable to various geometries. Chapters 2 and 3 will discuss the potential for RF plasma texturing to improve the performance of electrodes in wire, ribbon, sharpened tip, and plate structures along with the potential for more complicated form factors.

1.3.2 Cell Response Degrades Electrode Functionality

One objective of this work was to decrease the surface impedance of metallic electrodes in a biological environment by the formation of elongated radial metallic nanowires on an electrode surface. It is well established that high surface area, HiQ, electrodes exhibit decreased impedance at the electrode surface thereby allowing

higher current densities to reach targeted tissue as well as higher signal-to-noise ratios for recording electrodes[15,47,48]. At the interface between tissue and electrode, total impedance is controlled by the double-layer capacitance which is directly related to the surface area of the electrode[49]. In pacemakers, porous HiQ electrodes have been shown to improve sensing impedance and enable smaller electrode geometries which in turn improves battery efficiency[50–52]. However, the initial advantages of high surface area electrodes is lost after tissue response to implantation, such as inflammation or encapsulation, results in increased impedance[15,47,53]. Attempts have been made to better understand the mechanism of charge transfer at the electrode interface in a biomedical setting[49,54–56] and to characterize the effect of alternating current (AC) frequency on electrode impedance[57,58].

Of particular pertinence to this dissertation is work that has been done to increase electrode surface area and promote favorable integration with cell structures. Cui et al. demonstrated polymer coated neural recording electrodes that increased electrode surface area and decreased impedance in comparison to a pure gold electrode[59]. The same group also included cell-binding molecules within the polymer to help anchor the device[60]. Metal coatings have also been demonstrated as a method to amplify surface area. Norlin et al. studied electrodes coated with titanium-nickel alloy such that surface area increased by a factor of several hundreds[61]. Besides increasing surface area by adding material, electrode performance can also be improved by a selective subtractive etching process such as that performed by Loya et al. with the creation of metallic nanopillars on the surface of MP35N wires by

exposure to RF plasma[1]. Also demonstrated is favorable integration of nanopillar-textured MP35N wires with endothelial cells[6].

1.3.3 Surface Area and Impedance

However, despite the favorable cell response demonstrated on the RF plasma textured MP35N wires created by Loya et al., the surface area was not sufficiently increased to merit an electrode application: the metallic nanopillars on the surface of MP35N could only reach ~1-3 μm in average structure depth. In this work, the structure depth of metallic nanowires radially protruding from the surface of medical grade alloy wires is extended significantly by optimizing process parameters and procedures in pursuit of a high surface area, low impedance electrode, which is also textured to integrate favorably into cell structures.

1.3.4 Proposed Improvement to Biomedical Electrode Performance

Chronic electrode implants are used to stimulate or record electrical impulses in the brain or other electrically excitable tissue. However, implanted electrodes are susceptible to tissue response which causes failure by encapsulating the electrode itself in a glial scar sealing the electrode off from neural signals. The success of chronic electrode implants depends largely on the electrode/tissue interface, including: electrode material, surface morphology, and electrode geometry. By decreasing electrode surface impedance with an innovative RF plasma metallic texturing process resulting in nanopillar formations an electrode can both record smaller signals and more easily deliver stimulation. Chapter 4 of this thesis will focus on impedance

advances. Additionally, a conductive textured electrode can be made resistant to fouling by coating the topmost portion of the pillars in an antibiofouling hydrophobic material as will be discussed in chapter 5. The constructed electrode may then retain both conductivity and optimize the antibiofouling characteristics of the surface.

The potential advantages of fouling-resistant low-impedance interfacing technology is staggering. It could be possible to extend such a technology for the restoration of lost sensory or motor function[62,63]; victims of paralysis due to peripheral nerve injury could achieve a full recovery by directly recording the output of their motor cortex; sensory prosthetics that interface directly to the nervous system could be developed[17,37,64]; deep brain stimulation therapy for Parkinson's and clinical depression could retain effectiveness without the need to increase the stimulation voltage[42,65,66]; recording interfaces for neuroscience research could be greatly improved[67], and many other exciting possibilities await.

1.4 Antibiofouling Background

Many techniques have been attempted to both maintain the electrical integrity of an implantable neural electrode and minimize the biofouling effect[68,69]. Topographical patterning of implant surfaces has been shown to influence cell adhesion, migration, orientation, shape, and cell fate[30,33–35]. Nanotextured surfaces, such as silicon nanowires[70], patterned carbon nanotubes[23], and nanospun fibers have been used to optimize the intermolecular forces between the cells and an interfaced solid state surface[71]. The result of minimized interaction forces is an unfavorable environment for cell adhesion and thus a structural means for antibiofouling results.

Polymer coatings such as poly(dimethylsiloxane) (PDMS) and poly(ethylene glycol) (PEG) have also been used to minimize the interaction for by providing a hydrophobic coating[69].

1.4.1 Antibiofouling Surface Strategies

Much work has been done to limit biofouling of medical devices. Approaches typically fall in one of three categories[69]. Often the simplest is a homogenous surface either produced in bulk or coated to have hydrophobic, hydrophilic, or amphiphilic properties. Such surfaces may prevent cellular attachment, encourage attachment elsewhere, or decrease the viability of attached cell life. Another approach is a patterned or mixed heterogeneous surface with alternating hydrophobic and hydrophilic areas which may be used to promote cell movement away from a surface or make attachment difficult and inconsistent. Finally, three-dimensional surfaces with a controlled topography can also influence attachment, development, and viability.

1.4.2 Proposed Antifouling Measure for Biomedical Electrodes

Drawing inspiration from each of the three conventional antifouling strategies, this work presents a novel nanostructured surface for superior neural electrode functionality exhibiting antibiofouling properties. We have combined technologies using both novel texturing and polytetrafluoroethylene (PTFE or Teflon) coatings to maximize the antibiofouling characteristics of the surface. Such a surface exploits the relative advantages of homogeneous, heterogeneous, and three-dimensional antifouling strategies in a novel mixed approach.

For instance, one common implant scenario concerns aortic endothelial cells (EC) which line the vessels and arteries of the heart forming the endothelium by cell-to-cell connections[72]. A healthy endothelium exhibits a continuous layered network of EC tissue. This layering across an implanted neural electrode is the main cause of electrode degradation. Presented in chapter 5, substrates of 316L stainless steel were first repetitively exposed to RF plasma creating a novel nanotextured surface, then coated with PTFE along the outer edge of the surface texture, and compared to optimized cell culture plate and homogeneous untextured 316L implantable electrodes. Cell proliferation and cell spreading were significantly decreased by the combined nanotexturing and PTFE coatings as compared to texturing alone and the bare untextured surface. Surface impedance measurements were conducted in phosphate buffered saline (PBS) for untextured 316L electrodes, nanotextured 316L electrodes, and nanotextured PTFE-coated 316L electrodes. Nanotexturing the electrode decreased the surface impedance in the lower frequency range (<1000Hz). Subsequent coating of nanotextured electrodes with PTFE returned the low frequency surface impedance to a level comparable to the untextured 316L electrodes. The high frequency range, where electrolyte characteristics dominate, was unaffected[48]. Full details will be reported in Chapter 5 of this work.

1.5 Cardiac Stents and Drug Delivery

A stent is a small mesh tube-shaped structure employed to mechanically open a restricted artery and ensure normal blood flow or to support a weakened arterial wall as depicted in figure 1.9. Following implantation, foreign body response to the stent is

a primary concern for patient outcomes. Should the body react unfavorably to the implant, further arterial narrowing or restenosis may occur[73]. Another potential issue is the degradation of stent material leading to late stent thrombosis or very late stent thrombosis and possibly infarction and death[74,75]. In any sense, the placement of coronary stents during subcutaneous coronary intervention or angioplasty has represented a remarkably successful step forward in medical science.

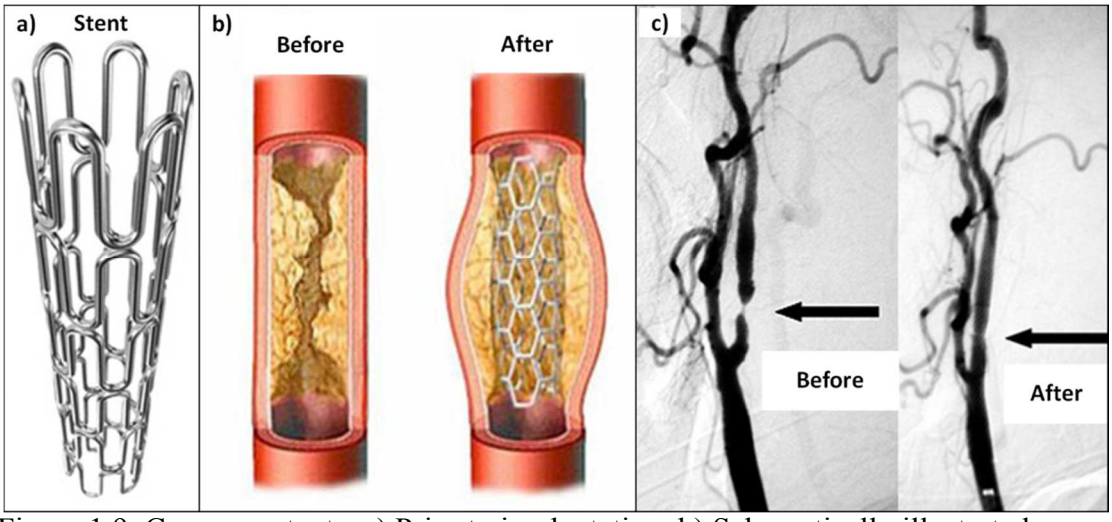

Figure 1.9. Coronary stents. a) Prior to implantation. b) Schematically illustrated showing before and after insertion and expansion. c) In situ showing expanded blood-flow.

1.5.1 Coronary Artery Disease

Coronary artery disease (CAD) affects more than 13 million Americans and is the leading cause of death in the United States[76]. Caused by the hardening of coronary arteries following the gradual deposition of lipid and cholesterol plaques on the tunica intima of an artery or vein. When surgical intervention is necessary, CAD is commonly treated by balloon angioplasty and stent placement.

1.5.2 Cell Proliferation and Surface Texturing

Bovine aortic endothelial cells (BAEC) have shown superior growth on RF plasma textured MP35N substrates[6]. During incubation, BAEC adhered preferentially to textured substrates in comparison to both untextured and control dish environments. On the textured substrate, cells formed smooth continuous cellular layers similar to a natural vessel wall whereas on untextured MP35N BAEC clustered with no apparent organization. Immunostaining revealed well formed peri-junctional cortical bands of filamentous actin formed on textured MP35N but untextured MP35N remained aggregated and lacked intercellular junctions. Surface texturing of stent materials could potentially reduce foreign body response following angioplasty.

1.5.3 Controlled Release of Anti-restenosis Drugs

Drug-eluting stents (DES) approved for clinical use in the United States employ a polymeric coating to hold and release medication[77–79]. In comparison to bare-metal stents (BMS), DES have lower rates of major adverse cardiac events representing a major step forward for angioplasty[78,80–84]. However, DES may have an increased risk of late thrombosis lasting at least five years after implantation[75,85–89]. In combination, the decreased risk of restenosis offsets the possible increased risk of late thrombosis and when considered overall DES are not associated with increased mortality[90].

Still, prevention of late thrombosis from DES offers an enticing avenue for improvement in interventional cardiology[91]. Coating strategies vary widely including but not limited to dip coating, spray coating, plating, sputtering, and mineralization.

Drug release may be diffusion controlled with water-insoluble polymers, degradation-controlled with water-soluble or hydrophobic polymers, ion exchange-controlled, or some combination or extension of the former. Later generation DES with improved long-term safety have emerged relying on advanced materials, biodegradable polymers, polymer-free stents, and as a future possibility, fully erodible stents[77,82,92–95]. At present, stent thrombosis leading to myocardial infarction remains a concern for DES in need of a reliable mitigation.

1.5.4 Anti-restenosis Drug Release Control Mechanism

Medicine may be released from a loaded stent surface by a diffusion-controlled mechanism, degradation-controlled mechanism, or an ion exchange mechanism[96]. Diffusion-controlled DES can extend release time by restricting the drug release path often with the addition of a semi-porous polymer layer. Most diffusion-controlled drug elution may be modeled with first-order kinetics. Degradation-controlled diffusion relies on the gradual decomposition or dissolution of a drug loaded stent coating when subjected to a body environment[97]. Worries remain about the possible health effects of gradual degrading bits as they may enter the patient's blood stream. Elution kinetics for degradation-controlled release fall somewhere between first-order and zero-order. An ion exchange mechanism could also be employed where ionizable drugs are coupled with oppositely charged ionic groups on a polymer matrix[96]. The drug release kinetics would then depend on the pH and electrolyte concentration of the stent environment.

1.5.5 Drug-Eluting Stents and Bare-Metal Stents

Following stent placement, foreign body response may lead to in-stent restenosis accompanied by angina and potentially myocardial infarction. To reduce this risk, DES have been developed which slowly release anti-restenosis medicine to prevent thrombosis by blocking cell proliferation. DES are typically constructed with multiple layers, built upon an underlying metal stent strut[91,94]. In a basic DES design, the first layer may act as a primer to promote adhesion of subsequent coatings to the substrate. The second layer consists of a drug-infused polymer to carry anti-restenosis agents. The final layer may consist of a polymer cap to slow and extend the release. In addition to directly combating fibrosis and encapsulation, DES can be designed to reduce both acute and chronic inflammation which stimulate immune response.

Table 1.3 presents a timeline of DES approved for clinical use by the U.S. Food and Drug Administration. The CYPHER™ stent received approval in Spring 2003 with a stainless steel strut and the capacity to release anti-restenosis sirolimus over a 30 day period[98]. The TAXUS™ stent releasing antiproliferative paclitaxel and a 316L stainless strut followed in 2004 with extensions coming in 2008 and 2009 under the TAXUS name[99–102]. Medtronic's Endeavor DES received approval in 2008 utilizing an MP35N strut with immunosuppressant zotarolimus release followed by a materially similar Resolute Integrity with an extended 180-day release profile[103–105]. The XIENCE™ DES line also received approval in 2008 followed by extensions in 2011 and 2014 using a cobalt-based XSH Alacrite as the stent strut material with immunosuppressant everolimus release over 120 days[106–109].

Table 1.3. Drug-eluting stents approved for clinical use by the U.S. Food and Drug Administration.

FDA Approval Date	Stent Name	Corporation	Strut Material	Eluted Drug	Release Time
2003 April 24	CYPHER™	Cordis	316L Stainless	Sirolimus	30 days
2004 March 4	TAXUS™ Express² ™	Boston Scientific	316L Stainless	Paclitaxel	90 days
2008 February 1	Endeavor	Medtronic	MP35N	Zotarolimus	-
2008 July 2	XIENCE™ V PROMUS™	Abbott	L605	Everolimus	120 days
2008 October 10	TAXUS™ Liberté	Boston Scientific	316L Stainless	Paclitaxel	90 days
2009 May 21	TAXUS® Liberté® Atom™	Boston Scientific	316L Stainless	Paclitaxel	90 days
2009 July 13	TAXUS® Liberté® Long	Boston Scientific	316L Stainless	Paclitaxel	90 days
2011 April 22	ION™	Boston Scientific	Pt-Cr	Paclitaxel	-
2011 May 24	XIENCE nano™	Abbott	L605	Everolimus	120 days
2011 November 1	XIENCE Prime XIENCE Prime LL	Abbott	L605	Everolimus	120 days
2011 November 22	PROMUS® Element™	Boston Scientific	Pt-Cr	Everolimus	-
2012 February 17	Resolute Integrity	Medtronic	MP35N	Zotarolimus	180 days
2012 June 1	PROMUS® Element™ Plus	Boston Scientific	Pt-Cr	Everolimus	-
2012 November 14	Zilver PTX	Cook	Nitinol	Paclitaxel	1 day
2014 October 3	XIENCE Xpedition® XIENCE Xpedition SV XIENCE Xpedition LL XIENCE Alpine™	Abbot	L605	Everolimus	120 days

Initially, PROMUS™ DES mirrored the XIENCE™ V in 2008, but later additions in 2011 and 2012 switched from the L605 strut to platinum-chromium while maintaining the everolimus release[106,110,111]. The ION™ DES which received approval in 2011 also released everolimus and used a platinum-chromium strut[112]. The most recent addition to approved DES lines came in late 2012 with the Zilver PTX peripheral stent utilizing a nitinol strut and immediate paclitaxel release rather than a polymer infused coating[113]. The Zilver PTX line relies on trapping the anti-restenosis drug between the stent surface and the tunica intima of an artery or vein. This method elevates drug levels surrounding the stent for a few days but is not comparable to the extended release profiles of the polymer coated types.

DES have been an excellent advancement with short-term restenosis rates dropping precipitously and the associated myocardial infarctions diminishing as well[80]. However, there have been some drawbacks associated with DES in the form of late stent thrombosis often attributed to degradation or delamination of the polymer coating matrix over time after the anti-restenosis agents have eluted completely. When compared to BMS, increased inflammation, thrombogenecity, late stage thrombosis (LST), and very late stage thrombosis (VLST) occur more frequently with DES[75,88]. Overall, the advantages gained by DES more than overcome the delayed elevated risk factors and indications point to newer DES designs having improved long term outcomes[92]. BMS remain in use, despite not performing as well in the short-term, partly because long-term issues remain less frequent for BMS.

1.5.6 Proposed Bare-Metal Stent Construction

Conformal texturing of MP35N biomedical alloy in a functional BMS geometry could promote natural endothelialization of an arterial wall following stent placement. Reduced cellular oxidative stress levels, smooth monolayer formations, improved adhesion, and well organized peri-junctional cortical bands may decrease short-term restenosis while also decreasing the risk of LST or VSLT when compared to DES. Chapter 6 of this work will discuss a middle-ground solution between DES and BMS in which anti-restenosis drugs may be released in a controlled fashion from a bare-metal surface without the necessity of additional drug-loaded material polymer or otherwise.

A finely textured BMS can act as a DES without the addition of any matrix material (polymeric or not) to hold the anti-restenosis drugs. Improvements to the RF plasma nanotexturing process established by Loya et al. makes drug storage in the metal nanostructure a possibility[10]. In chapter 6, drug release profiles of sirolimus and paclitaxel are manipulated and extended by loading drug into bare-metal nanostructures created by RF plasma texturing on the surface of medical grade alloy wires and then deforming the surface structure to restrict diffusion.

Release profiles of untextured, textured, textured/deformed, and control groups are compared over a 40-day in vitro trial comprising both the initial burst release phase and extended diffusion from the surface. With future refinements a stent constructed as a hybrid of the bare-metal and drug-eluting models could have the

superior late thrombosis properties of a BMS while retaining the anti-restenosis advantage of DES.

1.6 Scope and Outline of the Dissertation

Implants can extend life, enhance life-quality, repair damaged biological structures, protect from further harm, provide valuable physiological data, or accomplish a multitude of other medical objectives. Under ideal conditions, implants accomplish precisely what they are designed to do. However, in practice foreign body response can lead to a wide variety of complications such as infection, inflammation, encapsulation, or even rejection. The human body is well adapted to attack and remove alien invaders of its internal environment with no regard to medical intent. Consequently, creative and resourceful solutions are needed to mitigate and manipulate the body's natural response to an implant's presence such that it's function is not diminished.

In this dissertation, a unique metal texturing technique by way of RF plasma is first developed to produce desired surface structures, then employed to improve the impedance and antifouling performance of chronic electrode implants as well as to control drug delivery from the surface of an implantable coronary stent without the need for potentially harmful additional matrix materials.

Chapter 1 gives a brief background on metal texturing by RF plasma processing, biomedical electrodes, antibiofouling strategies, coronary stents, and controlled drug release.

Chapter 2 discusses the optimization of basic RF plasma nanotexturing for a variety of sample materials, plasma materials, powers, durations, pressures, and geometries. Also discussed is the theoretical mechanism of surface texturing as indicated by texturable results to the present point as well as a theoretical model for ion bombardment.

Chapter 3 discusses a breakthrough in RF plasma processing allowing for significantly deeper surface texture creation through precisely controlled repetitive exposure with maximum structure depth increased at least 400% in comparison to self-limiting depths reported prior. Also discussed is the extension of this technique to a variety of materials and geometries.

Chapter 4 contains experimental results of surface impedance for RF plasma textured electrodes. Significant decreases in surface impedance are reported for the low frequency range in simulated body fluid electrolyte.

Chapter 5 reports the construction of a novel antibiofouling surface intended for chronic electrode implants which retains electrical conductivity by RF plasma texturing while simultaneously presenting a hydrophobic antifouling surface to adjacent body tissue.

Chapter 6 demonstrates the feasibility of controlled drug release from a bare-metal stent surface which has been textured by RF plasma processing, loaded with anti-restenosis agents under vacuum, and then deformed to physically restrict diffusion from the surface.

Chapter 7 gives a summary of the main results of this work, discusses ongoing research, and outlines future exploration related to the dissertation topic.

Chapter 2: RF Plasma Nanotexturing Improvements and Extensions

RF plasma nanotexturing of metallic alloys is a novel etching process dependent on a variety of process parameters. When this work began, only a limited number of materials and parameters had been previously explored and systematic optimization hadn't yet been attempted. Nearly all previous texturing work was performed in MP35N biomedical alloy and typically as a single processing step. An entire search space of alternative plasma materials, power levels, durations, pressures, and structure materials invited exploration.

2.1 Limitations on Former RF Plasma Texturing Technique

Previous to this work, RF plasma texturing of MP35N biomedical alloy demonstrated a self-limiting structure depth with the maximum depth reached after approximately 20 minutes of processing. As shown in figure 2.1, further processing would not deepen the structure although material would continue to be removed evenly from the surface by etching. For many application, a deeper overall texture would be preferable. Deepening the structure increases surface area, decreases surface impedance, and opens up the possibility of storing drug molecules in the surface structure. Thus, an initial objective of this thesis was to dependably characterize the surface structure of RF plasma processed MP35N or other texturable alloy materials and then to vary parameters in search of increased overall structure depth. In this initial characterization, varied parameters included plasma material, power, pressure, and duration. Other parameters were held constant as specified below.

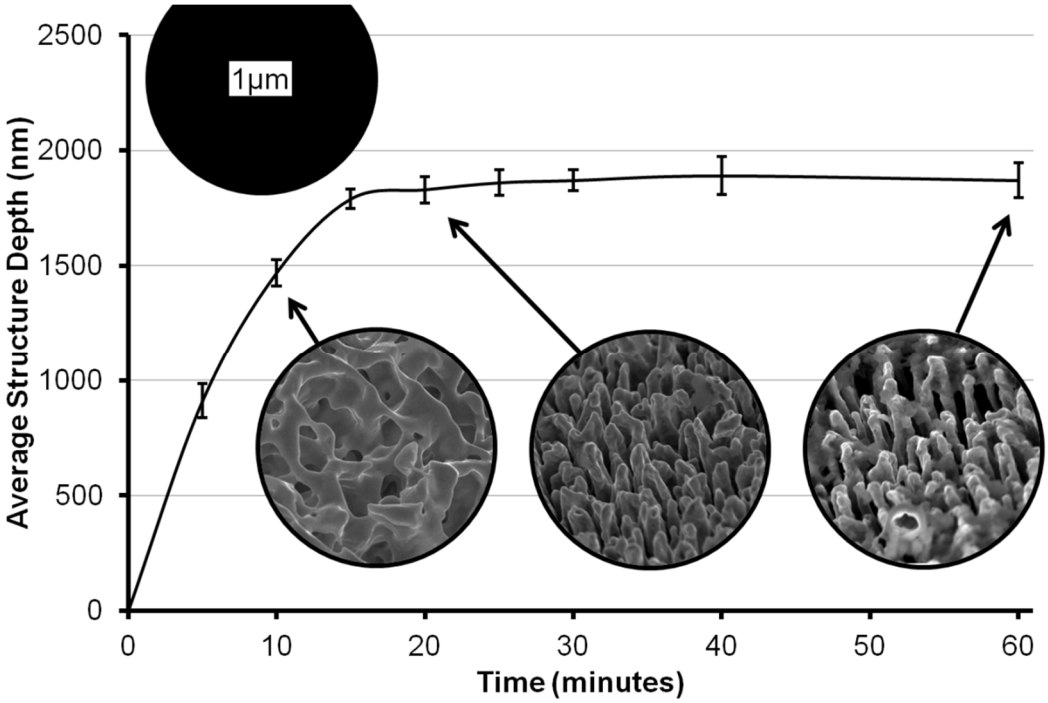

Figure 2.1. Progressive surface texturing depth for MP35N processing in argon RF plasma powered at 200 watts with a base pressure of 20 millitorr. Inset micrographs show structure after 10 minutes, 20 minutes, and 60 minutes. Inset in upper left gives scale bar for all three micrographs. Error bars are first standard deviation.

The sample alloy wires used for characterization experiments were made of medical grade alloy MP35N (35% Co–35% Ni–20% Cr–10% Mo in wt.%) and Pt-Ir (80% Pt–20% Ir) having a 250 µm diameter and an electropolished smooth surface. For texturing, five approximately 10 cm long wire samples were mounted vertically in the cathode plate base at 2.5 cm spaced apart from the neighboring wires. Within this wire-mounted region, the RF plasma texturing results were identical, independent of the location of sample mounting in chamber. Prior to processing, the chamber was evacuated to 10^{-5} Torr, then gas flow was initiated and pressure increased to the desired level by partially closing the high vacuum valve. Experiments were performed using a custom-built RF plasma system (13.56 MHz), with the RF powered cathode

using 30 sccm of Ar, H_2, or N_2 gas flow at a base operating pressure between 15 and 25 millitorr and subjected to between 100 and 300 watts power. The temperature rise of the MP35N and Pt-Ir wire samples was monitored using visual inspection and an IR thermometer, and was estimated to be in the 800–1000 °C range.

2.2 Surface Structure Characterization

After RF plasma processing, surface microstructures of the wire samples were investigated by scanning electron microscope (SEM, model FEI XL30-SFEG), brittle fracture in liquid N_2, interrogating the surface with a diamond scribe, and on-end polishing of textured wires embedded in epoxy. Five identical samples were produced with each round of processing and multiple measurements were conducted on each sample to promote statistical significance.

2.2.1 Mechanical Interrogation of Structure Depth

Determining structure depth proved challenging. The closeness of adjacent surface structures prevented a simple tilted view of the texture from revealing depth. Simple mechanical deformation of the textured surface was generally unsuccessful as a method to determine surface structure depth. Crimping, cutting, diamond scribe, and fatigue failure were all attempted but the small scale of the surface resulted persistently in local deformation and inaccurate measurements. Figure 2.2 is an on edge view of diamond scribed and then crimped surface. The deformations along the edge are obvious and make any determination of structure depth impossible. A different approach was necessary.

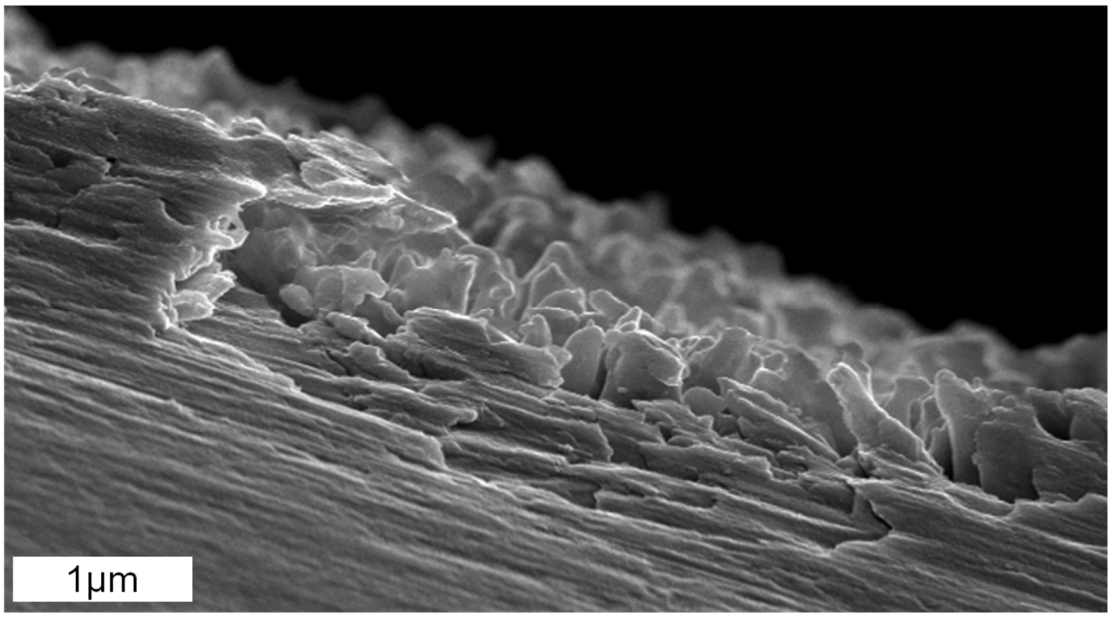

Figure 2.2. On edge view of RF plasma processed MP35N surface which was interrogated with a diamond scribe and then crimped.

2.2.2 Embedded Polishing

To avoid local surface deformation, textured MP35N samples were embedded in epoxy for polishing. Samples were RF plasma processed using the standard 20 minutes, 200 watts, 20 millitorr procedure before embedding and curing in epoxy. Polishing was performed stepwise from 180 grit sandpaper to 1 µm diamond polishing compound before finishing with colloidal alumina suspension. To prevent problematic charging, carbon tape and conductive silver paste coatings were applied to the nonconductive epoxy while leaving portions of the polished ends of MP35N visible. Figure 2.3 is a representative micrograph.

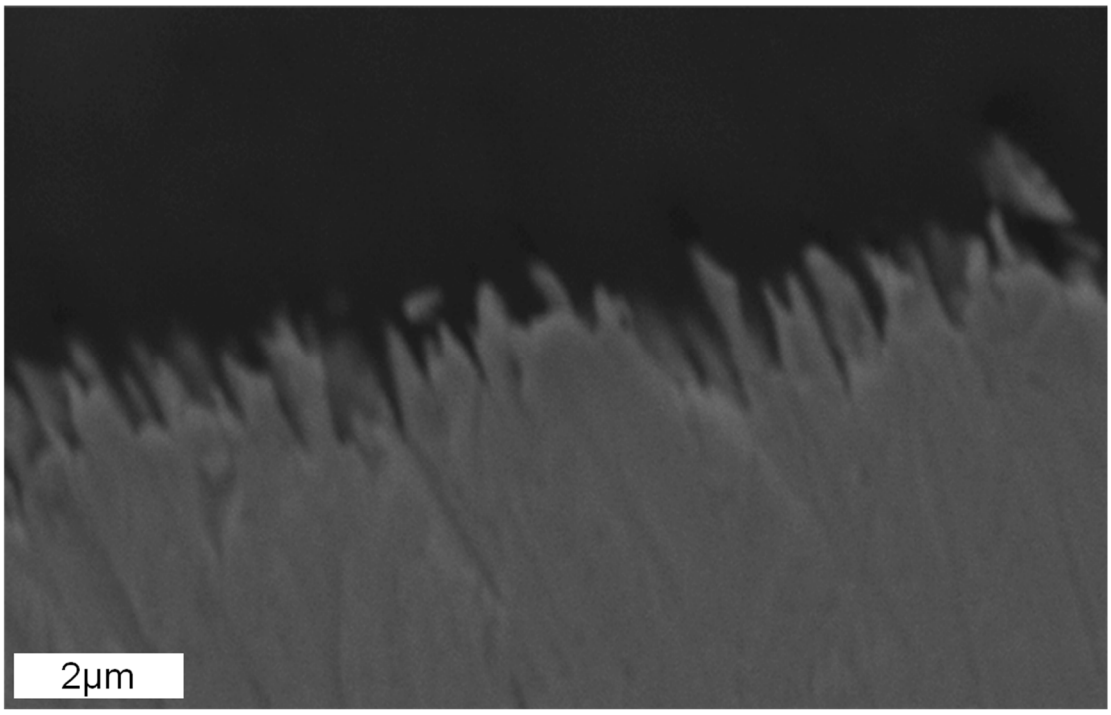

Figure 2.3. SEM micrograph of RF plasma textured MP35N embedded in epoxy and polished to reveal on end structure and overall depth of less than 2 micrometers.

Embedding and polishing successfully revealed the surface structure with reduced deformation but some local deflection was still apparent as texture often angled slightly away from being radial or perpendicular to the underlying surface. The procedure was also slower than would be preferable for many sample runs and the image quality of the nanostructure diminished quickly for anything not at the immediate surface. A quicker and higher quality technique was still needed.

2.2.3 Brittle Fracture of RF Plasma Textured Samples

The most consistently successful method for determining surface structure depth of an RF plasma textured samples was partial sectioning followed by full immersion in liquid N_2 and sudden fracture by longitudinal stress. For materials which experience a pronounced ductile-brittle transition temperature (DBTT) this method is

particularly effective. However, as shown in table 2.1 MP35N does not have a sharp DBTT but rather only a slight reduction in impact strength at decreased temperatures.

Table 2.1. Charpy V-notch impact strength of MP35N at a strength level of 1930 MPa[114].

Condition	Temperature (°C)	Impact Strength (J)
Cold drawn 49% and aged 649 °C 4h, air cool	24	25.6
	-73	23.2
	-129	20.7
	-196	21.8
	-253	18.3

Still, the slight reduction in strength was sufficient for an improved fracture surface when compared to both the diamond scribe and the embedded polishing methods and provided a satisfactory edge-on view of the RF plasma textured structure for characterization. As shown in figure 2.3, the transition from flat fracture surface to the textured area is a sharp change without any obvious deformation of the texture. Through the use of oblique estimations, physical interrogations, embedded polishing, and especially cold fracture of RF plasma textured samples it was possible to characterize structure depth for selected processing parameters. To promote statistical significance multiple samples and multiple positions on each sample were measured throughout the study. Good consistency between samples and within samples was observed.

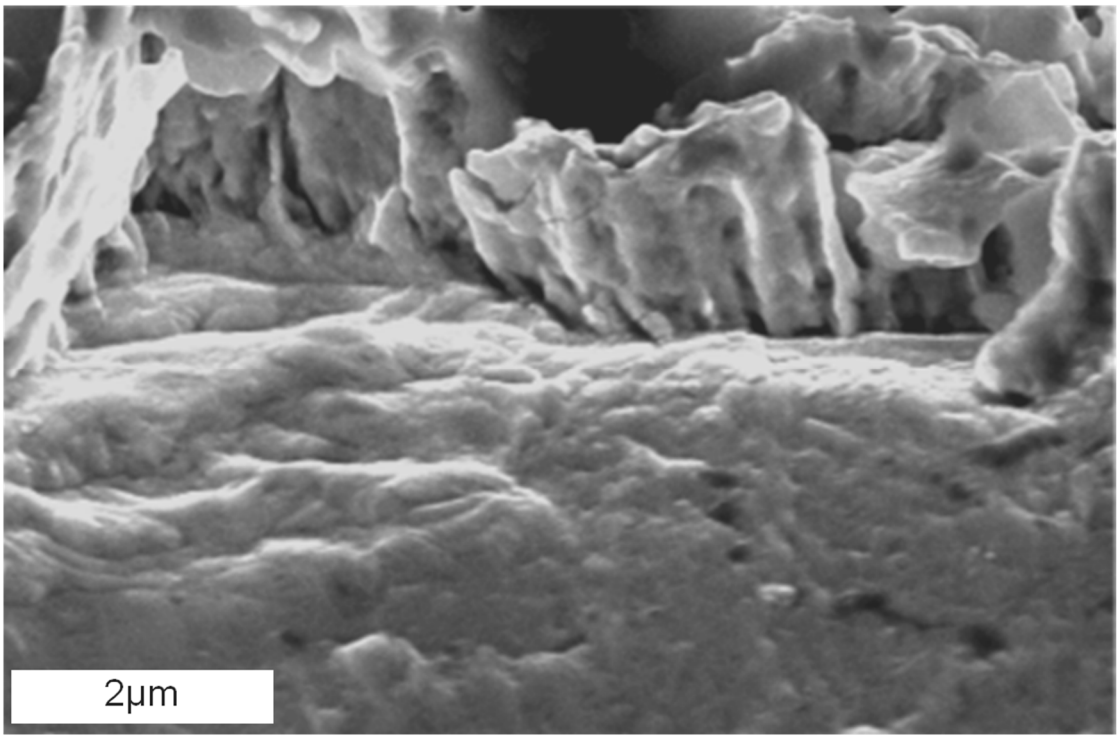

Figure 2.4. Edge view of RF plasma textured MP35N following partial sectioning and fracture submerged in liquid N_2.

2.3 Alternative Plasma Materials

Formerly only argon RF plasma had been demonstrated to produce nanopillars on MP35N alloy's surface. In the present study two additional plasma species were also evaluated, hydrogen and nitrogen. These two materials were selected because of their availability and frequency of use in plasma systems. Future investigations into heavier elements such as krypton or xenon is merited.

2.3.1 Hydrogen Plasma

Figure 2.5 shows the resultant surface structures on MP35N wire when processed with RF plasma using a hydrogen plasma at 250 watts for 20 minutes and a base operating pressure of 25 millitorr. Increases in power and pressure were chosen

after lower values produced almost no structure whatsoever. As shown, Hydrogen plasma produced only small clusters of 200-500 nm round formations within a shallow interlocked structure and no significant increase in surface area. Interestingly, the globule formations do not appear to be etched in place as with the argon plasma texturing. In regards to the high surface area objective, hydrogen plasma did not present a viable path to increased structure depth.

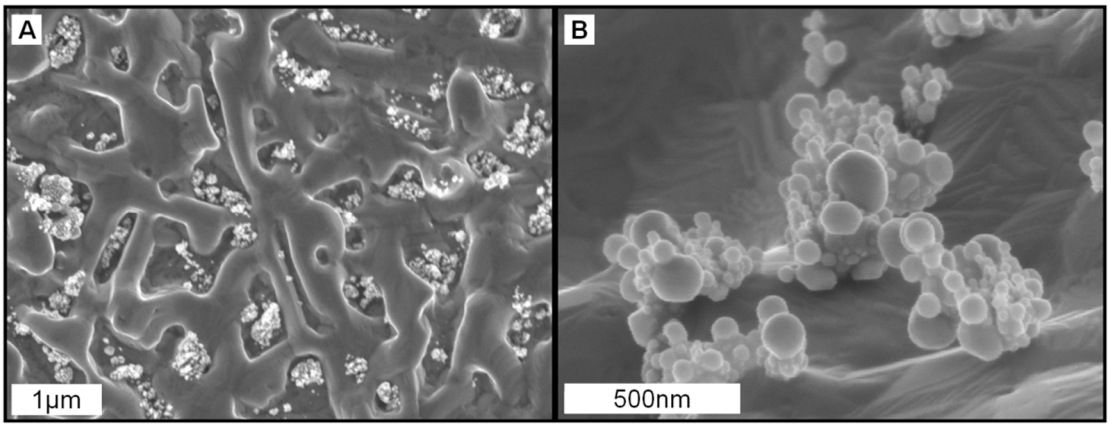

Figure 2.5. (A) and (B) SEM micrographs of MP35N processed in hydrogen RF plasma showing minimal surface texturing.

2.3.2 Nitrogen Plasma

Figure 2.6 shows that nitrogen RF plasma at 250 watts for 20 minutes with a base pressure of 25 millitorr produced larger 2 µm cone structures scattered sparsely across the surface. The conical shape of the etched structures matches precisely the predicted behavior of a surface under ion bombardment to be discussed in section 2.6.2. Still, the surface area was not significantly affected by the scattered nitrogen plasma texturing and nitrogen did not give any indication of being a good strategy for increased depth.

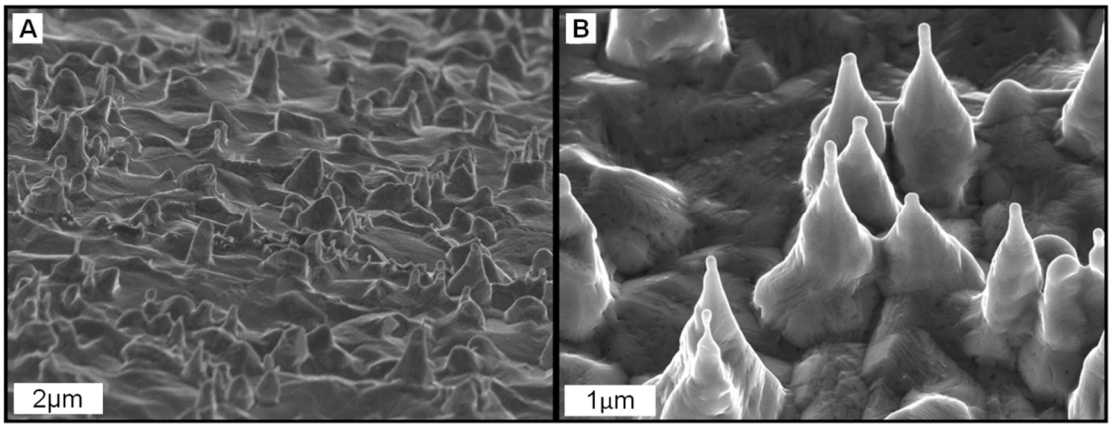

Figure 2.6. (A) and (B) SEM micrographs of MP35N processed in nitrogen RF plasma showing cone formation but still mostly minimal surface texturing.

2.3.3 Argon Plasma

As shown in earlier figures, argon plasma produces significantly denser and deeper texturing than either the argon or nitrogen plasma textured samples. Comparison of argon, hydrogen, and nitrogen plasmas indicate that atomic weight is likely a key parameter to the nanowire formation process. The bombardment by heavier ions, such as those in argon plasma, produces more evenly distributed and consistent nanowire texturing of a greater depth and much greater surface area. For the remainder of the structure depth study, argon plasma was selected.

2.4 Processing Parameters

Many different parameters affect the surface structure that develops during RF plasma processing. Among the most important is the interaction of duration, power, and pressure which can behave unpredictably. A search space surrounding the typical processing parameters for MP35N was outlines for investigation and included power levels from 100 to 300 watts, base pressures from 15 to 25 millitorr, and durations

from 5 to 30 minutes. To fully map this space with sufficient resolution would require at least 150 separate processing runs.

Given the complexity of variable interdependence, design of experiment (DOE) for efficient and conclusive research was a necessity. Comparison to a scientific control, blocking to isolate tested variables, and replication to reduce variance ensured accuracy. Fractional factorial experiments and sequential analysis promoted pertinence and efficiency. With three independent variables and the selected test values a full factorial experiment (fully crossed design) would have required 150 separate trials to cover the search space once; however, a fractional factorial design covers the 3-dimensional search space with far less individual tests. As shown in figure 2.7 it was possible to roughly explore the space in 30 initial trials and then 11 additional trials to fully explore the designated area of most interest. Selecting experiment parameters from random walks weighted for unexplored areas resulted in separate tests distributed evenly throughout the search space with approximately equal sized blocks of each independent variable's discrete testable values. Additionally, intelligent choice of test order facilitated the elimination of large blocks of search space and concentrated subsequent tests and multiple retests on relevant areas. By the sparsity-of-effects principle, comparisons of the means of these blocks identified the significant main effects and two-factor interactions[115].

Other influential parameters were held constant as dictated by the intended biomedical wire electrode application or process effectivity. These include frequency (held at 13.56 MHz as is typical for industrial capacitively coupled plasma[116]), plasma

material (argon), sample geometry (wire electrode), sample material (MP35N), and sample positioning (mounted orthogonal to cathode base plate).

Duration (minutes)	Pressure (mTorr)↓	Power (Watts) 100	150	200	250	300
5	15	1				9
	17.5		19			
	20			38		
	22.5		14	28		
	25					
10	15		24	12	18	
	17.5					4
	20			39		
	22.5					
	25				30	
15	15	29		34		
	17.5			35	7	
	20	21	32	31	33	17
	22.5			36		
	25		6	37		

Duration (minutes)	Pressure (mTorr)↓	Power (Watts) 100	150	200	250	300
20	15					
	17.5					27
	20			40		15
	22.5	10		3		
	25				22	
25	15					
	17.5			25	13	
	20		2	41		
	22.5					23
	25	11				
30	15					
	17.5					
	20		26	8		
	22.5	16				
	25			20	5	

Figure 2.7. Design of experiment to explore MP35N texturing by RF plasma as a function of power, pressure, and duration. Initial tests are shown by black numbers. Additional tests by red numbers. And the selected optimal area of interest by shading.

The morphology of formed nanopillars includes structure depth, structure density, aspect ratio, tip radius, coagulation, and the formation of wires or ripple-like wave structures and is influenced by a number of processing parameters. For the present study, processing duration and the RF plasma characteristics of power and pressure were selected for investigation. The following explores and seeks to understand the controls exerted by plasma pressure, power, and duration as well as the interaction between the variables. Process settings were limited to constant values of each parameter of interest per processing run. Future investigations may explore the effect of varying parameter values during a processing run but that is beyond the scope

of this study. The ultimate objective was to increase surface area, primarily by increasing the depth of the nanowire structure formation. The following three sections on processing duration, power level, and base pressure level will all refer to figure 2.8.

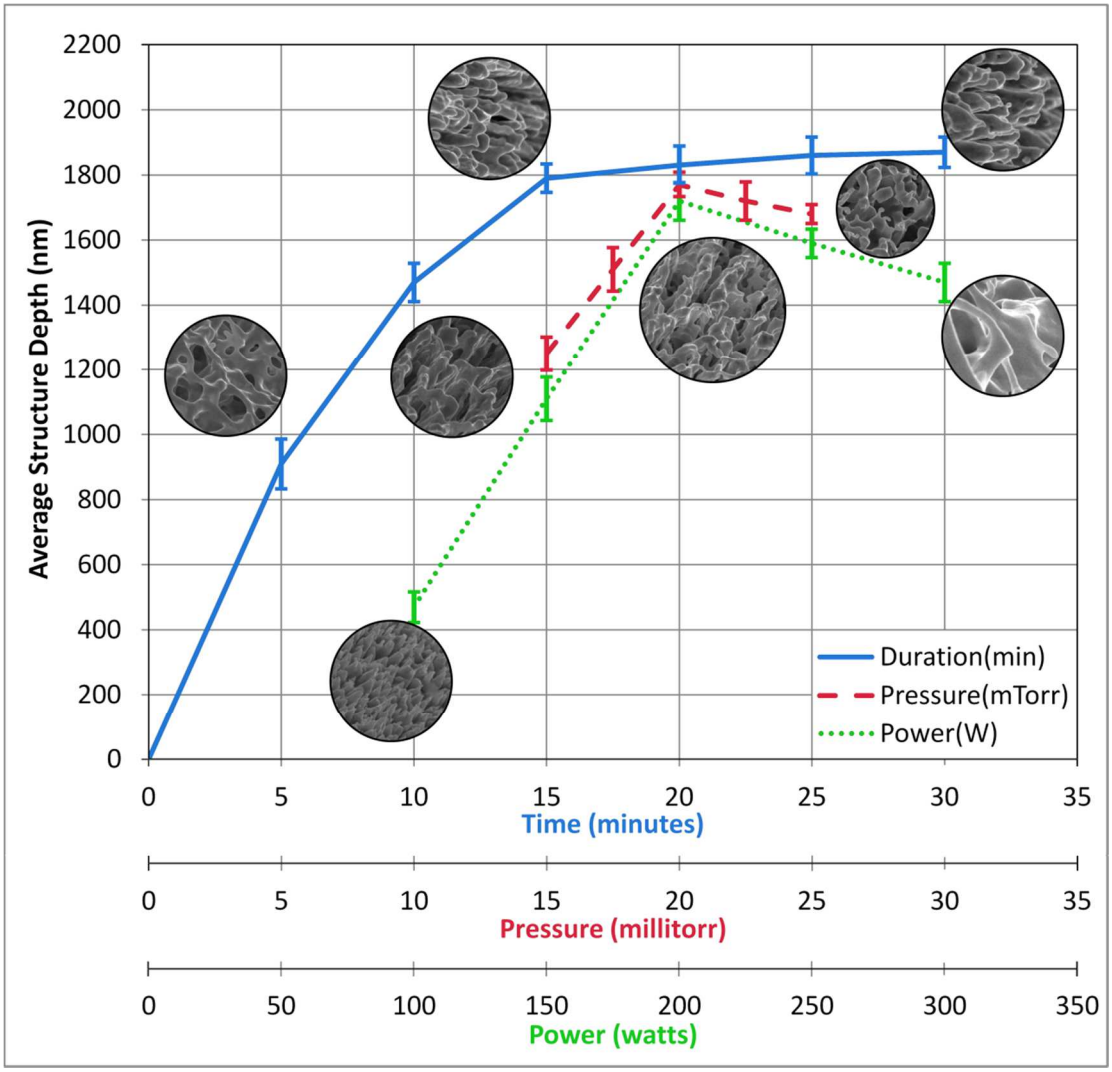

Figure 2.8. Structure depth plot of cross-sectional data for MP35N samples processed in argon RF plasma varied over duration (with pressure held at 20 mTorr and power at 200 W), varied over pressure (with duration held at 15 min and power at 200 W), and varied over power (with duration held at 15 min and pressure at 20 mTorr). Selected parameters: 15 min, 20 mTorr, and 200 W. Error bars indicate first standard deviation of data.

2.4.1 Processing Duration

As shown in figure 2.8, for the cross section shown the other parameters are held at their optimal value (20 millitorr, 200 watts), structure depth as a function of processing duration increases quickly for ~15 minutes before rapidly approaching an asymptotic maximum structure depth of ~1850 nm. Areas outside of the cross section shown in the plot behave similarly but with an overall reduction in peak depth. For areas with higher power and higher pressure structure depth increases more rapidly but does not reach the same peak value. For areas with less power and less pressure, structure depth increases slowly and reaches an asymptote below the optimum cross section. For the odd combinations of higher pressure, lower power and lower pressure, higher power the structure depth increases with similar rapidity but doesn't reach the same maximum depth as the optimal combination. As any increase in the mean measured depth after 15 minutes is statistically insignificant, 15 minutes was selected as the optimal processing time for maximizing structure depth in a single processing run.

2.4.2 Chamber Pressure

Again in figure 2.8, for the cross section shown the other parameters are held at their optimal value (15 minutes, 200 watts), structure depth as a function of chamber pressure increases nearly linearly from ~1250 nm at 15 millitorr to a maximum of ~1800 nm when pressure reaches ~20 millitorr after which the resultant depth decreases to ~1700 nm at 25 millitorr. Outside of the optimal cross section shown in the plot peak depth decreases and overall behavior shifts. For areas with

higher power and longer processing times the suppressed peak depth occurs at a lower pressure and decreases slightly with increasing pressure. For areas with less power and shorter durations, structure depth continues to increase with increasing pressure but with diminishing increases. For combinations of longer durations and lower power, again depth continues to increase with pressure. For higher power and shorter times, structure depth peaks near 20 millitorr before decreasing again. Maximum depth was achieved at 20 millitorr as shown in the optimum cross-section and was selected as the best value for single run structure depth.

2.4.3 Processing Power Level

Finally, for the optimum cross-section shown in figure 2.8 (20 millitorr, 15 minutes), structure depth as a function of power also increases very nearly linearly from ~500 nm at 100 watts before reaching a maximum of ~1700 nm at ~200 watts and then decreasing to ~1500 nm at 300 watts. Outside of the optimum cross-section, varying power has very similar results as the section shown. Over-powering or under-powering the process always decreases the overall depth with optimum values for power always near 200 watts, slightly more for low pressure situations and slightly less for high pressure.

In general, it appears that the power level is the main determining factor for surface melting and decreased depth. Pressure shifts this effect slightly one way or another and short durations can prevent melting. In the case of pressure or power beyond the optimal point, the nanopillar structure shows signs of melting and interlocking resulting in decreased depth. The similar trends exhibited by both power

and pressure variations is likely due to the same development: increased etch rate followed by overheating and melting of the surface in the first case by the increasing velocity of ion impacts and in the second by more frequent ion impacts. The self-limiting characteristic of structure depth seems to be a function of how quickly heat accumulates on the surface and melts the alloy. Maximum depth occurs at the approximate equilibrium point of 15 minutes, 20 millitorr, and 200 watts.

2.5 Sample Geometries

Extending the RF plasma process to geometries beyond a simple wire presents various challenges. First, any sudden orientation changes of the surface normal are susceptible to edge effects as charge accumulates at locations with greater curvature. This uneven accumulation tends to affect and distort the structure formed. For concave or interior portions, shielding also becomes a concern as no texture will form on a shielded surface. Ribbons or foil and sharpened metallic tips were targeted as geometries with worthwhile potential for biomedical applications if they could be successfully textured.

2.5.1 Wire Samples

Wire samples were textured by mechanically fixing one end into the cathode base plate, with the wire extending 7.5 cm vertically towards the anode into the region of highest plasma density. Radial structure was consistent with no preferential etching from any horizontal direction. As shown in figure 2.9, the texturing structure was not consistent for the entire length of wire but rather varied with distance from the

cathode. The upper 3.5 cm of each sample had generally consistent structure and depth whereas the lower portion had little structure.

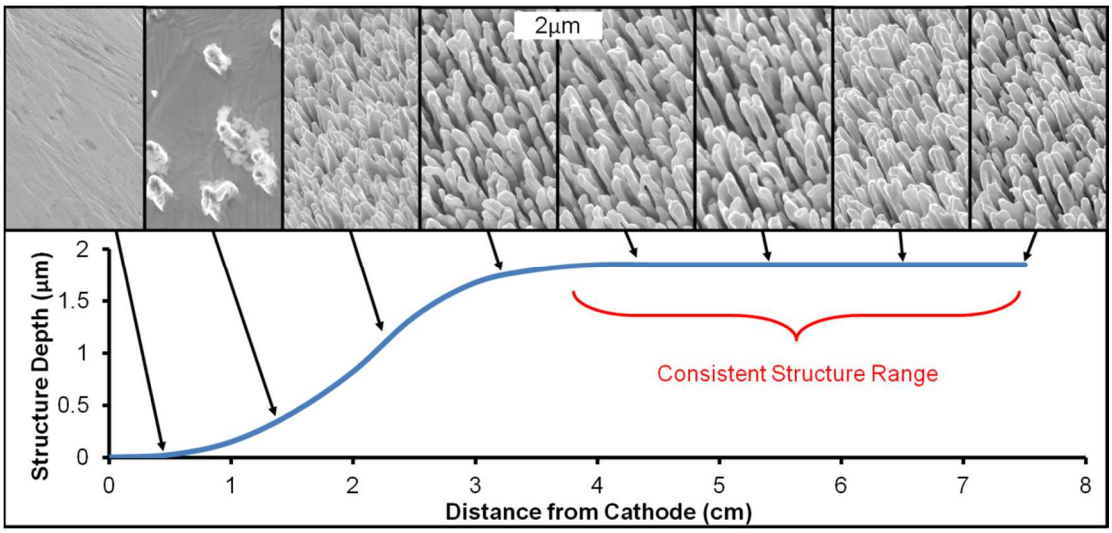

Figure 2.9. Structure depth as a function of distance from the cathode plate with accompanying micrographs. Samples were MP35N processed for 15 minutes at 200 watts in argon RF plasma with a chamber pressure of 20 millitorr.

2.5.2 Foil and Plates

As shown in figure 2.10 and 2.11, nanowire may be formed on both sides of a section of thin foil by supporting a ribbon or plate between two supporting NiCr pillars of 1 mm diameter which are electrically connected to the RF plasma chamber cathode base plate. Nanowire surface morphology on a foil sample shows consistent structure near the center of the ribbon and an elongated structure on the edge due to field effects near the high curvature edge of the foil. Overall structure depth is significantly diminished in comparison to wire samples with little penetration beyond rippling on the surface. Edge regions give the impression of greater depth and larger structures, but actual depth is quite shallow with the elongated features only creating

an illusion. During processing, temperature was apparently lower in the foil samples as they did not incandesce as wire samples do during processing.

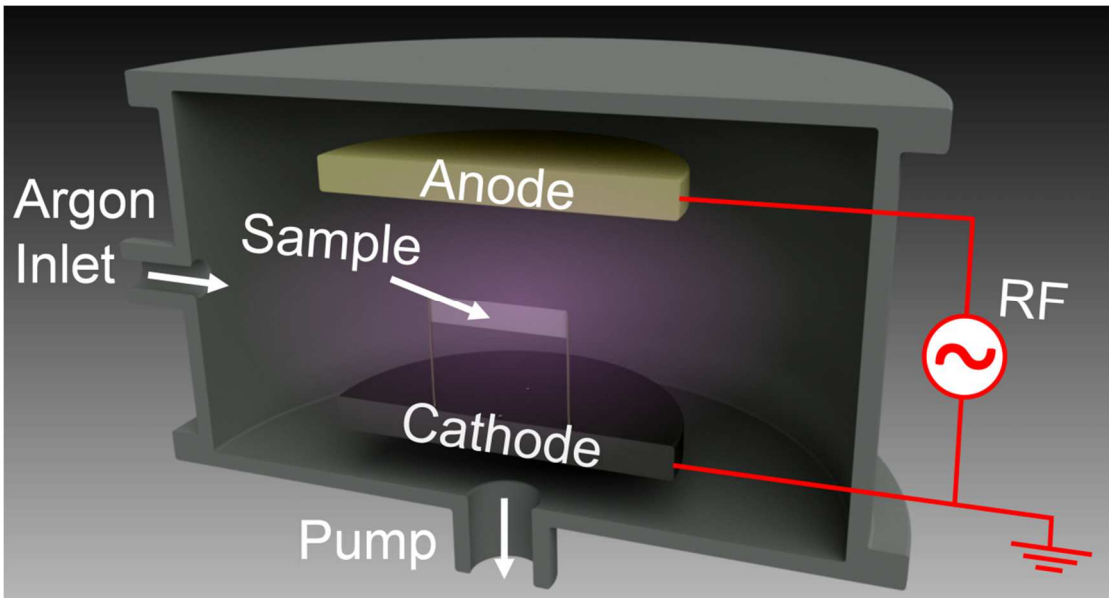

Figure 2.10. Sample configuration for processing of a foil ribbon suspended between two NiCr pillars which are mechanically affixed to the cathode plate.

For texturing on only one surface of foil, the suspended banner may be rolled into a ring and supported by NiCr pillars on opposing sides. Nanotexture will only form on the outward facing side of the ring while the interior is shielded and develops no texture. Also notable is the lack of texture development in the region near any supporting pillar due to either shielding or excessive heat transfer. Similarly, thin plates may be textured as shown in figure 2.11 by suspending the sample with a NiCr pillar connected to the cathode base plate, however areas adjacent to the supporting pillar will not develop texture. Plate texturing is consistently more difficult than either wire or foil texturing and structure tends to be more sparse and to not develop at all near edges.

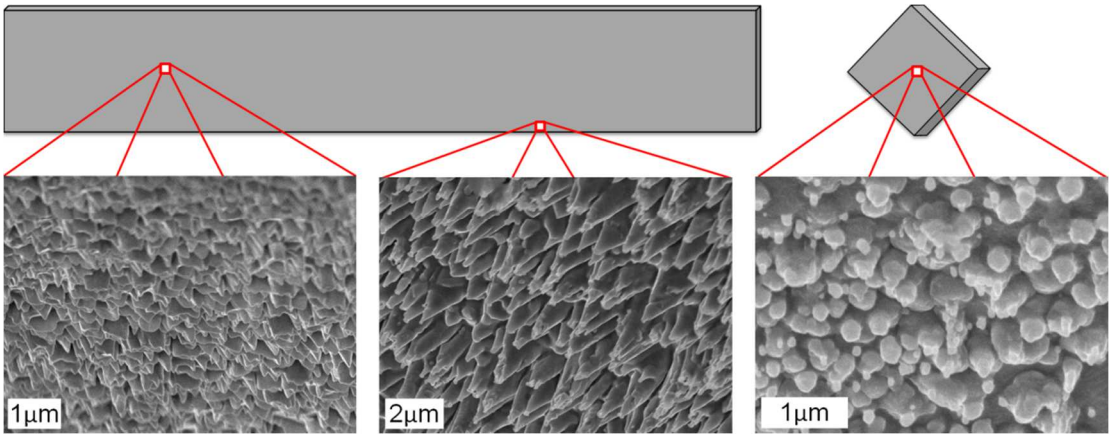

Figure 2.11. Micrographs and locations of texture on RF plasma processed foil and plate samples showing elongation near the foil edge and minor texturing near the sample center.

2.5.3 Sharpened Tips

Texturing metals which have been reduced to extremely small diameter tips could have some potentially important applications for biomedical research such as cell-poking, drug delivery, or energy harvesting. Figure 2.12 shows the basic approach of sharpening MP35N by electrochemical etching, followed by RF plasma texturing.

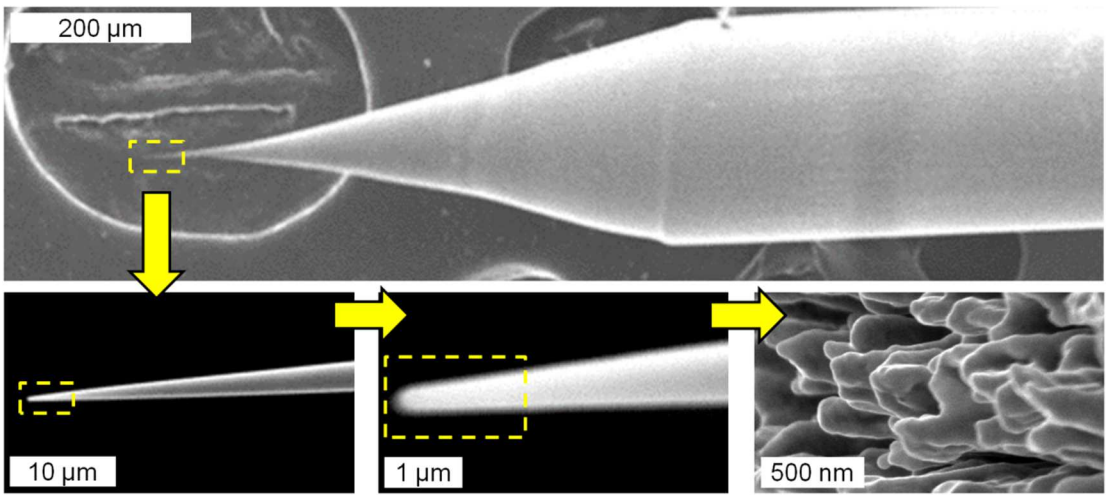

Figure 2.12. Proposed design for sharpened and textured device. MP35N wire electrochemically sharpened to produce an extremely fine tip. RF plasma processing then applied to texture the sharp tip.

RF plasma processing does produce radial texturing on the tip of sharpened MP35N, however, if too much power or pressure is applied, then the tip tends to melt and agglomerate, reducing the tip diameter. Even at a low level of 75 watts and 15 millitorr argon RF plasma, tips tend to form small globs as shown in figure 2.13. Final tip radii remain reasonably small but would need to be reduced further for use in most cell poking applications. One approach would be to electrochemically sharpen the MP35N tip, process at low power and pressure, and then electrochemically resharpen slightly to reduce the final tip diameter while still maintaining some of the texture. Notably, the surface texture near the point does not show the edge effect distortions as might be anticipated

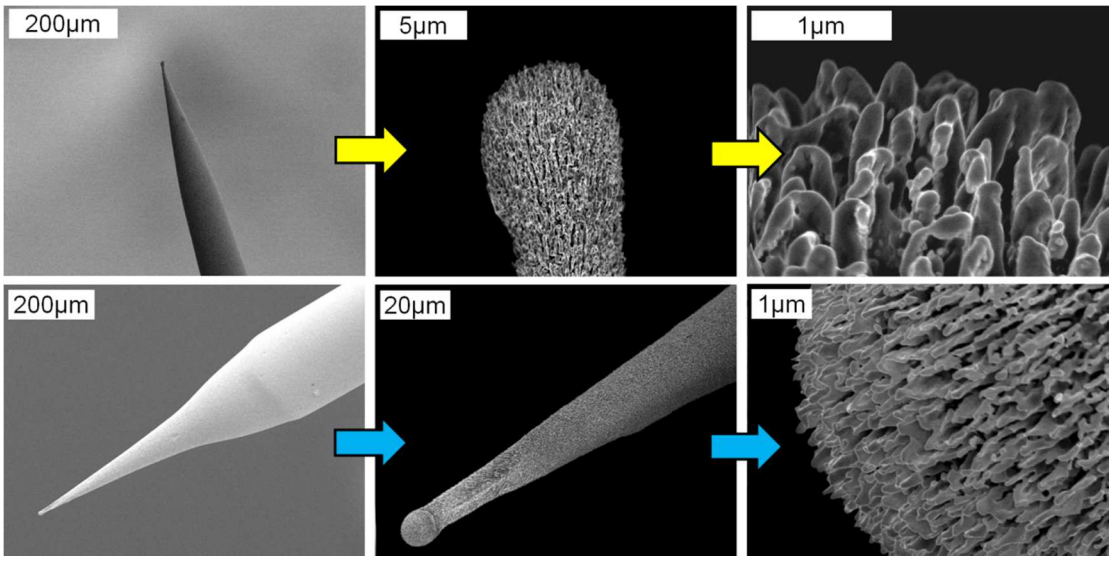

Figure 2.13. Two examples of sharpened MP35N wires that have been processed in low-power, low-pressure argon RF plasma to produce nanotexturing at the sharp tip. Tip radius was increased from 1-2 µm and material tended to agglomerate on the furthest end, likely from melting during processing.

2.6 Sample Materials

To this point, nearly all processing work had been done in MP35N biomedical alloy. The working theory being that multiple-phases and preferential etch rates were required for surface structure development and that single phase materials could not be textured with this procedure.

2.6.1 Multi-Phase or Single Phase Alloys

During experiments with various geometries as discussed in section 2.5, thick NiCr wire was used to support MP35N foil and surprisingly the nichrome surface textured as well as anything observed in MP35N. However, as figure 2.14 indicates, nichrome in the range of processing temperatures remains in the single-phase region.

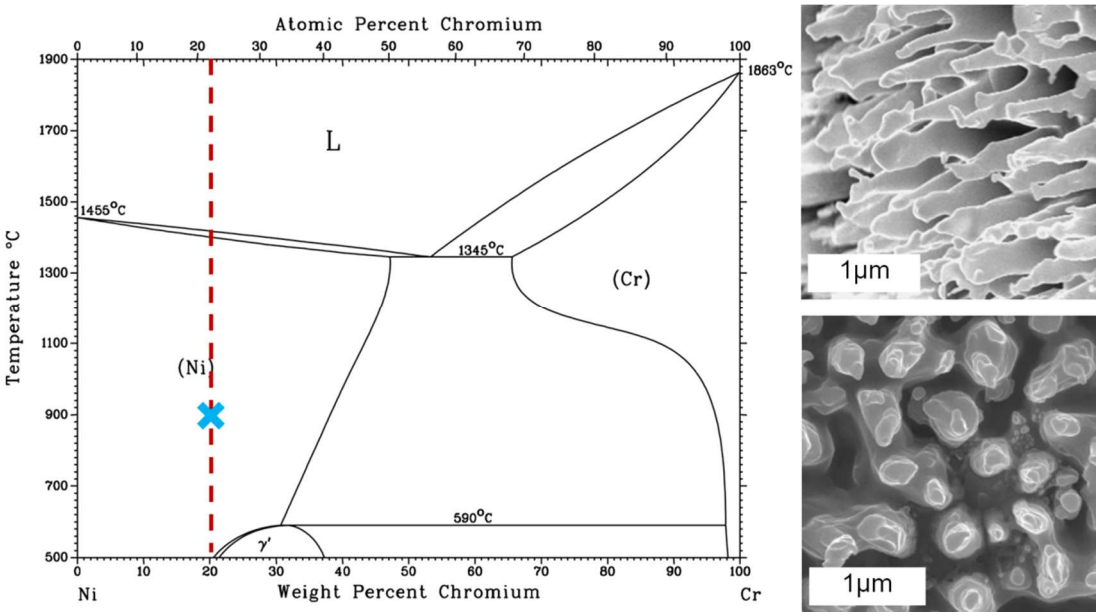

Figure 2.14. Nickel-chromium phase diagram (wt. %) with dotted line indicating 80/20 nichrome and 'X' marking RF plasma processing temperature as being in a single phase region. Micrographs at right are Ni-Cr (80/20) textured surface following RF plasma processing in argon at 200 watts for 20 minutes with a chamber pressure of 20 millitorr.

Single-phase Ni-Cr (80/20) texturing in RF plasma did not fit with the earlier theory of a multi-phase mechanism to texturing. In fact, Ni-Cr wires textured a bit deeper on average than either the MP35N or Pt-Ir samples that were successfully textured previously. In section 2.7, alternative possible mechanisms will be discussed. Following, the successful texture of nichrome a variety of other materials were effectively textured including inconel alloy, copper, 316L stainless steel, and 304 stainless steel in addition to MP35N, Ni-Cr (80/20), Pt-Ir (90/10), Pr-Ir (85/15), and Pt-Ir (80/20). Refer back to figure 1.2 for images of various textured materials. Other materials such as titanium, tantalum, and platinum proved more difficult and required additional procedures and methods as discussed in the following sub-section.

2.6.2 Alternative Texturing Procedures

For materials that couldn't be textured by the typical RF plasma procedure, it was necessary to develop a procedure of transferring texture from a material which could be textured to one which couldn't. As diagramed in figure 2.15, texture transfer etching may be accomplished by sputter depositing a texturable alloy such as Ni-Cr in a sufficiently thick layer onto an underlying substrate targeted for texture. The coated substrate is then subjected to RF plasma, texturing the coating material. Continued exposure to the RF plasma etches away the top layer coat and imprints the texture pattern onto the underlying surface. Once all the deposited material is etched away, only the target material remains and now has a textured surface. This method is useful for producing basic surface level texturing but does not allow for any significant

depth. Continued exposure beyond removal of the deposited material tends to progressively reduce the texturing in the target substrate.

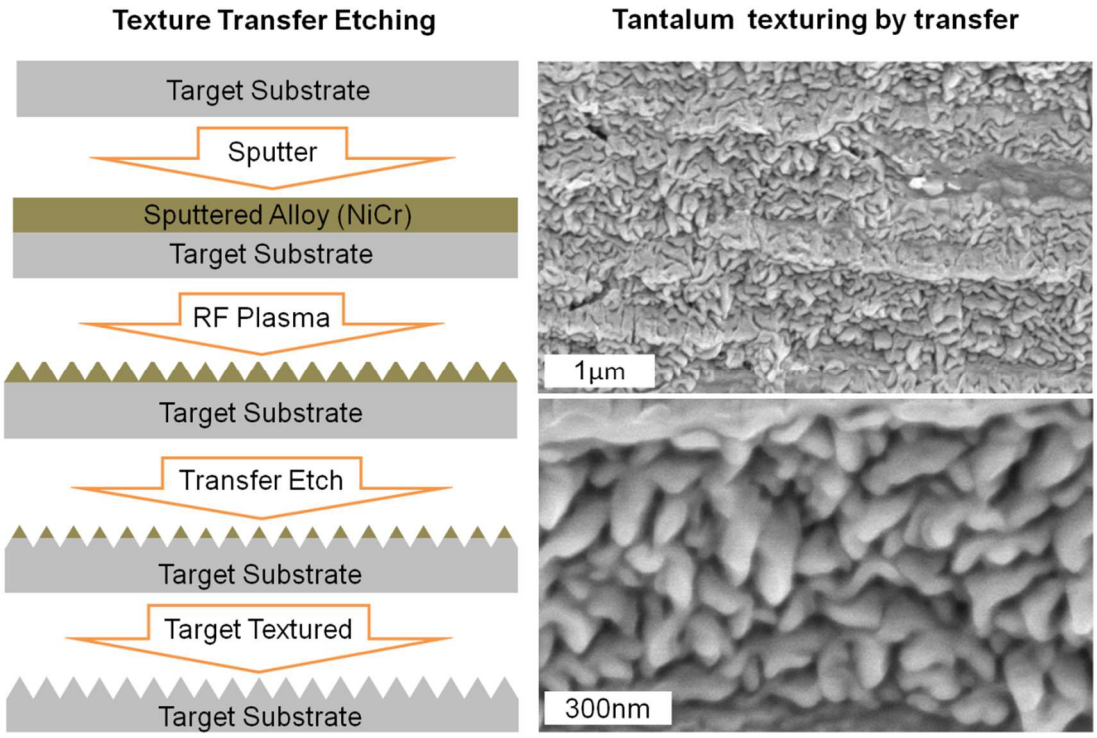

Figure 2.15. Texture transfer etching accomplished by sputter deposition on a target substrate, RF plasma texturing, and then transfer etching into the target material. Micrographs depict a textured tantalum surface accomplished by sputter deposition with 750 nm Ni-Cr followed by RF plasma texturing for 30 minutes at 200 watts in 20 millitorr argon base pressure.

If only the surface material is important but not the underlying substrate, another option to produce texture in a particular material is to first texture a susceptible material such as MP35N or Ni-Cr and then to deposit the desired material onto the textured surface, retaining some of the texture in the deposited layer. This method has been successfully applied with platinum coating a pre-textured MP35N substrate.

2.7 Mechanism

Introduction sections 1.2.4 and 1.2.6 established the original hypothesis that materials must satisfy two conditions in order to be texturable by RF plasma: multi-phase materials and different sputter etch rates among species. However, the extension of RF plasma texturing to single-phase Ni-Cr (80/20) among other materials in section 2.6.1 effectively ruled out the original hypothesis as being the only mechanism for texturing. Still, preferential sputter-etch rates and multiple phases likely still play some role and so will be discussed in section 2.7.1 before other options are explored.

2.7.1 Phases

MP35N wire samples have a multi-phase structure containing face-centered cubic (FCC) and hexagonal close-packed (HCP) phases[117]. Likewise, at lower temperatures (<900°C), the Pt-Ir wire samples exhibit a miscibility gap and hence phase separation[118]. The RF plasma process used to texture wire surfaces is a sputter etch process resulting in a loss of surface material. Sputter etching is not necessarily a uniform surface etch process. Temperature driven diffusion, and the chemical or geometrical surface inhomogenieties, may contribute to non-uniform etching and the formation of protruding ripples or nanowire type structures.

One possible explanation is that the presence of separate phases in the MP35N or Pt-Ir wire material contributes to the formation of nanowire/nanopillar geometry after RF processing, as different metals/phases exhibit substantially different sputter etch rates. Among the elements involved in the MP35N alloy for example ((35% Co–35% Ni–20% Cr–10% Mo in wt.%), the sputter etch rate of nickel and cobalt more

than double the etch rate of molybdenum. RF plasma texturing has also been investigated for Fe-Ni, Fe-Cr, and Fe-12% alloy wires and pure Pt, W, and Cu wires but has not obtained any substantial nanotexturing of the surface, perhaps due to single-phase microstructures or phases with similar etch rates. However, nanoscale surface texturing has been successfully produced on single phase Ni-Cr (80%Ni–20% Cr) wires. The RF plasma texturing technique remains a novel process in need of continued research. Further exploration of wire sample materials will illuminate the role phase structure and relative etch rates play in surface texture formation.

2.7.2 Ion Bombardment

Another possibility for the formation of nanoscale surface texturing relies on ion bombardment of the surface. As shown by Sigmund[119], assuming random slowing-down of bombarding ions at locally oblique incidence, the most prominent sputtering yield enhances small irregularities on a relatively smooth surface. It has been shown that sharp cone structures erode more slowly under high ion-bombardment than flat surfaces. When an ion impacts a surface at an angle, the energy is deposited with an elongation along the impinging angle and the point of maximum sputtering yield is farther down the surface from the impact point. In combination with the cross sectional likelihood of an ion impacting a particular point on a rough surface, small irregularities on a relatively smooth surface are enhanced by ion bombardment; sharp cone structures erode more slowly under ion bombardment than flat surfaces; and stable ripple or nanowire formations could result from bombardment. Notably, the

surface structure of MP35N when textured by nitrogen RF plasma very closely resembles the predicted cone-shaped texturing as shown in figure 2.16.

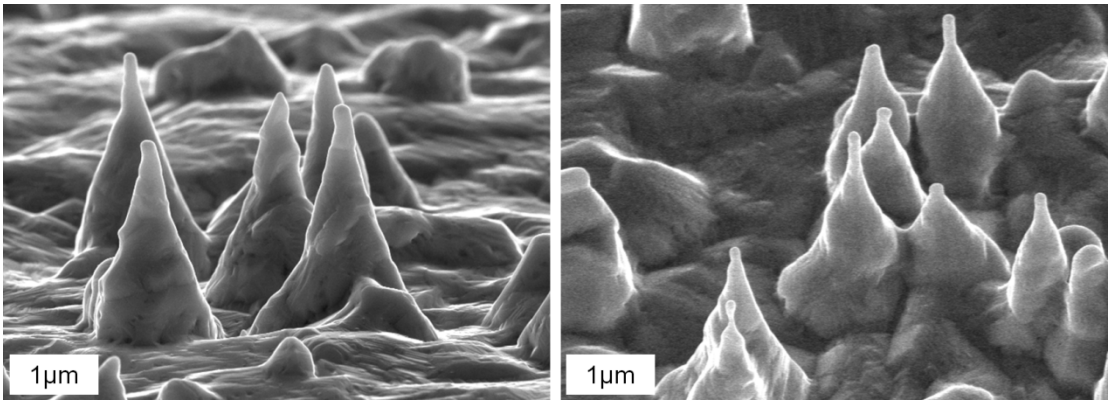

Figure 2.16. Conical surface structures on the surface of MP35N processed in nitrogen RF plasma.

Thus, exposure of the wire surface to RF plasma may result in the ripple or nanowire formations as stable structures during bombardment. If ion bombardment is the primary mechanism in RF plasma surface texturing of metallic wires, under the right conditions structure could be produced with any metal material subject to ion bombardment. Thus far, this has not been the case for the RF plasma texturing technique but further investigations may show the necessity of material-specific processing parameters in producing surface texture.

2.7.3 Microstructure Irregularities

Another possibility for nanopillar formation in metal alloys exposed to the RF plasma is the exploitation of inherent random weaknesses in the polycrystalline wire samples such as the discontinuities present at grain boundaries or dislocations scattered throughout each grain's lattice structure. Perhaps these discontinuities result in weak spots near the surface of the material that are more easily etched by exposure

to RF plasma. The energy imparted by the bombarding ions may allow the rapid movement and accumulation of these imperfections at the surface of the electrode wire thereby shaping its morphology.

It's also possible that these discontinuities result in weak spots near the surface of the material that are more easily etched by exposure to RF plasma. Increased localized etch rate due to these imperfections could possibly explain the formation of a nanotextured surface. Such a model may account for the observed self-limiting structure depth as these internal imperfections would annihilate upon encountering the surface. Unfortunately, at present in situ observation of the surface development and internal structure has not been possible so the idea remains untested. Comparisons of annealed and un-annealed samples however do not exhibit noticeably different texturing structures as would be expected if unreleased grain imperfections played a primary role in texture development. Further research is needed in this area.

At present it appears that the nanotexturing produced by RF plasma is based on a complicated interaction of ion bombardment, material crystal structure, and possibly imperfections in that structure. No single factor appears to be primarily responsible. Perhaps one dominates in some circumstance and another in differing circumstances. Further developments in chapter 3 add greater clarity to this complicated mechanism.

This chapter, in part, is reproduced or adapted from material as it appears in Acta Biomaterialia, "Controlled Metallic Nanopillars for Low Impedance Biomedical Electrode" Volume 10, Issue 5, Pages 2296-2303 (May 2014). Jonathan Trisnadi, Tae

Kyoung Kim, Karla Brammer, Lina Reiss, Li-han Chen, and Sungho Jin are co-authors. The dissertation author was the primary investigator and author of this paper.

Chapter 3: Repetitive Processing to Deepen Texture

Having determined the best parameters to achieve structure depth on a single run through the RF plasma process, the next step was to investigate if the heating and cooling portion of processing a sample could further enhance structure depth or if only total processing time would contribute to the final structure. To overcome self-limiting structure depth, additional processing runs were introduced at the optimum power, pressure, and duration parameters.

3.1 Subdivided Processing

The initial objective was to determine how the sample heating or cooling portion of processing runs affected structure depth in comparison to total processing duration. The self-limiting depth of texturing raised the possibility that once a temperature equilibrium is established further deepening is precluded. As an easy test, total processing time was held constant at 20 minutes but five different trials were conducted with differing divisions of the total time: 1x20 min, 2x10 min, 4x5 min, 10x2 min, & 20x1 min. The chamber was evacuated between processing divisions with each repetition separated by 30 minutes. Samples were not exposed to oxidizing agents between processing runs. Results are presented in figure 3.1 and show a successfully increased structure depth to ~2300 nm for the 2x10 min trial. Additional subdividing for the 4x5 min (~1600 nm), 10x2 min (~1200 nm), and 20x1 min (~900 nm) trials resulted in progressively decreasing structure depths. The importance of the initial heating or cooling of samples was confirmed for further testing.

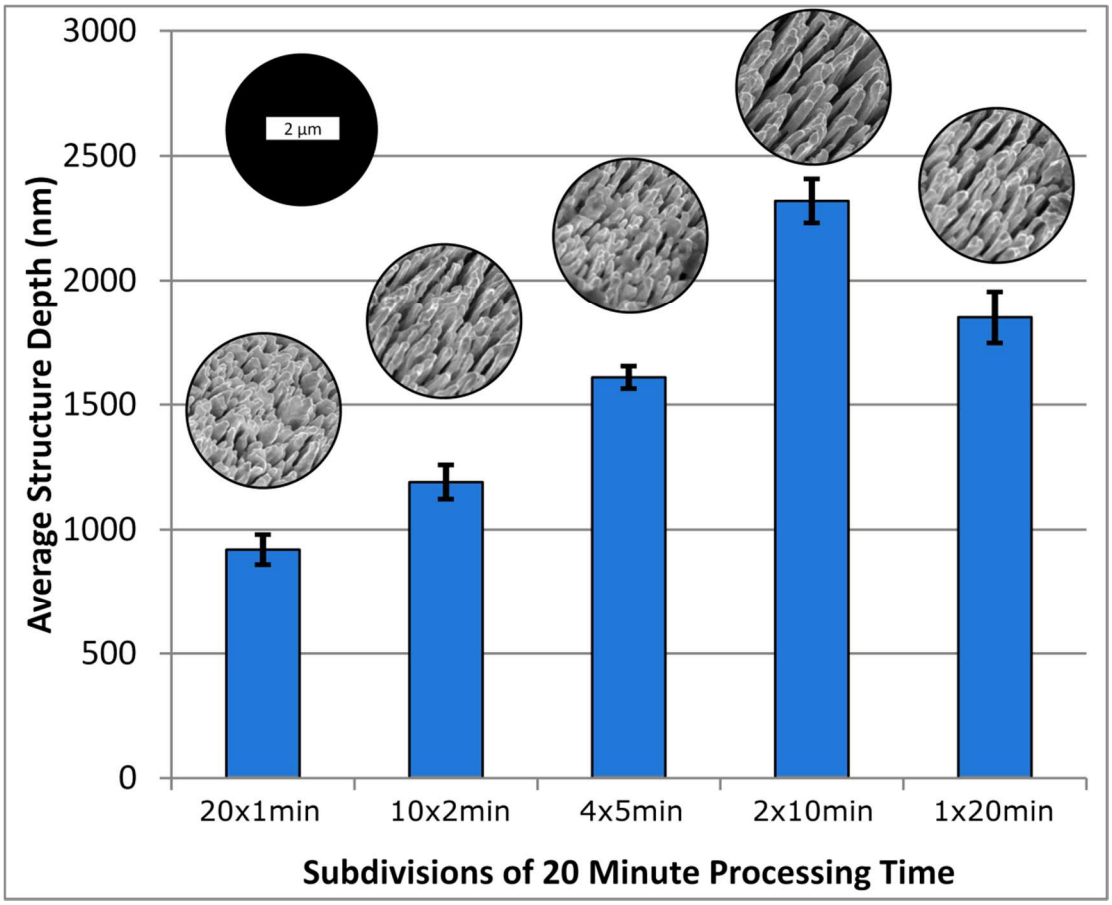

Figure 3.1. Total time held constant, subdivided trials of MP35N samples in argon RF plasma to test the effect of heating and cooling on structure depth. (Subdivisions: 1x20 min, 2x10 min, 4x5 min, 10x2 min, & 20x1 min). Deepest structure in 2x10 min samples indicates that repetitive heating and cooling may lead to deeper structure as long as the individual durations aren't too short. Error bars indicate first standard deviation of data.

3.2 Fully Repeated RF Plasma Texturing

To further increase structure depth, multiple in chamber repetitions separated by 30 minutes were introduced at the previously selected optimal power, pressure, and time and successfully continued to deepen the structure. As before, samples were kept in the evacuated chamber and not exposed to oxidizing agents between processing runs. As shown in figure 3.2, each successive step resulted in ~500 nm deeper

structure with slightly diminishing returns. Repetitive processing at the optimized values of 15 minutes, 200 watts, and 20 mTorr in argon plasma resulted in significantly deeper structures and increased overall surface area.

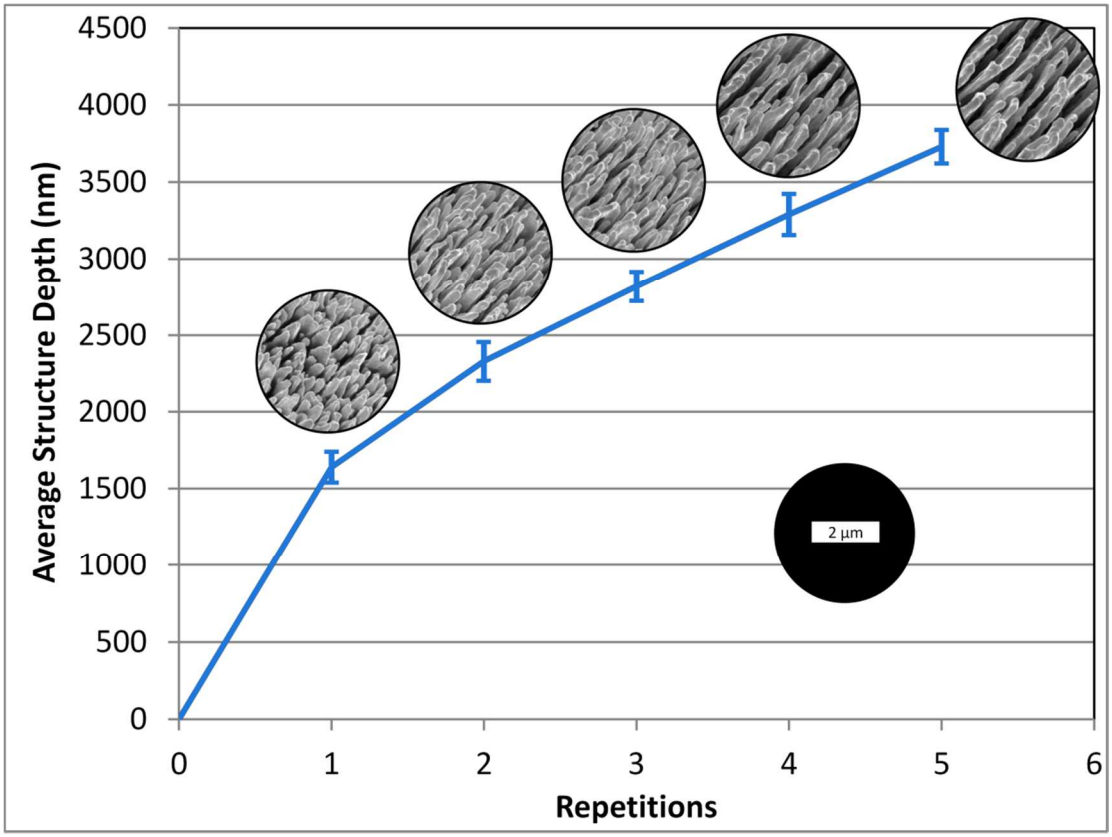

Figure 3.2. Repetitive processing of MP35N in argon RF plasma (15 min, 20 mTorr, 200 W) shows continually increasing structure depth, exceeding any structure formerly obtained by single runs. Error bars indicate first standard deviation of data.

In addition to the increased structure depth, the separation between pillars also became more pronounced and the nanowires more characteristically elongated. Diameter of the surface wires was consistent from base to tip before an abrupt rounded end. Figure 3.3 shows an MP35N wire after 10 successive RF plasma processes, with a total structure depth of ~7-10 µm. With higher repetitions, nanowire formations

show signs of accumulating into ripples wrapping radially around the perimeter of the textured MP35N wire.

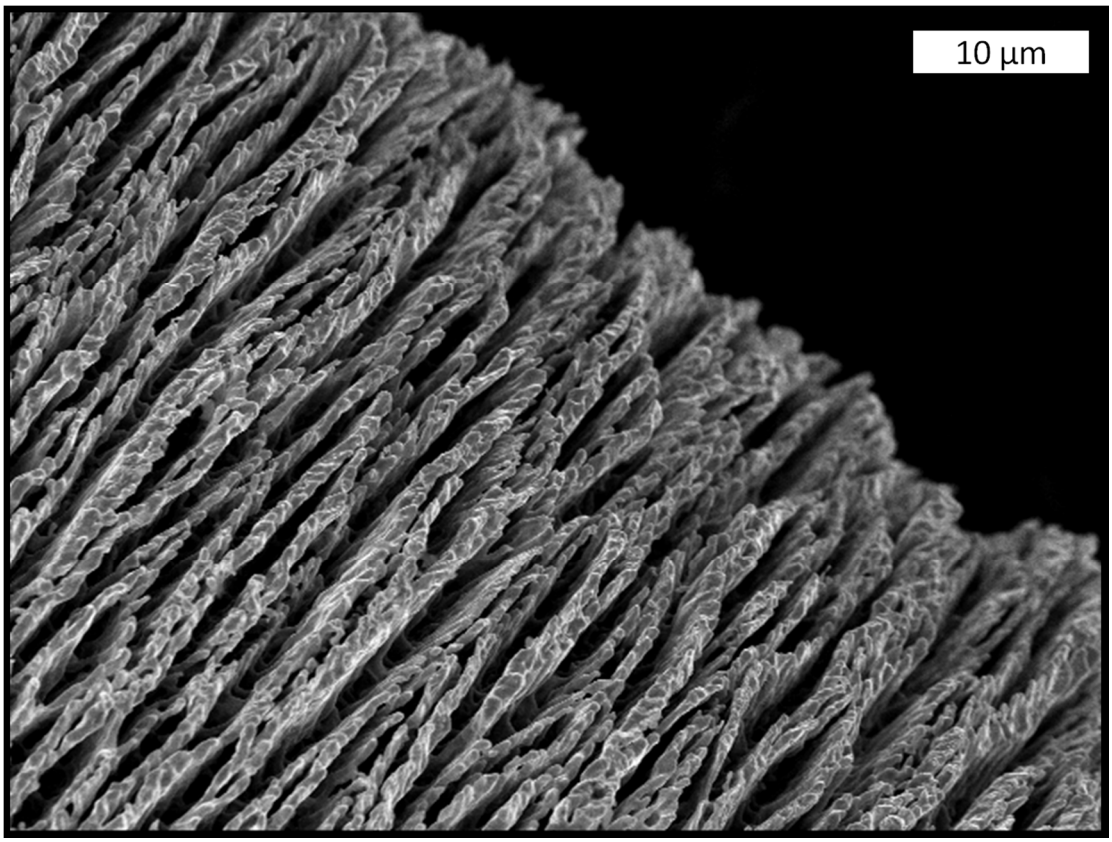

Figure 3.3. MP35N sample repetitively processed 10 times in argon RF plasma for 15 minutes, at 20 millitorr and 200 watts. Structure is significantly deeper (~7-10 µm) than attained in any previous trial.

3.3 Material Loss from Repeated Texturing

RF plasma texturing is an etching process which removes material from the samples continuously during processing. For higher repetition numbers, material loss can become an issue as samples may be severed once enough material is etched away. Figure 3.4 plots the mass loss per surface area for a range of processing runs and repetitions. Mass lost per surface are per unit time from the processed MP35N samples is highly consistent across repetition number and process duration. Regression analysis

revealed an average loss of 51.3 µg per mm^2 per minute with a high R-squared value of 0.9956 indicating a very linear fit. Introducing repetitions does appears to very slightly decrease mass lost, perhaps due to time spent heating the sample before reaching equilibrium.

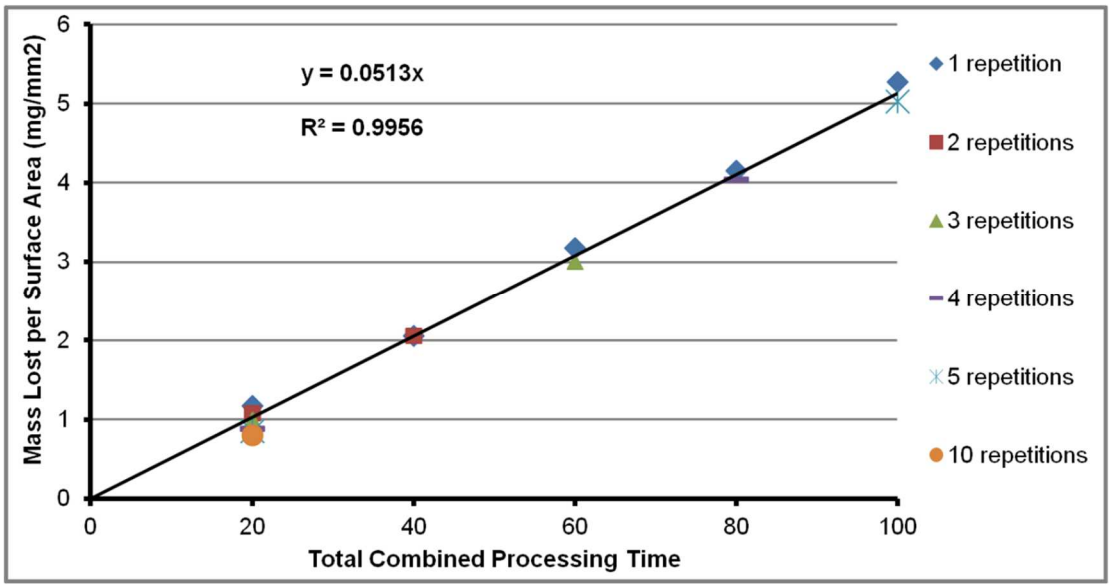

Figure 3.4. Mass lost per surface area from MP35N samples processed at 200 watts in argon RF plasma with a chamber pressure of 20 millitorr.

3.4 Repetitive Texturing of Alternative Geometries and Materials

Multiple run texturing of wire MP35N markedly increased surface texture depth. This improvement was consistent for wire samples of other materials such as Ni-Cr (80/20), Pt-Ir (80/20), and 304 stainless steel. Continued deepening was observed with no limitation other than the amount of material lost to etching. Electrochemically sharpened MP35N also exhibited increased structure depth with repeat processing, though tip diameter was reduced further with each successive step to deepen structure as additional material melting led to agglomeration of the tip.

Wires with diameters ranging from 1 mm down to the 5 μm tips sharp tips all exhibited increased structure depth with repetition. However, for foil geometries repetitive texturing was less successful. Repetition on MP35N foil and Ni-Cr (80/20) improved texturing near the foil edges but did not have as much of an effect on increasing structure depth. Likewise for thicker plates, repetitive processing resulted in more coverage on the plate but did not appear to deepen the texture.

3.5 Diminishing Returns and Maximal Texturing

At present the only limitation on increased structure depth is the initial amount of material available to be etched away by repetitive texturing. It seems that with sufficient processing time especially deep textures could be created before the wire loses structural integrity from material loss. There is a slight indication of diminishing returns with each successive repetition but sufficient data has yet to be collected before the wire is etched away entirely. If in fact less depth is added with each successive repetition, then there may be a theoretical limit to potential texturing depth. Also of consideration is the effect of increasing wire diameter to provide for increased material loss. This is fertile ground for future investigations into metal texturing.

3.6 Theorized Mechanism

It is apparent that repetitive processing does affect structure depth, and including multiple cycles of heating and cooling can result in a deeper structure than a single processing run could produce. The mechanism for continued deepening is not yet well understood but indicates the importance of surface heating and cooling in the

formation of nanowire morphology as opposed to steady state processing. It is possible that the grain morphology of the underlying polycrystalline alloy interacts with the surface during heating/cooling and the energy released by slight annealing results in structures permitting further deepening upon ion bombardment. In any case, the importance of reaching the correct temperature level between surface melting and surface reorganization without full melting is important. Overpowering the process results in metal structures with obvious signs of melting at the surfaces as shown in figure 3.5.

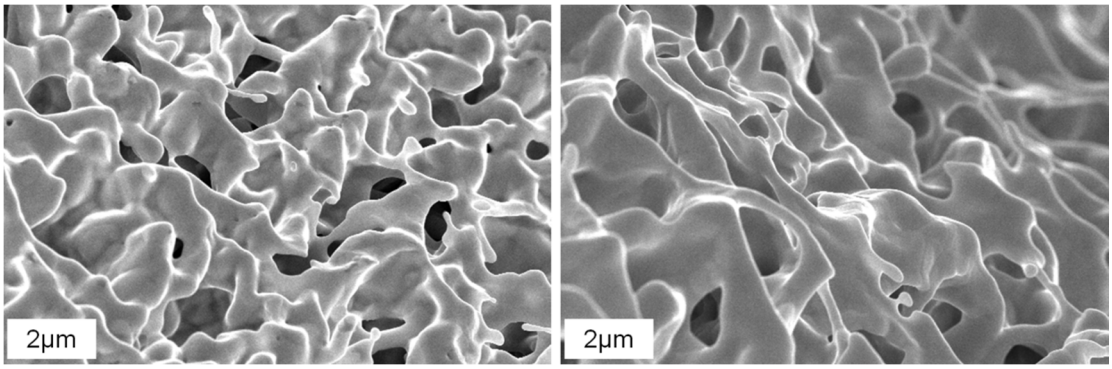

Figure 3.5. MP35N surface after processing at 300 watts for 20 minute in 20 millitorr argon RF plasma. Both micrographs show evidence of surface melting.

It is also possible to speculate that after initial texturing by ion bombardment, perhaps each additional time the sample is exposed to RF plasma, uneven resistive heating across the wire due to the skin effect may leave the preferentially heated base region of surface nanopillars more susceptible to etching by impinging argon ions than the tips of the nanopillars. Then once the wire reaches thermal equilibrium, the temperature difference between base and tip may be insufficient to facilitate further deepening for which additional repetitions must be introduced. Reliance on the skin effect would also account for the decreased effectivity of repetitions for non-wire

geometries. Still, at the scale under consideration, it is doubtful that temperature differences between the base and tip of surface nanowires would be sufficient to effect differing etch rates.

3.7 Endothelialization on Repetitively Textured MP35N

The nanopillar arrays produced by RF plasma surface texturing on the metallic surfaces of MP35N and Pt-Ir alloys has demonstrated superior cell growth, more continuous monolayer formation, and overall improved integration with cell structure as shown in figure 3.6. The nanotextured surface significantly improves cell performance with highly organized monolayer cell layer formation and healthy cell-to-cell junctions present on the textured surface but clumping and irregularity characterizing the untextured surface. The favorable performance of cell growth on nanotextured electrodes is encouraging as a potential avenue to mitigate cell response and maintain low impedance throughout the device's employment or perhaps to extend the device lifespan. Integration within the cell network may help reduce scar tissue encapsulation and the associated loss in electrode performance.

Cell morphology is highly similar to earlier results which also included promising cell adhesion (7 day), actin immunofluorescence (3 day), and oxidative stress (3 day) assays on RF plasma textured MP35N substrates[6]. That work detailed the number of adhering BAECs on textured MP35N after 1 day incubation was six times greater than on untextured MP35N, and after seven days incubation the cell adhesion on textured MP35N was 50-60% better than on untextured MP35N and had reached confluency; actin immunofluorescence showed prominent cortical bands at

cellular junctions and cytoskeletal organization for BAEC culture on textured MP35N but less pronounced cortical bands and no apparent cytoskeletal organization for culture on untextured MP35N; and oxidative stress levels in BAECs grown on textured MP35N were reduced ~40% when compared to untextured MP35N[6].

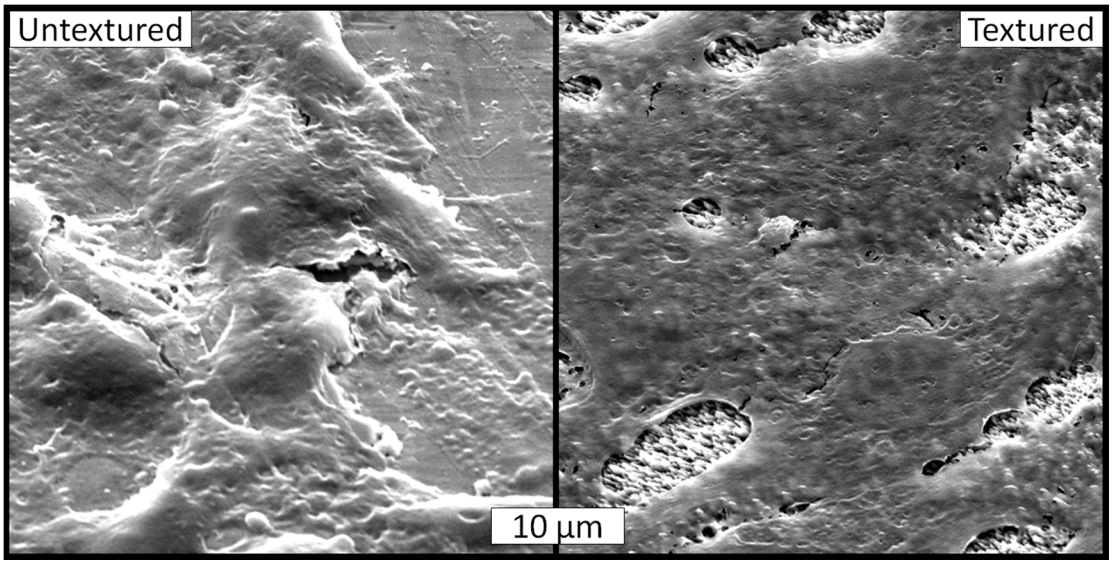

Figure 3.6. SEM micrographs of bovine aortic endothelial cells (BAECs) on non-textured vs. textured surfaces after 3 days of incubation. The cells on the textured surface (right) form a smooth, continuous intercellular layer with desirably tight junctions between cells. BAECs on the non-textured surface (left) are clustered, lacking a continuous monolayer structure.

This chapter, in part, is reproduced or adapted from material as it appears in Acta Biomaterialia, "Controlled Metallic Nanopillars for Low Impedance Biomedical Electrode" Volume 10, Issue 5, Pages 2296-2303 (May 2014). Jonathan Trisnadi, Tae Kyoung Kim, Karla Brammer, Lina Reiss, Li-han Chen, and Sungho Jin are co-authors. The dissertation author was the primary investigator and author of this paper.

Chapter 4: Low Impedance RF Plasma Textured Electrodes

Chronic electrode implants may stimulate or record electrical impulses adjacent to electrically excitable biological tissue. However, tissue response to an implanted electrode tends to degrade signal quality over time as the foreign material is encapsulated by insulating scar tissue and decreased charge transfer from between tissue and electrode. One possible approach to extending electrode life is increasing its sensitivity in recording neuronal signals or its efficiency in delivering electrical stimulation by increasing electrode surface area.

4.1 Surface Impedance and Double-Layer Capacitance

Surface electrical impedance opposes current flow from electrode to tissue for stimulating or tissue to electrode for neural recording. Poor charge transfer from high impedance decreases the efficiency of a stimulating electrode and the resolution of a recording electrode. Electrode surface area is inversely related to surface impedance with total impedance being determined by the double-layer capacitance of the electrode surface and the adjacent electrolyte material[11,120,121]. Increasing electrode surface area at the interface increases capacitance and decreases the impedance.

Double-layer capacitance at the surface interface consists of a charged layer at the surface of the metallic electrode with a thickness on the order of 0.1 nm[122]. The Debye length thickness of the charged layer in the electrolyte depends on molecule size and ion concentration. For undiluted phosphate-buffered saline solution, Debye length is on the order of 1 nm and increases as the solution as diluted reaching approximately 15 nm for a 10^{-4} molar concentration[123]. The important takeaway is that

the total thickness of the double-layer capacitance inner Helmholtz plane for an RF plasma textured electrode is on the order of nanometers and is sufficiently small to follow the surface texture and pores which are on the order of 200-300 nm as shown in figure 4.1. Thus, the entirety of the textured surface area can contribute to the decrease in surface impedance.

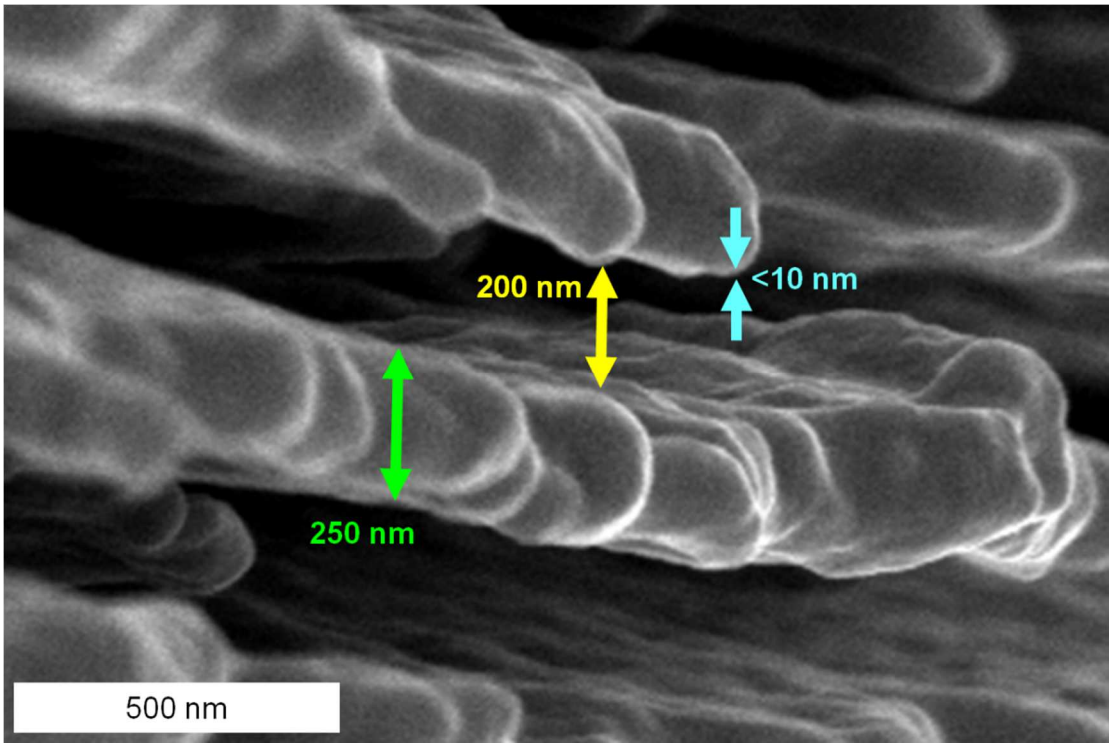

Figure 4.1. High magnification SEM micrograph of RF plasma textured MP35N showing nanowire thickness, separation, and approximate Debye length for phosphate-buffered saline electrolyte with ion concentrations above 1 mM.

4.2 Surface Area Increase of RF Plasma Textured Samples

By assuming a repeating structure for a textured surface it is possible to estimate the increase in surface area from RF plasma processing. Figure 4.2 shows a representative unit cell based on hexagonal packing of vertical cylinders. From the

assumed unit cell, calculating the ratio of textured surface area to flat surface area is straightforward:

$$\boldsymbol{R = 1 + \frac{2\pi dh}{\sqrt{3}b^2}}$$

where $\boldsymbol{R}$ is the ratio, $\boldsymbol{d}$ is the estimated pillar diameter, $\boldsymbol{h}$ is the estimated pillar height, and $\boldsymbol{b}$ is the center-to-center separation distance of pillars.

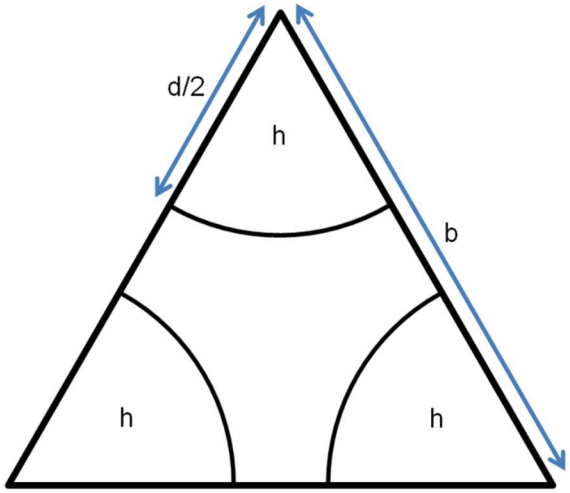

Figure 4.2. Representative unit cell for hexagonal packing of vertical cylinders with cylinder height (h), cylinder diameter (d), and center-to-center separation (b) indicated.

4.3 Decreased Impedance from Repetitive Texturing of Wire Electrodes

Surface impedance of RF plasma textured MP35N and Pt-Ir electrodes was characterized in a typical three-electrode electrochemical cell as depicted in figure 4.3 with a 25 cm^2 Pt counter-electrode and an Hg-free Ag/AgCl single junction high temperature reference electrode (Fisher Scientific accumet Glass Body) with electrode separation held constant. Dulbecco's Phosphate-Buffered Saline (PBS) was employed as an electrolyte to simulate physiological conditions with 1M concentration.

Reference electrode was placed as near as possible to the working electrodes to reduce ohmic drop during voltammetry.

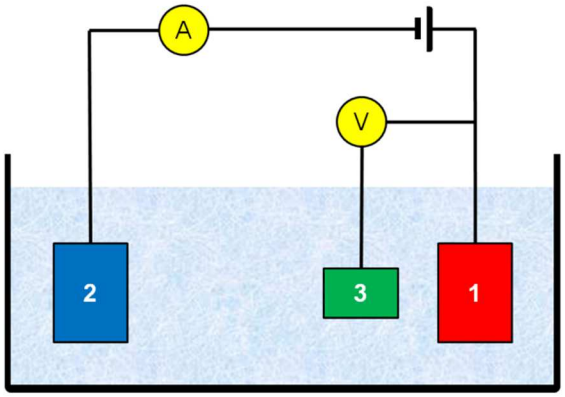

Figure 4.3. Three-electrode system for voltammetry with (1) working electrode, (2) counter-electrode, and (3) reference electrode showing (V) electric potential and (A) current measurements.

MP35N and Pt-Ir (80/20) wire electrodes were processed by single-run and repetitive RF plasma texturing and compared against control electrodes. The increased surface area resultant from the formation of nanowires significantly decreases surface impedance and for low frequency signals (<1000 Hz) results in decreased overall electrode impedance (electrolyte characteristics dominate for high frequency signals[48]). Signals below 100 Hz exhibited the most significant decrease, with the impedance of nanopillar-textured samples measuring on average at 20% that of the original unprocessed electrodes. Decreased impedance has been demonstrated for both MP35N and Pt-Ir (80/20) electrodes in Dulbecco's phosphate-buffered saline solution electrolyte as shown in figure 4.4. Also shown for the MP35N samples is that continued repetitive processing further decreases impedance in the low frequency range as structure depth and surface area increase. All measurements were made utilizing an Ag/AgCl reference electrode and a Pt counter electrode (25 cm^2).

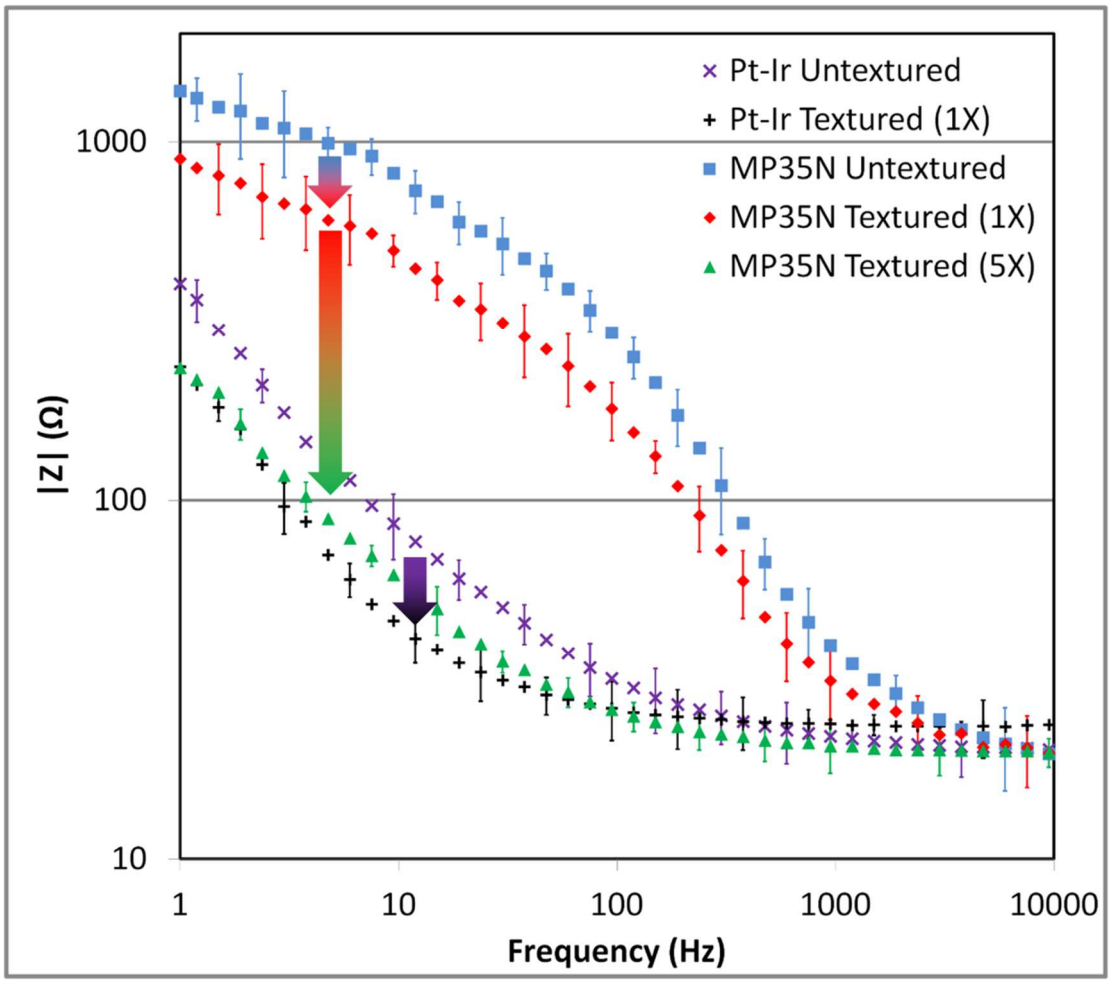

Figure 4.4. Impedance of Pt-Ir and MP35N electrodes with and without RF plasma processing to increase surface area. Significant impedance decreases occur in the lower frequency range (<1000 Hz) and both Pt-Ir & MP35N exhibit an approximate 50% decrease with one round of surface texturing. MP35N processed five times shows an order of magnitude decrease in impedance. Error bars indicate first standard deviation of data and are applied sparsely to maintain clarity.

In the low frequency range where the electrode-electrolyte surface characteristics dominate, the increased surface area significantly depresses impedance. For higher frequencies, the movement of ions within the electrolyte dominate and thus increasing surface area doesn't have as significant an effect[48]. Still, for many implantable biomedical electrode applications such as pacemakers, neural electrodes,

cochlear implants, etc. often the lower frequency range is employed (though perhaps not exclusively) and decreased surface impedance could provide advantages for battery life, measurement resolution, or noise reduction.

As expected, increased surface area increases double-layer capacitance resulting in a drop in surface impedance for the low frequency range. Observationally, the maximum magnitude of drop is inversely proportional to the increase in surface area from RF plasma texturing.

4.4 Decreased Impedance from Texturing of Foil Electrodes

Having established that RF plasma texturing can suppress surface impedance in wire electrode geometries, foil electrodes were prepared for similar testing. Again, surface impedance measurements were taken using a typical three-electrode electrochemical cell as in figure 4.3 with a platinum counter electrode (4 cm^2 surface area), an Hg-free Ag/AgCl single junction high temperature reference electrode (Fisher Scientific accumet Glass Body), and 316L stainless steel working electrodes (2 cm^2 surface area) separated by 2 cm in PBS solution. Measurements were taken over the 5 Hz - 1 MHz frequency range and five identical samples of each type were produced and multiple measurements conducted on each sample to promote statistical significance.

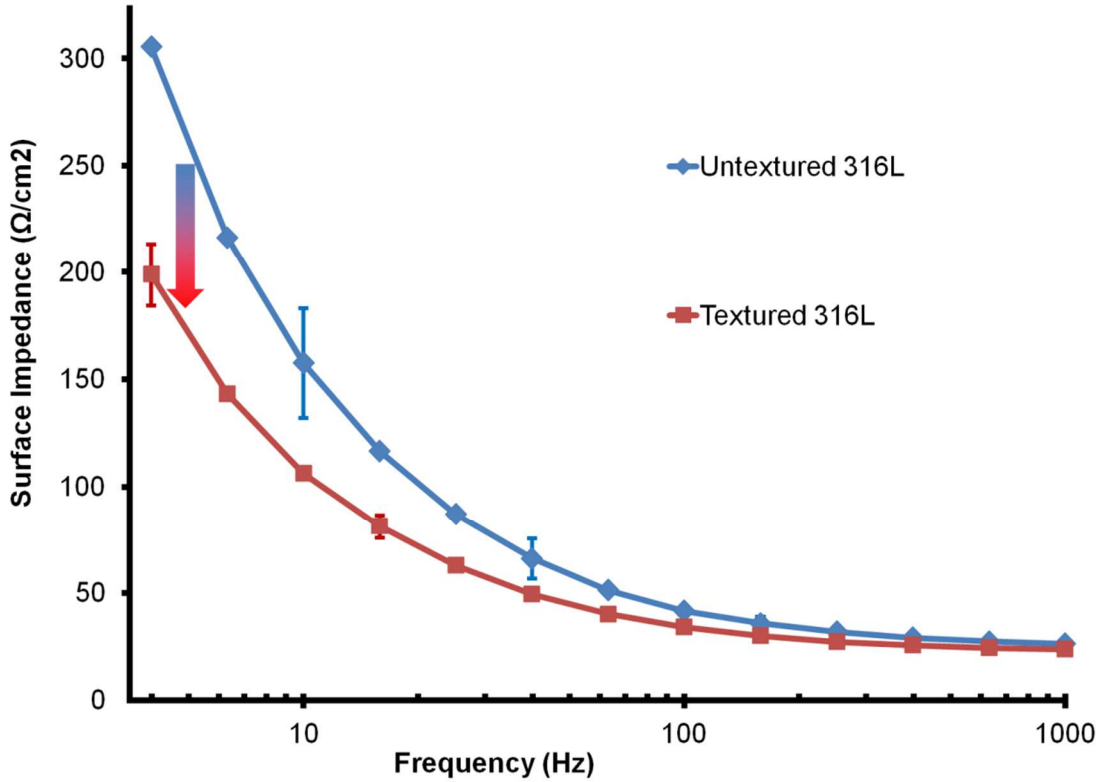

Figure 4.5. Surface impedance measurements with error bars representing the 95% confidence interval for RF plasma textured 316L stainless steel.

As presented in figure 4.5, RF plasma texturing of 316L stainless steel decreased the surface impedance particularly in the lower frequency range as electrolyte properties dominate in the upper frequency range. The increased surface area of the nanotextured 316L electrodes resulted approximately in a 33% decrease in surface impedance. Samples were textured by suspending 1.5 cm foil ribbons between 1 mm diameter Ni-Cr pillars electrically connected to the cathode base plate and separated by 10 cm. Samples were processed for 30 minutes at 250 watts in argon plasma with a chamber pressure of 25 millitorr. Texturing was primarily confined to the central strip of each ribbon sample. Untextured edges were removed and samples sectioned for impedance measurements.

4.5 Electrode Impedance Increase from Antifouling Coating

The next chapter will discuss in greater detail an antibiofouling electrode design in which textured electrodes are partially coated with polytetrafluoroethylene (PTFE); the aim being to prevent cell adhesion while retaining conductivity for neural recording or stimulation. For 316L samples prepared as in the previous section, the subsequent oblique incidence sputter deposition of PTFE re-increased the surface impedance to comparable levels as an untextured surface. Figure 4.6 shows how the fabricated antibiofouling 316L electrodes retain conductivity similar to simple untextured 316L electrodes.

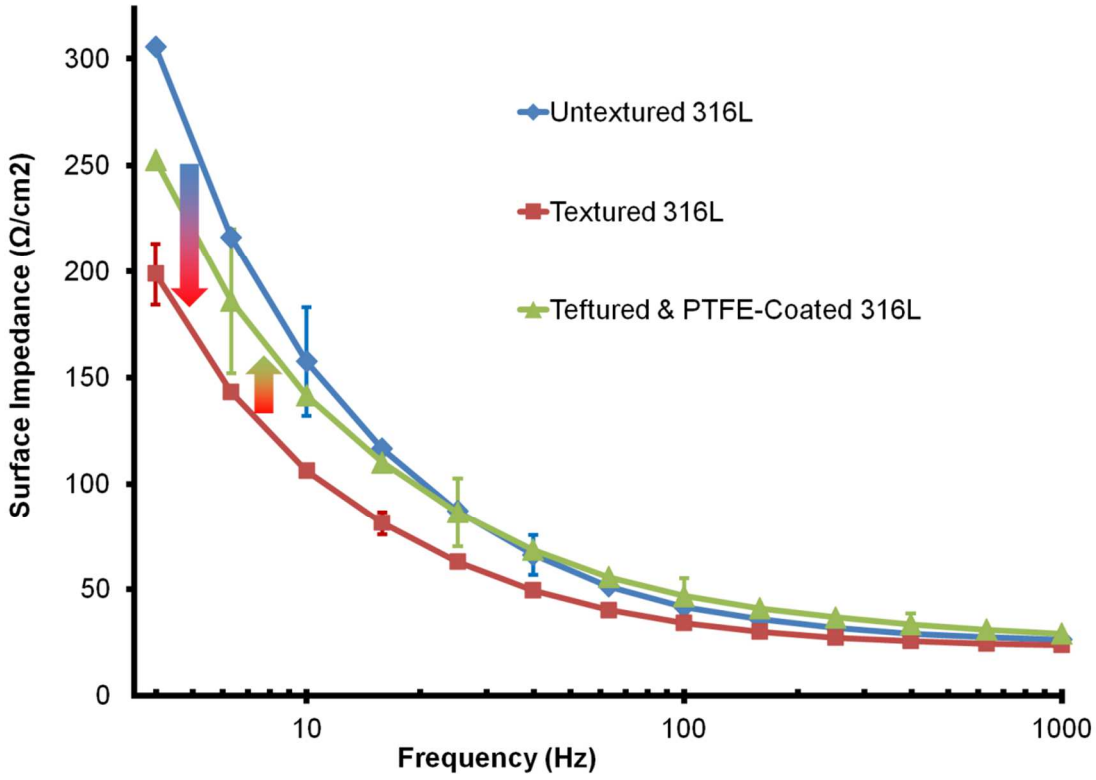

Figure 4.6. Surface impedance measurements in the lower frequency range (<1000 Hz) for untextured, RF plasma textured, and RF plasma textured PTFE-coated 316L electrodes.

Antibiofouling Pt-Ir wire electrodes were prepared similarly by repetitive RF plasma processing to produce surface texture followed by oblique incidence sputtering with PTFE. Samples were textured in argon plasma five times at 200 watts and 20 millitorr for 15 minutes per run. Surface impedance was measured as before in a typical three-electrode electrochemical cell with a 25 cm^2 Pt counter-electrode and an Hg-free Ag/AgCl single junction high temperature reference electrode (Fisher Scientific accumet Glass Body) with electrode separation held constant. Dulbecco's Phosphate-Buffered Saline (PBS) electrolyte simulated physiological conditions with 1M concentration. Figure 4.7 shows the expected decrease in surface impedance following texturing with the greatest effect in the lower frequency range.

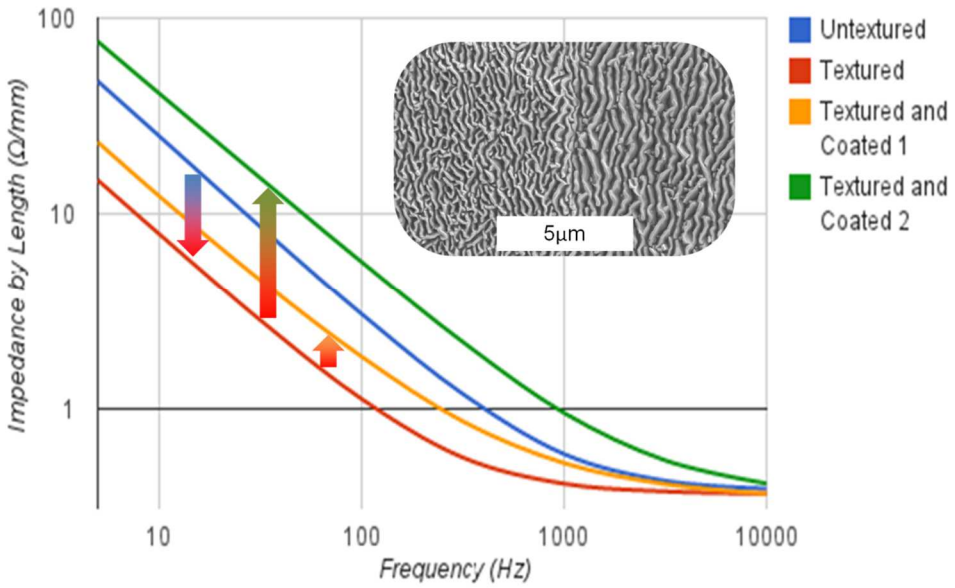

Figure 4.7. Antibiofouling Pt-Ir (80/20) electrode impedance comparison showing impedance decrease in the lower frequency range following texturing and then increase following PTFE deposition. Inset micrograph shows Pt-Ir textured surface structure.

Oblique incidence sputter deposition of PTFE onto textured Pt-Ir (80/20) re-increased surface impedance to levels comparable to plain platinum-iridium

electrodes. However, results were not consistent across sample groups with the first group's impedance not increasing enough and the second group's increasing too much. Inconsistent impedance increase across processing runs is an ongoing difficulty for wire geometries with PTFE sputtering having unpredictable effects on the conductivity. The trouble may have something to do with sample orientation when mounted in the sputtering chamber. For the antibiofouling foil 316L electrodes which are coated as a flat surface, impedance results were consistent. Conversely, for wire electrodes which are mounted vertically for texturing impedance measurements have varied widely. The structure of antibiofouling electrodes will be discussed further in the following chapter.

This chapter, in part, is reproduced or adapted from material as it appears in Acta Biomaterialia, "Controlled Metallic Nanopillars for Low Impedance Biomedical Electrode" Volume 10, Issue 5, Pages 2296-2303 (May 2014). Jonathan Trisnadi, Tae Kyoung Kim, Karla Brammer, Lina Reiss, Li-han Chen, and Sungho Jin are co-authors. The dissertation author was the primary investigator and author of this paper.

This chapter is also, in part, an adaptation of material being prepared for publication as "Antibiofouling Neural Electrodes by RF-Plasma Nanotexturing and Selective Hydrophobic Coating" with intended submission to Acta Biomaterialia. Laura Connelly, Chulmin Choi, Sungho Jin, and Renkun Chen are co-authors. The dissertation author is primary investigator and author of this material.

Chapter 5: Antibiofouling Electrodes

Antibiofouling electrodes were produced from 316L stainless steel by repetitive texturing with RF plasma followed by oblique incidence PTFE sputter deposition to selectively coat the upper portion of the textured surface. Surface impedance measurements confirmed good conductivity of the resultant electrode structure. Cell culture indicated a significant antifouling effect from the prepared electrodes including an 8-fold decrease in cell coverage. Nanotexturing followed by selective antifouling coating is presented as a feasible approach to manufacture of an antibiofouling neural electrode.

5.1 Antibiofouling Structure

As shown in figure 5.1, electrodes were fabricated from 316L stainless steel foil 0.1 mm thick. For texturing, foil was sectioned into 10 x 2 cm ribbons and processed under the following conditions: The ribbons were suspended by mechanical fixation between two NiCr wires (1 mm diameter, 10 mm length) connected to the chamber's cathode base plate. RF plasma texturing was performed with argon gas at a base operating pressure of 25 millitorr and samples subjected to 250 watts power for 30 minutes repeated five times to deepen structure[10]. Ribbons were allowed to cool completely between repetitions but were not exposed to oxidizing agents. Samples were taken from the center 1 cm of the ribbons to avoid the edge-effected regions near the sides. Following texturing, samples were sputter-coated with PTFE at an oblique angle of incidence such that deposition concentrated near the tips of the nanotextured features while the lower portions remain uncoated and highly conductive.

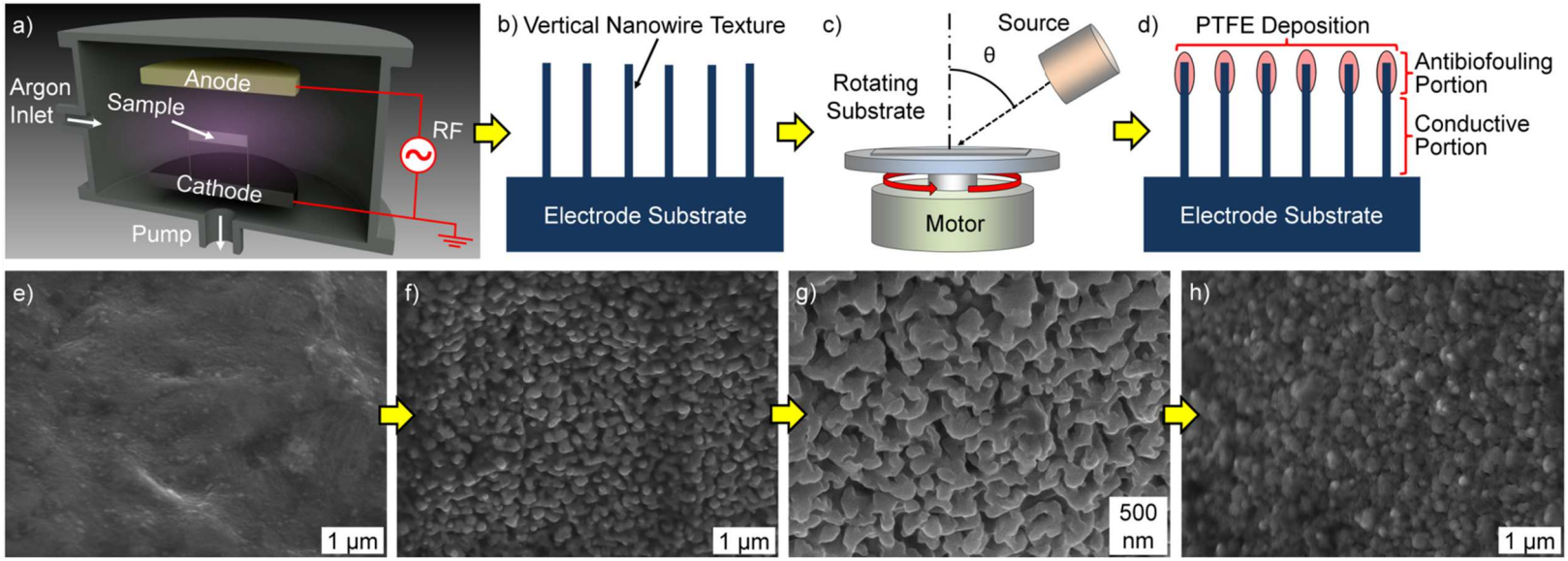

Figure 5.1. The electrode production process consisted of (a) repetitively texturing 316L stainless steel ribbons in RF plasma to (b) form metallic vertical nanostructures on the ribbon surface and (c) PTFE sputter deposition at an oblique angle to form (d) electrodes with a conductive portion underlying a hydrophobic antibiofouling layer. SEM micrographs are presented of the (e) untextured 316L surface, (f) 316L surface following one cycle in RF-plasma, (g) structure deepening by multiple repetitions, and (h) a textured and PTFE-coated surface.

5.2 Human Cell Culture on Antibiofouling Electrodes

Human aortic endothelial cells (HAOEC passage 2) (Cell Applications, Inc. San Diego, CA) were used for cell culture on the prepared 316L stainless steel antibiofouling electrodes. 1 mL ampoule of cells was mixed with 10 mL of alpha minimum essential medium with 10% fetal bovine serum and 1% penicillin-streptomycin. Cells were cultured at 37 °C and 5% CO_2 environment. Cells were seeded onto the substrates of interest (textured 316L, textured & PTFE-coated 316L, and untextured 316L) at a concentration of ~2 x 10^4 cells/mL. The substrates were placed on a 12-well polystyrene plate and medium changed after 24 hours and subsequently every 48 hours through the completion of the study.

5.3 Immunofluorescence of Cells Cultured on Antibiofouling Electrodes

At the specified time points cells were fixed to their respective substrates by 4% paraformaldehyde for 20 minutes at room temperature, then washed twice with wash buffer (1X PBS, 0.05% Tween-20). Cells were permeabilized with 0.1% Triton X-100 in 1X PBS solution for 10 minutes and again rinsed twice with wash buffer. TRITC-conjugated phalloidin (1:1000 Chemicom International) in 1X PBS was added and incubated for 1 hour at room temperature. Cells were once again washed in three rounds with 1X wash buffer for 5 minutes. Samples were inverted onto glass slides with fluomount-G (Southern Biotech), and visualized and captured using a red filter on a fluorescent inverted microscope. (DM IRB, Leica Co., USA).

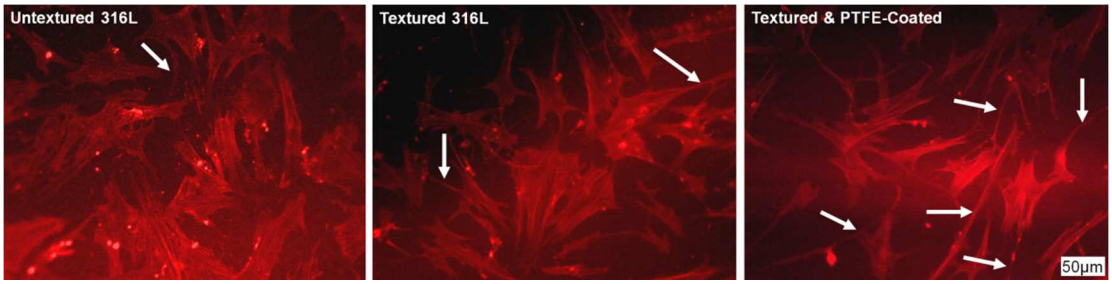

Figure 5.2. Immunofluorescent images of cytoskeletal actin (red) for HAOECs on untextured, textured, and PTFE-coated 316L surfaces after 8 days of culture incubation. Arrows indicate elongated filopodia.

After 8 days of incubation, immunofluorescent images of cytoskeletal actin shows the least cell spreading on the textured PTFE-coated samples compared to the textured and untextured samples in figure 5.2. The actin stain clearly shows long spindle like extensions (white arrows) from the cells on the textured surface and more so on the textured and coated surfaces compared to the wider spread cells imaged on the untextured 316L. These wide spread cells show many shorter filopodia on all the edges of individual cells.

5.4 FDA Assay of Cells Cultured on Antibiofouling Electrodes

Fluorescein diacetate (FDA) was used to visualize cell viability. At each time point samples were rinsed with PBS and incubated for ~30 seconds with FDA stock solution (5 mg dissolved in 1 mL acetone) in PBS (10 µL/10 mL). Samples were imaged by inverting opaque samples in a clean well with a droplet of PBS and captured using a green filter on a fluorescent inverted microscope. (DM IRB, Leica Co., USA).

Cell viability was evaluated by an FDA staining assay as shown in figure 5.3 to compare a polystyrene plate optimized for cell culture to the three experimental

electrode substrates. Similar to the actin stain, the FDA images show an obvious antibiofouling effect in the textured and the textured PTFE-coated substrates. Figure 5.3 shows representative fluorescent images from Day 10 of incubation. The textured PTFE-coated substrate shows the least cell spreading and the fewest number of viable cells in all images and time points during the assay. Several long thin filopodia extensions were observed in the textured PTFE-coated images, in agreement with the conformations observed in the cytoskeletal actin.

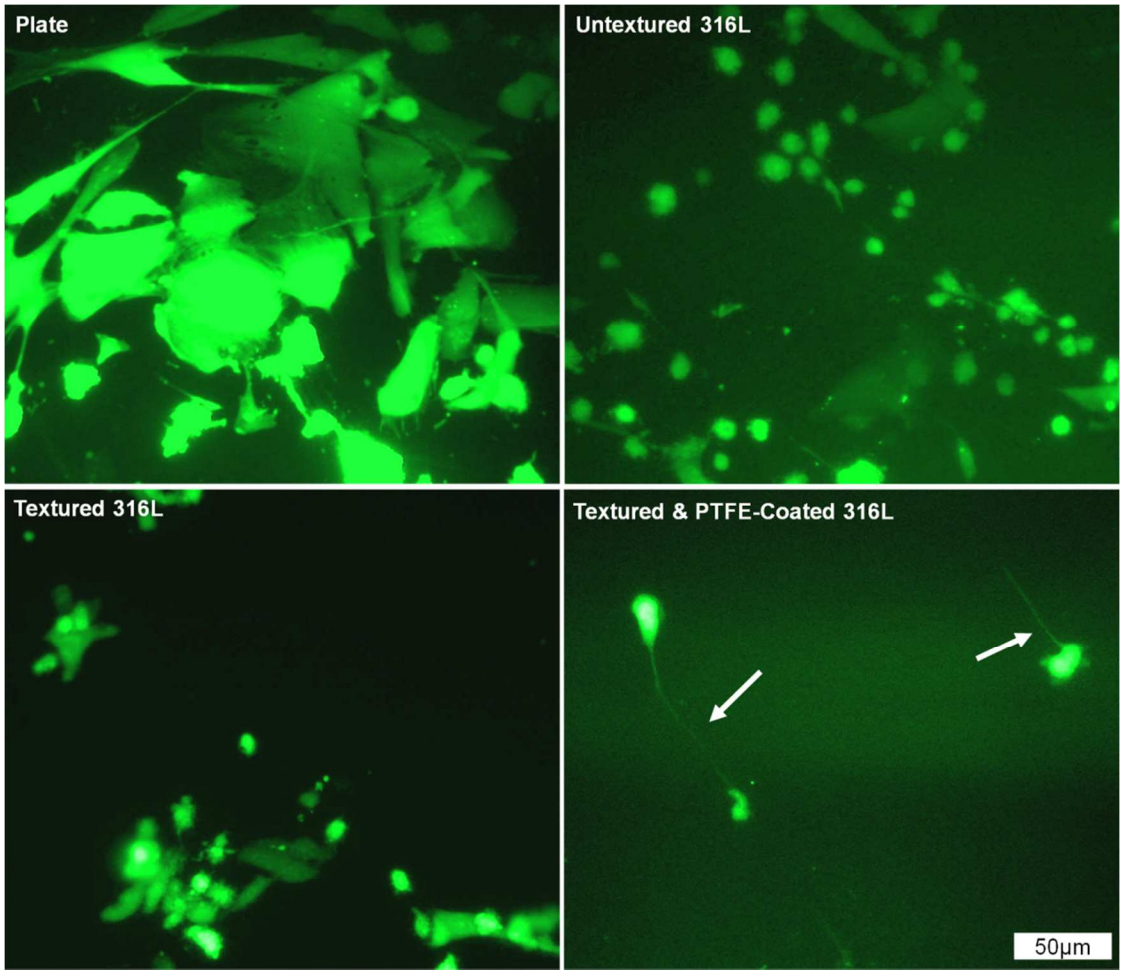

Figure 5.3. FDA (green) viability of HAOECs on polystyrene culture dish, untextured, textured, and PTFE-coated 316L surfaces after 10 days of culture incubation. Arrows indicate filopodia extensions.

5.5 MTT Assay of Cells Cultured on Antibiofouling Electrodes

For each time point, samples were rinsed with phosphate buffered solution and transferred to new 12-well dishes of polystyrene. Then, 1 mL of media and 0.1 mL of MTT reagent was added to each well and incubated for 2 hours in a 37 °C and 5% CO_2 environment. Finally, 1 mL of solubilizing solution was added to each well to dissolve the crystals at the completion of the incubation period. Absorbance of the solutions was measured at 570 nm, subtracting out background at 690 nm. Control samples were untextured 316L and plain wells in the 12 well culture dish of polystyrene.

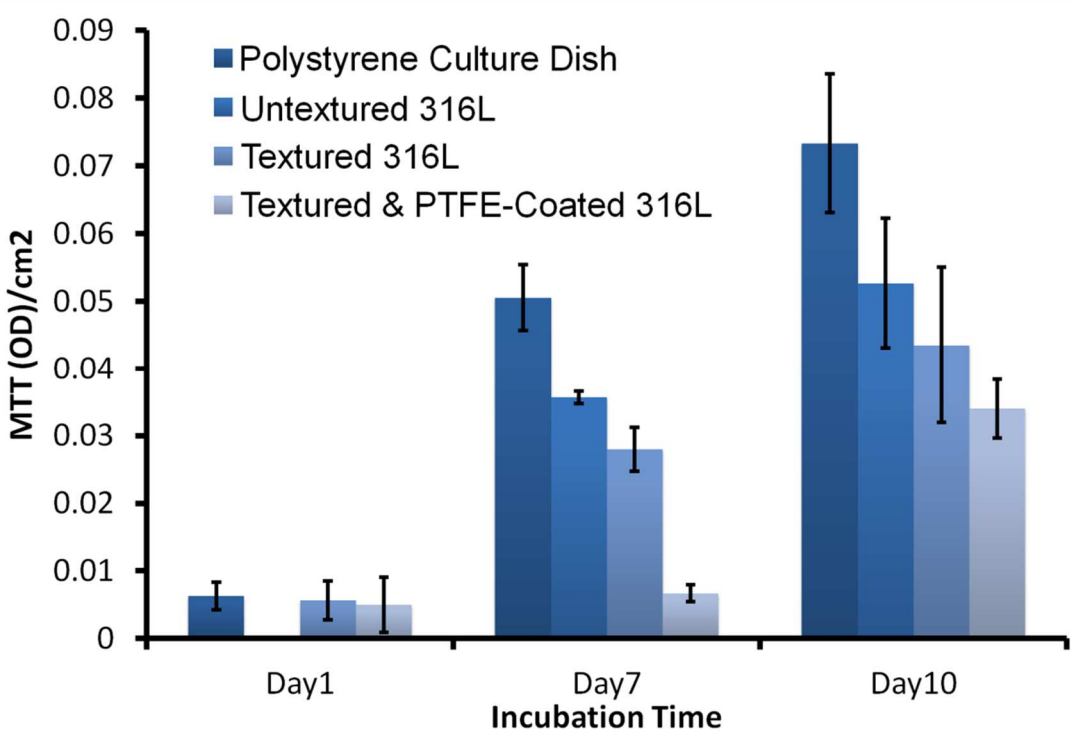

Figure 5.4. MTT assay data showing the optical density (OD) of the reaction product of the MTT working solution of HAOECs on polystyrene culture dish, untextured, textured, and PTFE-coated 316L surfaces at 1, 7, and 10 days of culture incubation. Error bars show average standard error.

Cell viability was also evaluated by an MTT assay shown in figure 5.4 with time points at 1, 7, and 10 days. This assessment also indicates that the smallest density of viable cells occurred on the textured PTFE-coated samples. Consistent with the immunofluorescent images and the FDA assay, at each time point the textured and PTFE-coated samples exhibited the most biofouling surfaces with a particularly favorable result on day 7. The textured surface alone also showed a biofouling effect in comparison to the untextured and culture dish measurements. The untextured surface, at the first time point of day 1 is reported as zero. This may be due to day 1 values below the optical density limit of the spectrophotometer.

5.6 Cell Coverage on Antibiofouling Electrodes

Cell spreading was quantified using ImageJ software and selection of 3 representative FDA fluorescence images. The area of fluorescent cells was calculated by color thresholding and presented as a percentage of the entire imaged area. To quantify coverage by viable cells, the percentage of cell coverage for each experimental surface was calculated from the average of 3 representative FDA fluorescent images as shown in figure 5.5. The textured PTFE-coated textured surface shows 0.97% +/-0.54 coverage compared to the untextured control sample at 7.86% +/-1.60 for an 8-fold decrease in coverage. The cell coverage decrease due to the PTFE coating is 7-fold from the plain textured sample.

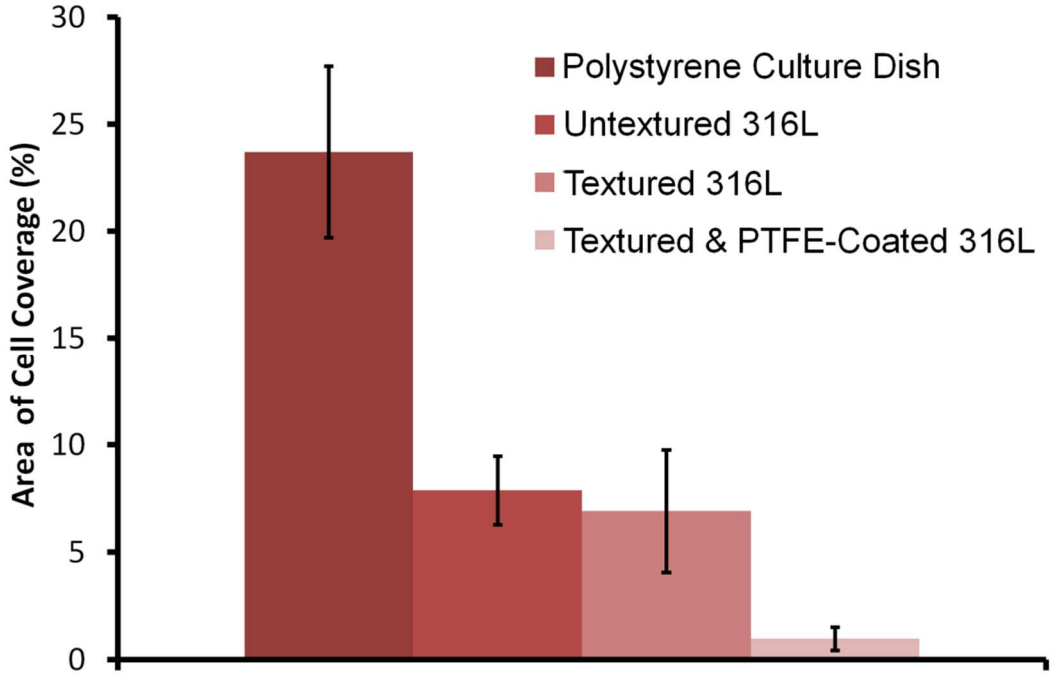

Figure 5.5. Cell Coverage analysis of HAOEC spreading on the polystyrene culture dish, untextured, textured, and PTFE-coated 316L surfaces after 10 days of culture. Error bars show the average standard error.

5.7 Differences Between BAEC and HAEC Results

Earlier work by Loya et al., and result reported as a portion of this work in section 3.7 explored endothelial cell response to surface texturing for non-textured and textured MP35N seeded with bovine aortic endothelial cells (BAEC) for cell culture and analysis[6,10,9]. In the earlier work, RF plasma texturing provided for enhanced endothelialization, particularly the formation of a smooth single layer of cells with excellent organization. Now however, for cells cultured on RF plasma textured 316L stainless steel samples cell viability, coverage, and organization is notably suppressed even without a PTFE antifouling coating. The difference in result is likely due to the differences in cell type (BAEC vs. HAEC), substrate material (MP35N vs. 316L

stainless steel, and surface structure as depicted in figure 5.6. Whereas the MP35N surface is textured with regular similar sized nanowires with blunt upper tips, the 316L surface is irregular with a substantially more jagged morphology. It is possible that the difference in results between BAEC culture and HAEC culture is attributable to the disparity in surface regularity. Otherwise, inconsistent materials (both cells and substrates) is the most probable cause.

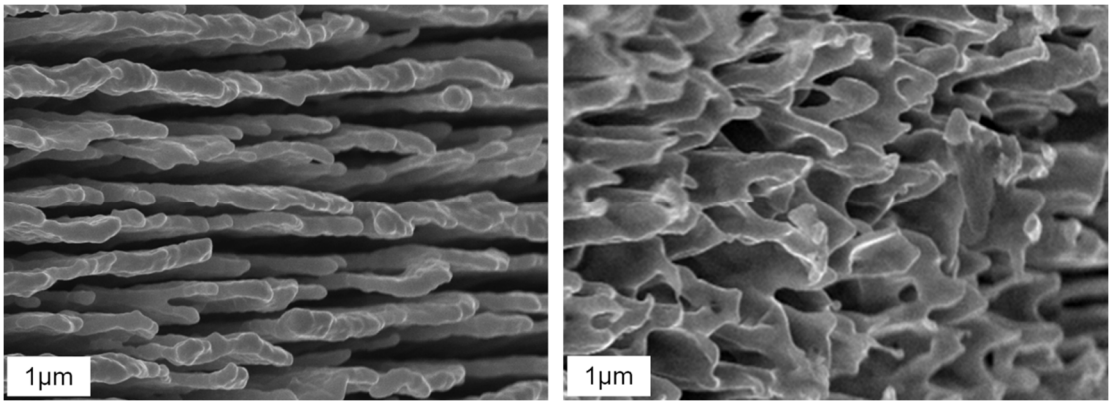

Figure 5.6. Comparison of RF plasma textured MP35N (Left) and RF plasma textured 316L stainless steel (Right). Both samples were textured for five repetitions.

5.8 Discussion of Antibiofouling Electrode Results

Implantable neural electrodes must not only electrically function but also remain biocompatible without causing cytotoxicity. In this work, the goal was to create an antibiofouling surface which retains the electrical integrity of the electrode. Both 316L stainless steel[124,125] and PTFE[126] have previously been utilized in specific biological implants. Textured 316L coated with PTFE expresses an enhanced antibiofouling compared to the uncoated samples in all cell culture assays observed.

The fewer but much longer extensions on the textured surfaces, observed in the actin stain in figure 5.2, suggest that the cell's local environment is unfavorable and

therefore the cell extends filopodia over long distances in search for points of stronger focal adhesion. These unfavorable surfaces, likely caused by both the nanotexturing and hydrophobic PTFE coating may sufficiently limit cellular adhesion to create a significant antibiofouling effect.

In the FDA staining assay of figure 5.3 and MTT assay of figure 5.4 which were used to evaluate cell viability, the textured and PTFE-coated 316L stainless steel substrate was compared against untextured 316L stainless steel, textured but uncoated 316L stainless steel, and polystyrene plates optimized for cell culture. Each assay shows an obvious antibiofouling effect in both the textured and textured PTFE-coated substrates indicating that the texture alone produces a notable decrease in cell viability. The addition of the PTFE coating only enhances this property as the textured and coated samples exhibit fewer viable cells of any substrate tested.

An antibiofouling surface is one that limits the overall cell coverage, allowing electrical signals to be transmitted and received. It is apparent that wider spread cells may cover more surface area than balled up and condensed cells. Therefore, a perhaps better measure of antibiofouling properties is overall cellular coverage rather than total number of viable cells. The percentage of cell coverage for each experimental surface was presented in figure 5.6 with the textured PTFE-coated surface demonstrating a significant 8-fold decrease in coverage when compared against the untextured uncoated 316L samples. The importance of the PTFE coating is made abundantly clear as well: there is a 7-fold decrease in cell coverage on the coated samples compared against the uncoated but textured group.

By reducing cell coverage on the electrode surface while maintaining electrical conductivity, it will be possible to produce longer lasting implantable electrodes. Still there remains much work to do. Extensions of this research must include a variety of cell types, electrode geometries, electrode materials, longer time-scales, and potential drug delivery performance[70,127–131]. And of course, experiments must move beyond in vitro testing to true in vivo impedance results for specified applications such as cochlear implants, pacemaker electrodes, or other chronic electrode implants for neural recording or stimulation. Potential issues may arise from PTFE delamination, geometric and shielding challenges in the RF plasma texturing process, and/or difficulties with oblique incidence sputtering for more complex electrode form factors.

This chapter, in full, is adapted from material being prepared for publication as "Antibiofouling Neural Electrodes by RF-Plasma Nanotexturing and Selective Hydrophobic Coating" with intended submission to Acta Biomaterialia. Laura Connelly, Chulmin Choi, Sungho Jin, and Renkun Chen are co-authors. The dissertation author is primary investigator and author of this material.

Chapter 6: Controlled Drug Release from Textured and Deformed MP35N

In combination with mechanical strength, high ductility has been observed in the surface nanopillars which result from RF plasma texturing. Unlike many non-metallic nanostructures, the pillars may be plastically deformed without fracture. As result, it is possible to store drugs (antifouling or anti-inflammatory drugs for instance) within the surface crevices and to deform the pillars to secure the drugs for restricted long-term release.

6.1 Materials

Drug-eluting surfaces are highly important to successful biomedical implants. Many devices utilize or could utilize drug elution such as prosthetics, wound dressings, bone implants, dental implants, pacemakers, cochlear implants, or chronic electrode implants among others[132,133]. But by far the most important controlled release in current clinical use is drug-eluting coronary stents[93,94]. Drug-eluting stents (DES) with current clinical approval release anti-restenosis drugs paclitaxel, sirolimus, or a sirolimus derivative (zotarolimus or everolimus). Stents are constructed from 316L stainless steel, Pt-Cr, L605, Nitinol, or MP35N as in Table 1.3. For this work, sirolimus and paclitaxel on an MP35N bare metal stent (BMS) were selected.

6.1.1 Sirolimus

Sirolimus, a macrocylic lactone with anti-inflammatory and anti-proliferative properties has been shown to reduce the risk of restenosis following the placement of coronary stents [80,83,134–136]. Also known as rapamycin, sirolimus ($C_{51}H_{79}NO_{13}$) was

obtained from ChemieTek with 99+% purity and used without further purification. Before use, the material was stored desiccated at 5 °C in a non-transparent container. UV/VIS spectrometry maxima for ethanolic solution is at the 277 nm wavelength and was measured accordingly.

6.1.2 Paclitaxel

Similarly, anti-microtubule paclitaxel has been used in stents to suppress neointima growth and restenosis formation [73,78,79,135–138]. Paclitaxel ($C_{47}H_{51}NO_{14}$) was obtained from Acros Organics with 99+% purity and used without further purification. Before use, the material was stored desiccated at 5 °C in a non-transparent container. UV/VIS spectrometry maxima for ethanolic solution is at the 229 nm wavelength and was measured accordingly.

6.1.3 MP35N

MP35N biomedical alloy composed of 35% Co, 35% Ni, 20% Cr and 10% Mo was selected as BMS platform due to its history as a coronary stent material as well as its susceptibility to nanotexturing by RF plasma[103,105,139]. MP35N wire samples have a multi-phase structure containing close-packed (HCP) and face-centered cubic (FCC) phases[117]. The RF plasma technique used to nanotexture the stent surface results in a loss of material by etching, which is not necessarily a uniform process. It may be that the presence of separate phases in the MP35N is important to the formation of nanowire/nanopillar geometry by RF processing, as the different phases exhibit

substantially different sputter etch rates. The sample alloy wires prior to processing were 250 μm in diameter with an electropolished smooth surface.

6.2 RF Plasma Texturing of MP35N Stent Struts

All sample texturing was performed using a custom-built RF plasma system (13.56 MHz) configured as depicted in section 1.1 of this work. In preparation, ten MP35N alloy wires, each 250 μm in diameter and approximately 10 cm long, were rolled to ~75 μm. Five were then placed vertically in the cathode plate base of the RF plasma system situated 2.5 cm apart from each other. Before processing, the chamber was evacuated to 10^{-5} Torr, then 30 sccm of Ar gas flow initiated, and pressure increased to 20 millitorr by partially closing the high vacuum valve. Argon gas was selected as having shown the most substantial texturing properties in prior reported experiments[10]. Upon equilibrium, the rolled wires were subjected to between 175 watts power for 18 minutes repeated five times with wires cooled between repetitions. Repetition was employed to deepen the surface texture sufficiently for drug loading with maximum depth reaching ~6-8 μm with texture as shown in figure 6.1. Samples were not exposed to oxidizing agents between processing runs. It should also be noted that the etching process decreased the overall thickness of the processed samples to ~65 μm. The temperature rise of the MP35N wire samples was monitored using visual inspection and IR thermometer, and reached an estimated 800–1000 °C. The remaining five wires which were rolled but not textured were designated for experimental controls.

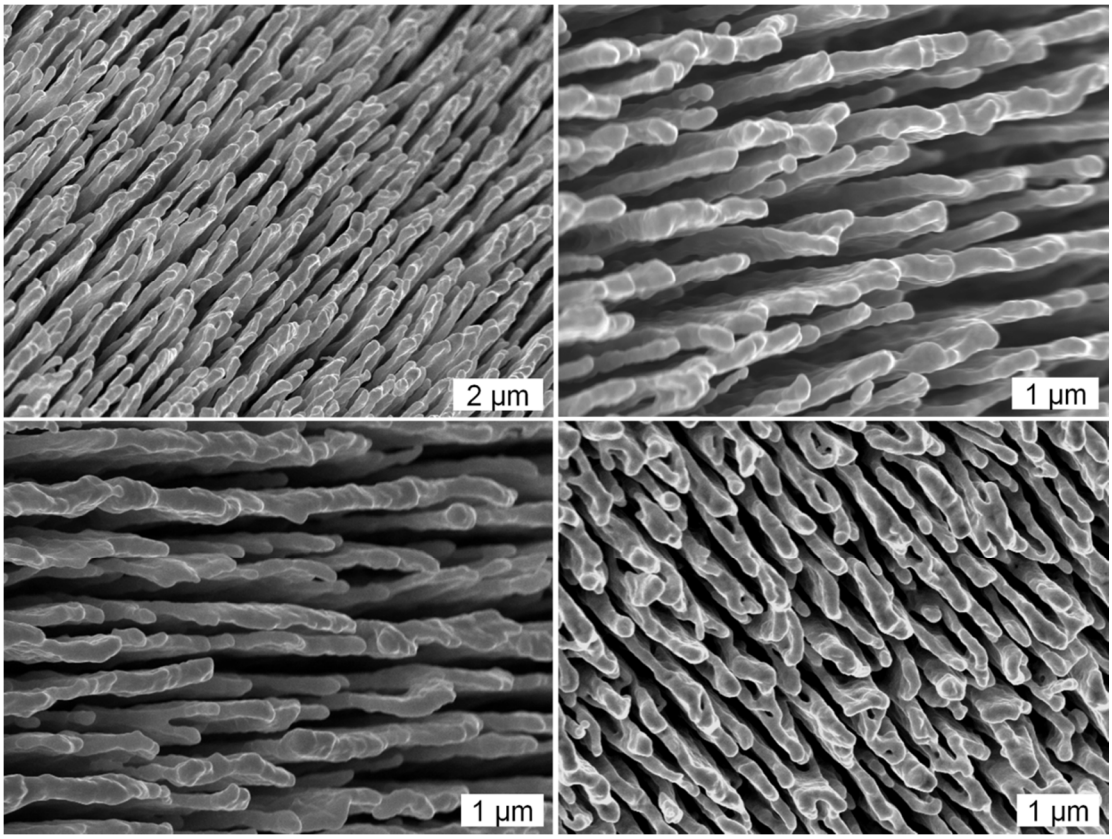

Figure 6.1. SEM micrographs at various magnification levels of textured MP35N surfaces following RF plasma processing repeated five times to deepen the structure.

6.3 Drug Loading Textured Stent Struts

Vacuum loading was necessary to ensure good penetration of drug solutions into the textured surface. Drug loading was accomplished by evacuating the five textured samples and half of the untextured samples to 10^{-2} Torr and immersing them in either a 1 mg/ml solution of sirolimus in ethanol or a 1 mg/ml solution of paclitaxel in ethanol. Samples were agitated overnight prior to removal and complete ethanol evaporation at 35 °C. Total drug loaded was to be determined by totaling release data. The remaining untextured and unloaded samples were maintained as an experimental control. Figure 6.2 presents an SEM micrograph of a textured and loaded sample.

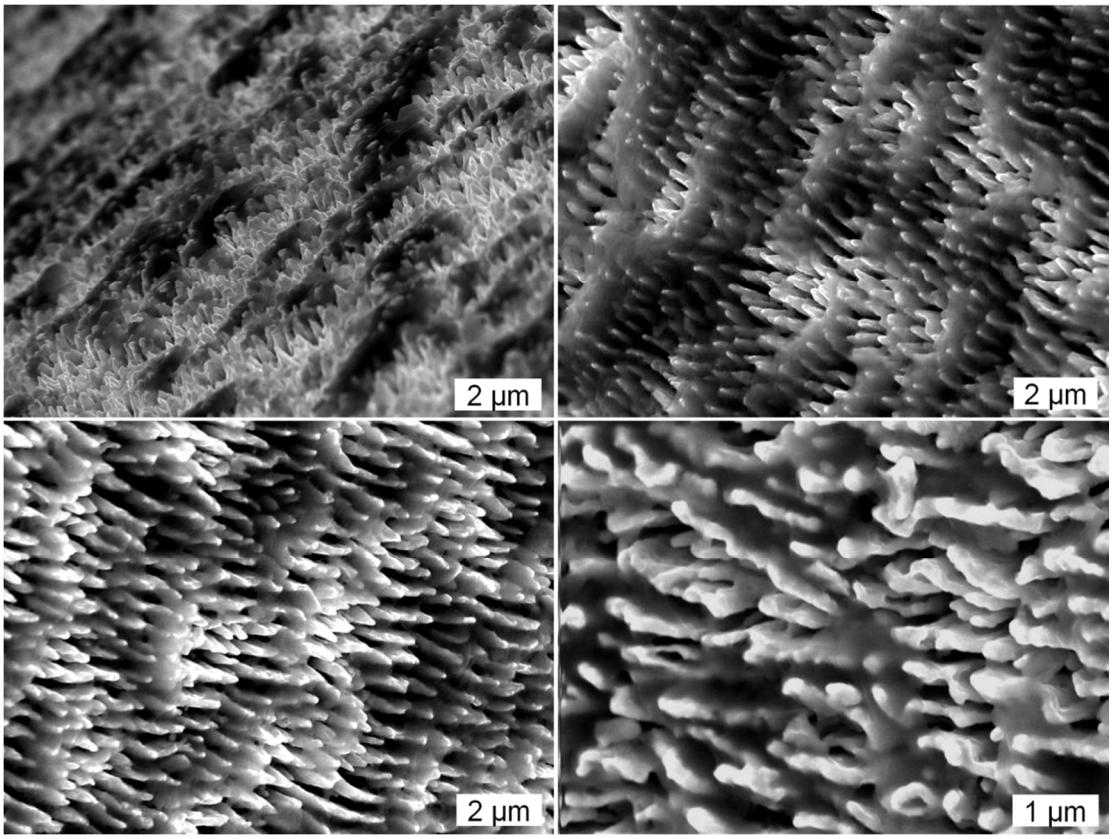

Figure 6.2. SEM micrographs at various magnification levels of RF plasma textured MP35N surfaces following sirolimus or paclitaxel loading in ethanolic solution under vacuum. Nanopillar tips remain visible as the medications fill the interspersing spaces.

6.4 Deformation to Confine Drugs within Stent Surface

To restrict drug diffusion from the textured and loaded surface, half each of the textured and loaded sirolimus samples and the textured and loaded paclitaxel samples were rolled to ~55 µm. Finally, samples were sectioned into 1 cm lengths resulting in five identical samples across seven sample types. The samples tested were as follows: textured and rolled MP35N loaded with paclitaxel; textured MP35N loaded with paclitaxel; untextured MP35N loaded with paclitaxel; textured and rolled MP35N loaded with sirolimus; textured MP35N loaded with sirolimus; untextured MP35N loaded with sirolimus; and untextured MP35N with no drug loaded to act a control.

Figure 6.3 presents SEM micrographs of samples which were textured, loaded, and rolled to restrict drug release.

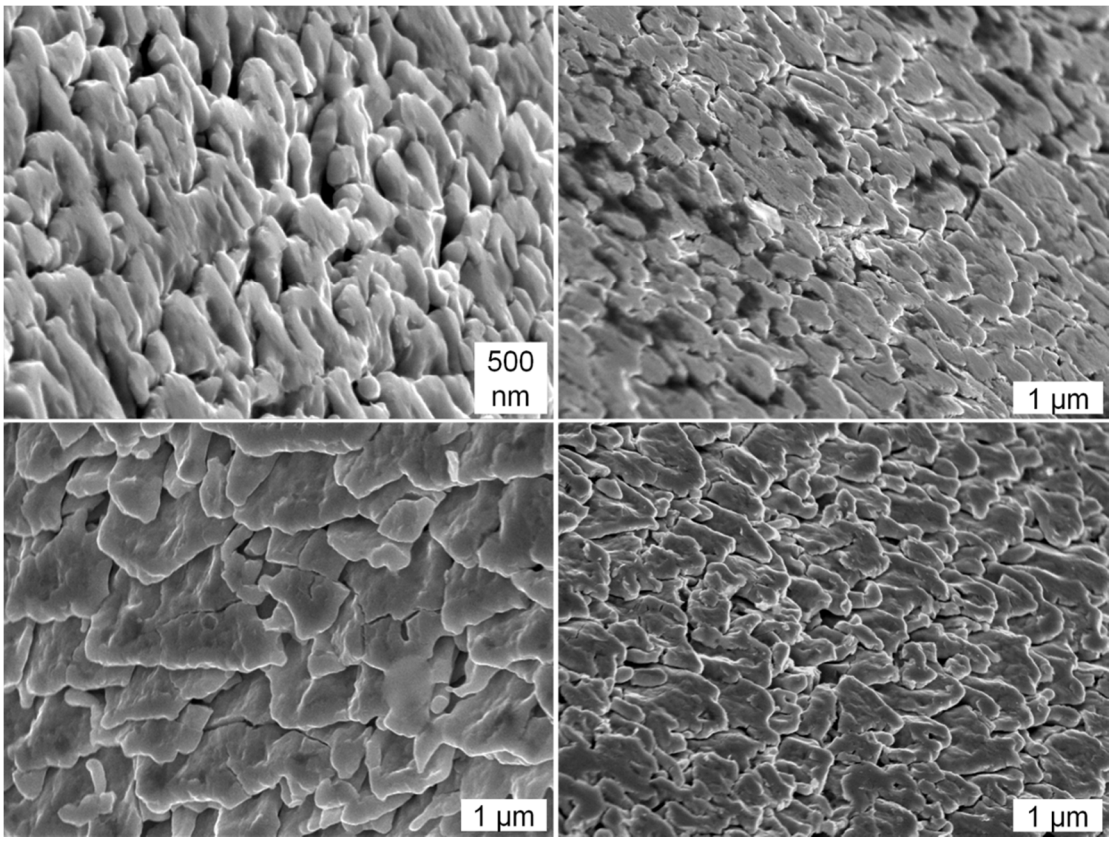

Figure 6.3. SEM micrographs at various magnification levels of MP35N surfaces which were textured by RF plasma, loaded with either sirolimus or paclitaxel, and then mechanically deformed by rolling.

6.5 Drug-Release Experiment Design

Prior to beginning the drug release trial, standard concentration curves for Paclitaxel and Sirolimus were obtained for the BioMate 3 UV/VIS spectrophotometer used throughout. All measurements were performed using a single-position cell holder with a blank measured prior to each test (Sirolimus at 277 nm, Paclitaxel at 229 nm). Standard curves were obtained, with triple redundancy, by determining absorbance at known drug concentrations in 1:1 solutions of ethanol and Dulbecco's Phosphate-

Buffered Saline (DPBS) which would be used to simulate a body environment during release testing. Measurements were performed using BRAND 759210 UV cuvettes. Concentration calibrations for both sirolimus and paclitaxel showed good linearity with R^2 values of 0.995 for paclitaxel and 0.990 for sirolimus.

The release experiment was designed on a 40-day timeline with measurements staggered according to expected release concentrations. The 35 samples were tested for drug release in a 0.5 mL of DPBS to simulate body fluid. All release was performed at 37 °C to mimic body temperature. For concentration testing, samples were immediately transferred to fresh, preheated (37 °C) simulated body solutions and returned to the incubator. Concentration measurements were taken by adding 0.5 mL ethanol to the release DPBS, mixing by vibration, measuring by BioMate 3 UV/VIS spectrophotometer, and comparing against the standard curve. Blank was set for every test to maintain consistency in measurement.

On day 1, the drug release concentration was tested every hour for the first three hours, then at the 6th hour, the 12th hour, and the 24th hour. The concentration was then measured on the 2nd, 3rd, 5th, 7th, 10th, 13th, 17th, 22nd, 29th, and 40th days of the trial. All 35 samples, five samples for each of the seven types, were measured each time with exception of the 7th, 13th, 17th, and 29th measurements. For those data points only the rolled samples were measured along with the unloaded control as the other sample types had all but ceased any drug release. Successive measurement points were selected based on evaluation of previous concentrations and,

in the early trials, the time limitations of measuring all samples successfully between time-points.

6.6 Drug-Release Experiment Results

Results were analyzed with MATLAB. Drug release data from different samples were evaluated by unpaired Student's *t*-test and one-way ANOVA analysis followed by Tukey's range test. Differences were considered statistically significant when $P \leq 0.05$. Upcoming sub-sections 6.6.2 through 6.6.4 will refer to figure 6.4 and figure 6.5. Sub-sections 6.6.5 through 6.6.7 will refer to figure 6.6 and figure 6.7.

6.6.1 Untextured and Unloaded Control Group

Five samples of 250 μm MP35N wire rolled to ~75 μm and sectioned to 1 cm lengths were used as an unloaded control group. Release concentration measurements were performed identically to drug-loaded samples. As expected, concentration measurements were consistently very near zero (averaging ~0.2 μg and always less than 0.5 μg) and substantially lower than the release from either sirolimus-loaded or paclitaxel-loaded samples. The slight nonzero measurements were attributed to impurities acquired during sample transfer and in the interim between concentration measurements. Results were highly consistent across the five samples with standard deviations averaging ~0.1 μg and always less than 0.25 μg. As the impurities acquired by the unloaded control samples would also be present in the loaded samples, it was possible to calibrate the loaded sample measurements using the control group as a baseline.

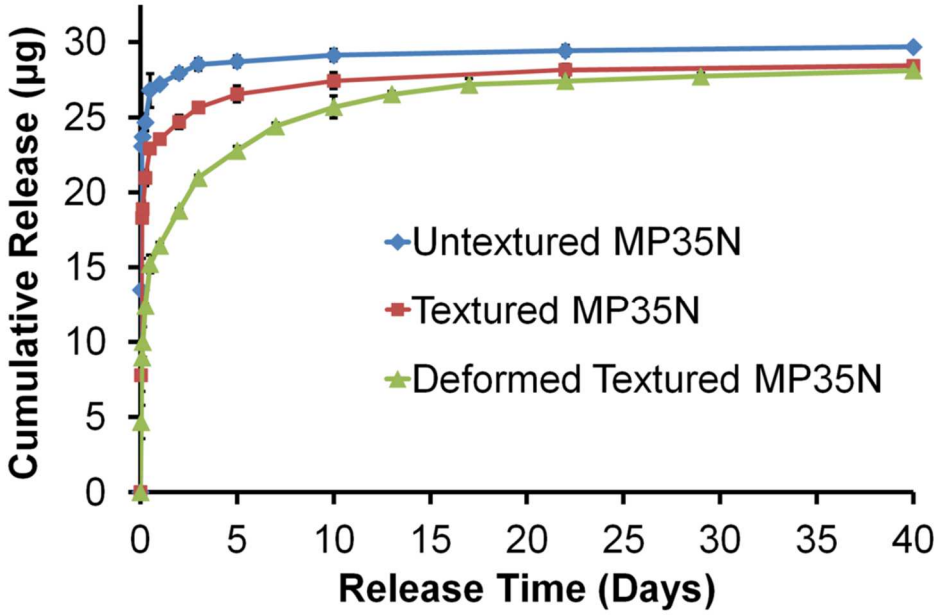

Figure 6.4. Paclitaxel cumulative release profiles in vitro from untextured, textured, and deformed textured MP35N samples demonstrating the extended release of the deformed set. Error bars indicate first standard deviation of data.

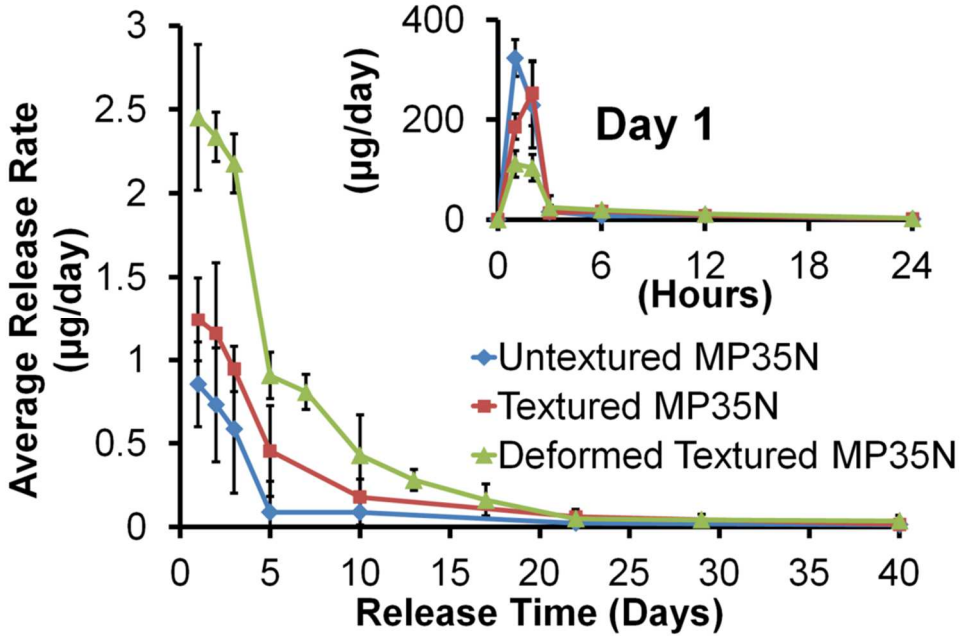

Figure 6.5. Paclitaxel release rates in vitro from untextured, textured, and deformed textured MP35N samples showing the elevated rate of release over time from the deformed group. The inset captures the burst phase of quick release upon sample insertion and illustrates the suppressing effect of the deformed surface.

6.6.2 Untextured and Paclitaxel-Loaded Group

A total of ~30 μg paclitaxel was released on average from each of five samples of 250 μm MP35N wire which was rolled to ~75 μm before loading with Paclitaxel. Figure 6.4 depicts the cumulative release profile with tight deviations across the five samples. Average surface load density was ~0.37 mg/cm^2. During an initial burst phase, over 75% of the drug was released in the first two hours, and in excess of 90% in the first day. The release rate peaked immediately at ~320 μg/day before quickly tapering off as shown in figure 6.5. Following the initial release of loaded drug from the surface, the other sample types surpassed the untextured samples release rate. Measurable release had all but ceased within five days. With little resistance to diffusion of the drug from the sample surface, the loaded paclitaxel was rapidly exhausted.

6.6.3 Textured and Paclitaxel-Loaded Group

For the five samples which were rolled to ~75 μm and nanotextured by RF plasma prior to loading with paclitaxel a slightly lower total of ~28 μg was released on average with an average surface load density of ~0.36 mg/cm^2. As shown in the cumulative release profiles of figure 6.4, the release from a textured surface was extended but still accomplished mostly within the first few days of the trial. Approximately 65% of the total release occurred within the first two hours, and over 80% by the end of the first day. Appreciable release continued until the tenth day of the trial. The release rate depicted in figure 6.5 peaked in the second hour at ~250 μg/day, before falling off for the remainder of measured time-points. The depth and

density of surface texture appears to have somewhat slowed diffusion but the burst phase still dominated release with only a small remainder of loaded paclitaxel escaping afterward.

6.6.4 Textured, Paclitaxel-Loaded, and Deformed Group

The group of MP35N samples which were flattened, textured by RF plasma, loaded with paclitaxel, and then rolled again to deform the surface released ~28 μg total on average from each sample over the course of the trial for a surface load density of ~0.35 mg/cm^2. As before, the majority of drug was released in the first day but the burst phase was significantly reduced with only 30% of total release occurring in the first two hours and less than 60% in the first day.

For the deformed samples, the cumulative release profile in figure 6.4 showed considerable continuous release for the first three weeks. Figure 6.5 depicts the suppressed burst phase release rate peaking in the first hour at ~110 μg/day and an extended elevated release rate which surpasses the untextured and textured samples on the first day and remains markedly superior over the next 20 days of the trial. The deformed surface seems to have delayed drug diffusion from the surface when compared to the other sample types though the release rate fell continuously after peaking at the first measurement.

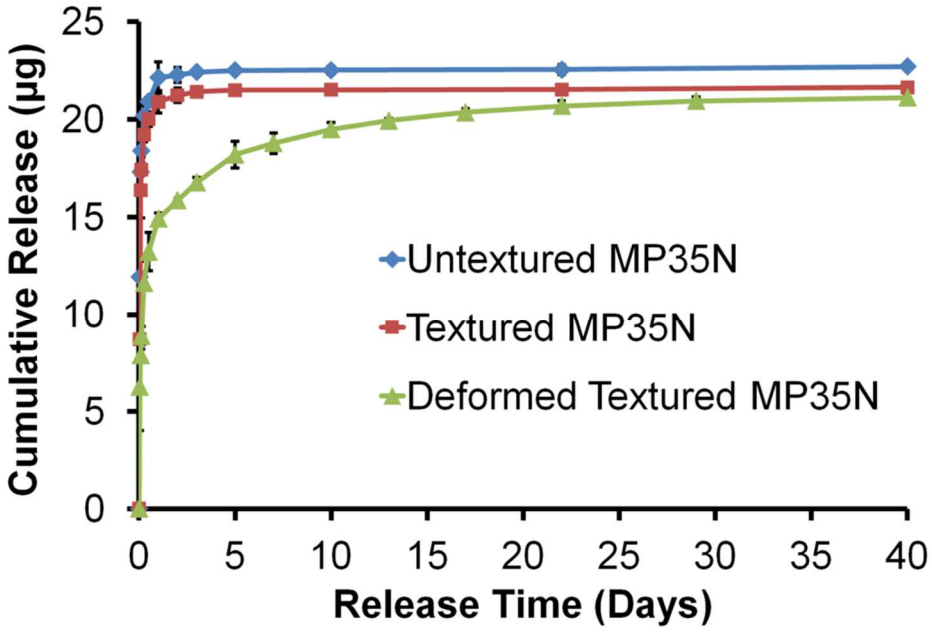

Figure 6.6. Sirolimus cumulative release profiles in vitro from untextured, textured, and deformed textured MP35N samples demonstrating the extended release of the deformed set. Error bars indicate first standard deviation of data.

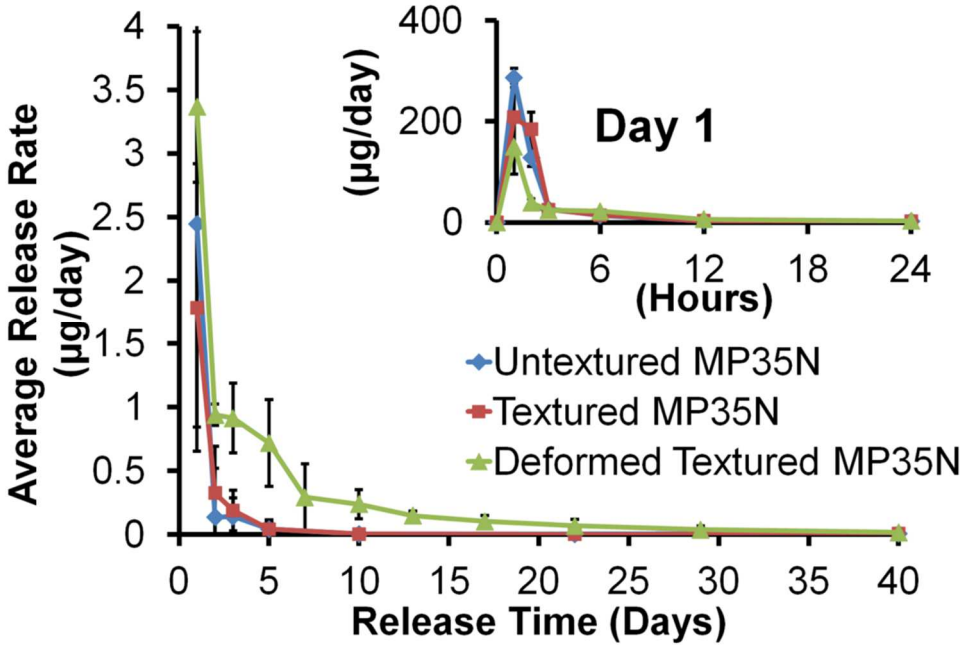

Figure 6.7. Sirolimus release rates in vitro from untextured, textured, and deformed textured MP35N samples showing the elevated rate of release over time from the deformed group. The inset captures the burst phase of quick release upon sample insertion and illustrates the suppressing effect of the deformed surface.

6.6.5 Untextured and Sirolimus-Loaded Group

The group of samples which were flattened and then loaded with sirolimus exhibited a total average release of ~23 μg for a load density of ~0.28 mg/cm^2. Figure 6.6 presents the cumulative release profile of sirolimus-loaded samples and shows that the untextured group released nearly all the drug immediately with ~75% occurring in the first two hours and over 97.5% in the first day. The release rate in figure 6.7 peaks in the first hour at nearly 290 μg/day before falling off immediately and disappearing completely after the 5th day. As with the untextured paclitaxel group, it seems that with little resistance to diffusion from the sample surface, the loaded sirolimus was rapidly exhausted.

6.6.6 Textured and Sirolimus-Loaded Group

The five samples which were flattened and then textured by RF plasma before sirolimus-loading showed a highly similar release profile to the untextured group. The average total release was just under 22 μg with a load density of ~0.27 mg/cm^2. The release profile in figure 6.6 closely follows the shape of the untextured group with ~75% occurring in the first two hours and over 95% in the first day. The release rates in figure 6.7 are also near identical though the textured group does not peak so highly during the burst phase, reaching only ~210 μg/day before falling off. As with the untextured group, release drops steeply and essentially disappears after the fifth day. In contrast with the textured and paclitaxel-loaded group, this group does not seem to exhibit any extended release attributable to the surface texturing alone.

6.6.7 Textured, Sirolimus-Loaded, and Deformed Group

The final group consists of samples which were flattened to ~75 μm, nanotextured by RF plasma, loaded with sirolimus, and then deformed by rolling to ~55 μm. The cumulative release profile in figure 6.6 is quite obviously extended for the first four weeks or so of the trial before reaching a totaled average release of ~21 μg indicating a load density of ~0.26 mg/cm^2. As with the deformed paclitaxel sample, the majority of release occurs during the initial burst phase with ~35% occurring in the first two hours and ~70% in the first day. Figure 6.7 shows the burst phase peaking at a suppressed rate of ~150 μg/day and the extended release rate exceeding both the untextured and textured groups over at least the first four weeks of the trial. Consistent with the paclitaxel trial, the deformed surface appears to have delayed drug diffusion from the surface.

6.7 Discussion of Controlled Release from RF Plasma Textured Stents

Drug release measurements indicate good consistency in sample preparation across all seven sample types as variance was low for both stepwise and total release within groups. Loading levels were fairly even as well, especially within drugs as paclitaxel samples were all near 0.36 mg/cm^2 and sirolimus samples all near 0.27 mg/cm^2. SEM micrographs as in figures 6.1-6.3 revealed consistent structure along the length and width of sample surfaces with structure diminishing only near the periphery of the flattened MP35N due to edge effects during RF plasma texturing. Variations in drug load may be accounted for by differences in positioning during loading, slight differences in loading solution concentration, uneven ethanol evaporation, surface

affinities, or general randomness. In every tested case, samples which were textured, then loaded, and then deformed exhibited extended drug release profiles in comparison to the untextured and undeformed groups. By direct manipulation of the metallic surface, a BMS could perform like a DES without the necessity of additional coatings which may contribute to late thrombosis risk.

Tables 6.1 and 6.2 present statistical analysis of the paclitaxel-loaded and sirolimus-loaded groups respectively and indicate significant differences between groupings. Sample types are designated as follows: "C" for the untextured, unloaded, control samples; "U" for the untextured, drug-loaded samples; "T" for the textured, drug-loaded samples; and "D" for the textured, drug-loaded, and deformed samples. Analysis was performed on both stepwise data and cumulative totals to illustrate separate aspects of the results. In either case, ANOVA p-values less than 0.05 suggest statistical differences among the compared groups. Tukey HSD p-values then identify the significant differences between pairs with values less than 0.01 indicating the 99% confidence interval and values less than 0.05 indicating the 95% confidence interval. In the stepwise cases where only the two groups C and D were measured (Days 7, 13, 17, and 29), the ANOVA p-value reduces to a student's t-test. For days 10, 22, and 40 the stepwise analysis across all four groups was performed by summing the release from interval measurements of the C and D groups. Cumulative data from the control group was not included here as the differences in total drug released between the unloaded control group and the loaded groups is uniformly obvious throughout the trial (all p-values would fall in the $p < 0.01$ range).

Table 6.1. Paclitaxel release samples statistical summary confirming significance for the extended release from the deformed group. C indicates the untextured, unloaded control group; U indicates the untextured, paclitaxel-loaded group; T indicates the textured, paclitaxel-loaded group, D indicates the deformed, textured, paclitaxel-loaded group. A

Data	Stepwise							Cumulative			
Test	ANOVA	Tukey HSD p-value						ANOVA	Tukey HSD p-value		
Groups	p-value	C vs U	C vs T	C vs D	U vs T	U vs D	T vs D	p-value	U vs T	U vs D	T vsD
Hr 1	2.8E-11	0.001	0.001	0.001	0.001	0.001	0.003	4.4E-07	0.001	0.001	0.006
Hr 2	6.1E-06	0.001	0.001	0.045	0.900	0.012	0.003	1.2E-05	0.047	0.001	0.001
Hr 3	1.3E-02	0.067	0.102	0.010	0.900	0.748	0.625	2.1E-05	0.048	0.001	0.001
Hr 6	2.7E-07	0.010	0.001	0.001	0.003	0.001	0.567	6.4E-05	0.143	0.001	0.001
Hr 12	3.2E-05	0.001	0.001	0.001	0.900	0.333	0.191	1.0E-04	0.134	0.001	0.004
Day 1	1.1E-08	0.002	0.001	0.001	0.223	0.001	0.001	3.0E-04	0.164	0.001	0.007
Day 2	6.1E-08	0.014	0.001	0.001	0.214	0.001	0.001	1.6E-03	0.252	0.001	0.025
Day 3	1.6E-09	0.007	0.001	0.001	0.127	0.001	0.001	6.8E-03	0.327	0.005	0.078
Day 5	5.3E-06	0.881	0.009	0.001	0.039	0.001	0.010	3.9E-02	0.557	0.033	0.198
Day 7	5.4E-07	-	-	0.001	-	-	-	-	-	-	-
Day 10	4.8E-07	0.900	0.265	0.005	0.530	0.001	0.001	3.5E-01	0.695	0.315	0.750
Day 13	4.3E-05	-	-	0.001	-	-	-	-	-	-	-
Day 17	8.8E-03	-	-	0.009	-	-	-	-	-	-	-
Day 22	2.0E-07	0.554	0.865	0.001	0.201	0.001	0.001	8.0E-01	0.808	0.831	0.900
Day 29	2.4E-02	-	-	0.024	-	-	-	-	-	-	-
Day 40	1.0E-04	0.900	0.900	0.001	0.900	0.001	0.001	8.2E-01	0.801	0.900	0.900

The paclitaxel release statistical analysis in table 6.1 suggests significant differences among each of the four tested groups. The primary group of interest is D with the textured, loaded, and deformed samples. This deformed group is statistically different to the unloaded control group at each step throughout the trial indicating continued drug release even in the later measurements. The suppressed C vs. D p-values on day 22 and 40 may be artifacts of summing intervening concentration measurements for comparison to groups U and T but the continued significance in comparison to the control in the interim adds weight to a conclusion for statistical distinction. In contrast to the D group, the textured and paclitaxel-loaded T group is indistinguishable from the unloaded control group C after day 5 of the trial. Similarly, the untextured paclitaxel-loaded U group is only statistically separate from the unloaded control group up to day 3. Groups U and T perform in comparable fashion throughout the experiment with only a few separable release points stepwise. The deformed group remains distinct from U or T for the majority of time points with the overlap on the first day corresponding to the cross point where deformed samples continued to release paclitaxel as the untextured and textured groups paclitaxel release diminished. The D group outperformed both the U and T groups consistently through day 40 and the end of the trial. From a cumulative release perspective, groups U and T were only distinguishable through the third hour of release. The deformed group, with an extended release rate, remained separable from group T until day 5 and from group U until day 10. Over the course of the trial, the total paclitaxel released by the U, T, and D groups was statistically indistinct.

Table 6.2. Sirolimus release samples statistical summary confirming significance for the extended release from the deformed group. C indicates the untextured, unloaded control group; U indicates the untextured, sirolimus-loaded group; T indicates the textured, sirolimus-loaded group, D indicates the deformed, textured, sirolimus-loaded group.

Data	Stepwise							Cumulative			
Test	ANOVA	Tukey HSD p-value						ANOVA	Tukey HSD p-value		
Groups	p-value	C vs U	C vs T	C vs D	U vs T	U vs D	T vs D	p-value	U vs T	U vs D	T vsD
Hr 1	1.9E-07	0.001	0.001	0.001	0.059	0.001	0.201	4.2E-03	0.078	0.003	0.209
Hr 2	2.8E-10	0.001	0.001	0.030	0.002	0.001	0.001	3.0E-04	0.855	0.001	0.001
Hr 3	4.9E-05	0.001	0.001	0.001	0.900	0.900	0.900	2.0E-04	0.838	0.001	0.001
Hr 6	3.0E-08	0.001	0.001	0.001	0.900	0.003	0.004	6.0E-04	0.841	0.001	0.002
Hr 12	2.5E-03	0.171	0.141	0.001	0.900	0.094	0.115	1.1E-03	0.841	0.002	0.004
Day 1	7.0E-04	0.008	0.062	0.001	0.723	0.508	0.111	3.8E-03	0.763	0.005	0.016
Day 2	3.0E-04	0.844	0.273	0.001	0.681	0.001	0.012	1.3E-02	0.842	0.015	0.040
Day 3	2.2E-06	0.594	0.379	0.001	0.900	0.001	0.001	3.0E-02	0.859	0.033	0.082
Day 5	1.8E-05	0.900	0.900	0.001	0.900	0.001	0.001	1.2E-01	0.866	0.120	0.264
Day 7	4.9E-02	-	-	0.049	-	-	-	-	-	-	-
Day 10	8.0E-05	0.611	0.623	0.002	0.900	0.001	0.001	4.4E-01	0.869	0.413	0.690
Day 13	1.0E-04	-	-	0.001	-	-	-	-	-	-	-
Day 17	9.6E-03	-	-	0.010	-	-	-	-	-	-	-
Day 22	1.9E-06	0.247	0.214	0.001	0.900	0.001	0.001	8.3E-01	0.857	0.849	0.900
Day 29	1.2E-01	-	-	0.115	-	-	-	-	-	-	-
Day 40	7.0E-04	0.494	0.347	0.034	0.900	0.002	0.001	8.6E-01	0.846	0.900	0.900

The statistical indicators of sirolimus release as presented in table 6.2 are in general form very similar to the paclitaxel-release analysis from table 6.1. Again the textured, loaded, and deformed samples remained distinguishable from the unloaded control group throughout the trial (with exception of the day 29 measurement) and distinct from the U and T groups with exception of the crossover point in the latter part of the first day of release. The untextured sirolimus-loaded group U and the textured sirolimus-loaded group T are even more similar than the paclitaxel analogues with only a single statistically different measurement point in either the stepwise or cumulative analyses. Additionally, for the sirolimus U and T groups, distinction from the unloaded control group disappears after the first day of release. As with the paclitaxel group, the cumulative release of sirolimus from the deformed samples remains separable from the U and T groups in the early part of the experiment but by the trial's end the total amount of sirolimus released is not statistically dissimilar across the loaded groups.

In both the sirolimus and paclitaxel tests, the drug release kinetics of those samples which had been textured, then loaded with drug, and finally deformed by rolling were clearly different than those samples which were either unloaded, untextured, or textured but not deformed. The changes in surface morphology evidently restricted both the immediate and prolonged diffusion of sirolimus or paclitaxel from the metal. As an advantageous and unexpected surprise, the release data seems to indicate that little to no drug was lost from the MP35N surface during the rolling process. The drug itself, sirolimus or paclitaxel, had little if any effect on

the overall release profile results which are highly similar in each case in both cumulative release and release rate.

While the results are promising, the release profile is not sufficiently extended to compare favorably with those DES approved for clinical use in the United States. For instance the Resolute Integrity® drug-eluting stent releases 85% of its zotarolimus within 60 days and the remainder within 180 days[105]. For clinical use, greater restrictions on drug diffusion will be required. This may be accomplished by deepening the surface texture either through additional repetitions in the RF plasma texturing process, selection of a material more susceptible to plasma texturing, or a different strategy to texture the metal surface. It may also be possible to further restrict diffusion by more extensive surface deformations following loading. As this undertaking was intended to demonstrate the feasibility of controlling drug release with surface morphology without the addition of any material beyond the drugs themselves nothing was done to control drug concentration and loading levels, for clinical use either higher or lower concentrations may be necessary depending on stent form factor. Also of potential concern is the long-term susceptibility of the nanotextured metal surface to degradation in body environment. Future in vivo investigations should be undertaken to preclude such possibility. The structural differences between single samples and a functioning stent also must be considered. The processes used to produce samples individually could be extended to a manufacturing environment but not without challenges to overcome. For instance, stent struts may need to be produced individually to avoid shielding problems during

plasma texturing and rather than rolling, deformation would likely require drawing which could present issues with uneven deformation. Generally, bare-metal surface morphology may be used to control drug release, but there remains much work to be done before a functional stent could exploit this property to prevent restenosis.

Chapter 6, in full, is from material being prepared for publication as "Extended Release of Paclitaxel and Sirolimus from Bare-Metal Stent Surface by RF-Plasma Nanotexturing and Subsequent Deformation" with intended submission to the Journal of Controlled Release. Jennifer He, Gary W. Johnston, Sungho Jin, and Renkun Chen are co-authors. The dissertation author is the primary investigator and author of this material.

Chapter 7: Overall Summary, Conclusions, and Future Work

In this dissertation, the development of fully metallic nanoscale surface texturing through exposure to a radio-frequency plasma was systematically explored with a particular emphasis on potential biomedical applications. This work has been an important step to further understanding the prospects and limitations of a novel material processing technique. Nanostructures and their specialized propertied continue to generate significant scientific interest with good reason. The possibilities explored herein reveal considerable promise for medical devices produced by RF plasma texturing to save lives, improve patient outcomes, and aid future biomedical and neurophysiological research.

7.1 RF Plasma Nanotexturing Contributions and Direction

Surface texturing of MP35N wires by RF plasma was systematically explored and optimized for single run structure depth for particular values of processing power, chamber pressure, and duration. Texturing with differing plasma materials was explored, with argon outperforming both nitrogen and hydrogen. A procedure for determining structure depth through sectioning and brittle fracture was developed. Texturing was extended beyond simple wire geometries to foil and sharpened tips. Additional sample materials were textured including Ni-Cr (80/20), inconel alloy, copper, 316L stainless steel, 304 stainless steel, copper, and various Pt-Ir alloy concentrations. For materials that resisted texturing, a process of transfer etching from a texturable sputtered material was developed and used to texture tantalum. The extension of texturing to single-phase materials such as Ni-Cr (80/20) controverted an

earlier hypothesis for the texturing mechanism and suggested additional explanations such as ion bombardment or microstructure irregularities.

Future directions include the continued extension of RF plasma texturing to additional materials and geometries. Deformations near high curvature edges and shielding of concave surfaces each present particular challenges to be overcome. Continued investigations will also further illuminate the texturing mechanism.

7.2 Repetitive Processing Contributions and Direction

Repetitive RF plasma processing was successfully demonstrated to increase nanostructure depth with indications that the heating/cooling of the sample surface is integral to the deepening process. MP35N samples repetitively textured 10 times had nanowire structure deepened to ~7-10 μm, the deepest yet achieved by RF plasma texturing. Repetitive texturing was extended to foil and sharp tip geometries as well as assorted materials beyond MP35N. Bovine aortic endothelial cells were confirmed to form a smooth, organized, endothelial layer on repetitively textured MP35N.

Future investigations should explore the limit of repetitive texturing for samples with more initial material as well as the precise mechanism for structure deepening upon repetition. Improvement is also needed in deepening foil geometries.

7.3 Electrode Impedance Contributions and Direction

RF plasma texturing to increase structure depth and surface area was used to decrease electrode impedance in an electrolyte simulating body fluid for both wire and foil electrode geometries. Conductivity was maintained in antibiofouling electrodes

selectively coated with PTFE by first decreasing the surface impedance through texturing.

Future research in this area should focus on in vivo measurements and overcoming the inconsistent increase in surface impedance for RF plasma textured, PTFE-coated wire electrodes.

7.4 Antibiofouling Electrode Contributions and Direction

Novel antibiofouling electrodes with an RF processed nanotextured surface and selective hydrophobic PTFE coating were constructed. Cell culture revealed significantly less cell adhesion on the antibiofouling surface after 10 days of incubation along with decreased cell viability. Antibiofouling electrodes were demonstrated to have similar electrical properties to plain polished electrodes but to be substantially less susceptible to biofouling.

To develop this technology for long-term implantation as a stimulating or recording electrode, in vivo studies are needed to investigate cell response and the possibility of PTFE delamination. Alternative antifouling coatings also offer an opportunity for worthwhile exploration.

7.5 Controlled Drug-Release Contributions and Direction

Extended anti-restenosis drug release was demonstrated from a stent without the addition of anything to the surface of a metal besides the eluted drug. As well as prolonging release for at least 20 days, the surface structure successfully suppressed the initial burst of drug upon insertion into simulated biological fluid. In comparison

to samples which were either not textured or not deformed, an MP35N stent surface that was textured by repetitive exposure to RF plasma, loaded with either sirolimus or paclitaxel, and then deformed by rolling to flatten the surface features and restrict the release of drug from the surface exhibited statistically dissimilar drug release characteristics without reduction in the total amount of delivered drug.

With this demonstration of feasibility, bare-metal drug-elution offers a promising avenue for future stent design and the potential for improved patient outcomes. The development of a hybrid DES and BMS which offers controllable extended anti-restenosis drug release but without the addition of anything besides the active drug to the metallic stent has great potential. Such a bare-metal drug-eluting stent could potentially maintain the advantageous properties of DES while also reducing the risk for late thrombosis.

References

1. Loya, M. C., Park, E., Chen, L. H., Brammer, K. S. & Jin, S. Radially arrayed nanopillar formation on metallic stent wire surface via radio-frequency plasma. *Acta Biomaterialia* **6,** 1671–1677 (2010).

2. Seker, E., Berdichevsky, Y., Begley, M. R., Reed, M. L., Staley, K. J. & Yarmush, M. L. The fabrication of low-impedance nanoporous gold multiple-electrode arrays for neural electrophysiology studies. *Nanotechnology* **21,** 125504 (2010).

3. Loeb, G. E. Cochlear Prosthetics. *Annual Review of Neuroscience* **13,** 357–371 (1990).

4. Wisniewski, N. & Reichert, M. Methods for reducing biosensor membrane biofouling. *Colloids Surf B Biointerfaces* **18,** 197–219 (2000).

5. Polikov, V. S., Block, M. L., Fellous, J.-M., Hong, J.-S. & Reichert, W. M. In vitro model of glial scarring around neuroelectrodes chronically implanted in the CNS. *Biomaterials* **27,** 5368–5376 (2006).

6. Loya, M. C., Brammer, K. S., Choi, C., Chen, L.-H. & Jin, S. Plasma-induced nanopillars on bare metal coronary stent surface for enhanced endothelialization. *Acta Biomaterialia* **6,** 4589–4595 (2010).

7. Etsion, I. State of the Art in Laser Surface Texturing. *Journal of Tribology* **127,** 248 (2005).

8. Bolzan, A. E., Castro Luna, A. M., Visintin, A., Salvarezza, R. C. & Arvia, A. J. Smooth and rough platinum deposits resulting from the electroreduction of hydrous oxide platinum overlayers—a mechanistic approach. *Electrochimica Acta* **33,** 1743–1751 (1988).

9. Loya, M. Design and fabrication of advanced surface microstructures: surface modification of cardiovascular stent wires via RF plasma processing. (2010).

10. Gardner, C. J., Trisnadi, J., Kim, T. K., Brammer, K., Reiss, L., Chen, L. & Jin, S. Controlled metallic nanopillars for low impedance biomedical electrode. *Acta Biomaterialia* **10,** 2296–2303 (2014).

11. Cogan, S. F. Neural Stimulation and Recording Electrodes. *Annual Review of Biomedical Engineering* **10,** 275–309 (2008).

12. Polikov, V. S., Tresco, P. A. & Reichert, W. M. Response of brain tissue to chronically implanted neural electrodes. *Journal of Neuroscience Methods* **148,** 1–18 (2005).

13. Mussa-Ivaldi, F. A. & Miller, L. E. Brain-machine interfaces: computational demands and clinical needs meet basic neuroscience. *Trends Neurosci.* **26,** 329–334 (2003).

14. Lebedev, M. A. & Nicolelis, M. A. L. Brain–machine interfaces: past, present and future. *Trends in Neurosciences* **29,** 536–546 (2006).

15. Tykocinski, M., Duan, Y., Tabor, B. & Cowan, R. S. Chronic electrical stimulation of the auditory nerve using high surface area (HiQ) platinum electrodes. *Hearing Research* **159,** 53–68 (2001).

16. Horner, P. J. & Gage, F. H. Regenerating the damaged central nervous system. *Nature* **407,** 963–970 (2000).

17. Schwartz, A. B., Cui, X. T., Weber, D. J. & Moran, D. W. Brain-Controlled Interfaces: Movement Restoration with Neural Prosthetics. *Neuron* **52,** 205–220 (2006).

18. Carmena, J. M., Lebedev, M. A., Crist, R. E., O'Doherty, J. E., Santucci, D. M., Dimitrov, D. F., Patil, P. G., Henriquez, C. S. & Nicolelis, M. A. L. Learning to Control a Brain–Machine Interface for Reaching and Grasping by Primates. *PLoS Biol* **1,** e42 (2003).

19. Hochberg, L. R., Serruya, M. D., Friehs, G. M., Mukand, J. A., Saleh, M., Caplan, A. H., Branner, A., Chen, D., Penn, R. D. & Donoghue, J. P. Neuronal ensemble control of prosthetic devices by a human with tetraplegia. *Nature* **442,** 164–171 (2006).

20. Lebedev, M. A., Carmena, J. M., O'Doherty, J. E., Zacksenhouse, M., Henriquez, C. S., Principe, J. C. & Nicolelis, M. A. L. Cortical Ensemble Adaptation to Represent Velocity of an Artificial Actuator Controlled by a Brain-Machine Interface. *J. Neurosci.* **25,** 4681–4693 (2005).

21. McConnell, G. C., Rees, H. D., Levey, A. I., Gutekunst, C.-A., Gross, R. E. & Bellamkonda, R. V. Implanted neural electrodes cause chronic, local inflammation that is correlated with local neurodegeneration. *J. Neural Eng.* **6,** 056003 (2009).

22. Serruya, M. D., Hatsopoulos, N. G., Paninski, L., Fellows, M. R. & Donoghue, J. P. Brain-machine interface: Instant neural control of a movement signal. *Nature* **416,** 141–142 (2002).

23. Webster, T. J., Waid, M. C., McKenzie, J. L., Price, R. L. & Ejiofor, J. U. Nano-biotechnology: carbon nanofibres as improved neural and orthopaedic implants. *Nanotechnology* **15,** 48 (2004).

24. Williams, J. C., Rennaker, R. L. & Kipke, D. R. Long-term neural recording characteristics of wire microelectrode arrays implanted in cerebral cortex. *Brain Res. Brain Res. Protoc.* **4,** 303–313 (1999).

25. Gingerich, M. D., Wiler, J. A. & Wise, K. D. Use of an active microelectrode array for stimulation and recording in the central nervous system. in *BMES/EMBS Conference, 1999. Proceedings of the First Joint* **1,** 471–vol (IEEE, 1999).

26. Bellamkonda, R. V., Pai, S. B. & Renaud, P. Materials for neural interfaces. *MRS Bulletin* **37,** 557–561 (2012).

27. Nicolelis, M. A. L., Dimitrov, D., Carmena, J. M., Crist, R., Lehew, G., Kralik, J. D. & Wise, S. P. Chronic, multisite, multielectrode recordings in macaque monkeys. *PNAS* **100,** 11041–11046 (2003).

28. Geddes, L. A. & Roeder, R. Criteria for the Selection of Materials for Implanted Electrodes. *Annals of Biomedical Engineering* **31,** 879–890 (2003).

29. Biran, R., Martin, D. C. & Tresco, P. A. Neuronal cell loss accompanies the brain tissue response to chronically implanted silicon microelectrode arrays. *Experimental Neurology* **195,** 115–126 (2005).

30. Brammer, K. S., Oh, S., Gallagher, J. O. & Jin, S. Enhanced Cellular Mobility Guided by TiO2 Nanotube Surfaces. *Nano Lett.* **8,** 786–793 (2008).

31. Joner, M., Finn, A. V., Farb, A., Mont, E. K., Kolodgie, F. D., Ladich, E., Kutys, R., Skorija, K., Gold, H. K. & Virmani, R. Pathology of Drug-Eluting Stents in Humans: Delayed Healing and Late Thrombotic Risk. *Journal of the American College of Cardiology* **48,** 193–202 (2006).

32. Versari, D., Lerman, L. & Lerman, A. The Importance of Reendothelialization After Arterial Injury. *Current Pharmaceutical Design* **13,** 1811–1824 (2007).

33. Bjursten, L. M., Rasmusson, L., Oh, S., Smith, G. C., Brammer, K. S. & Jin, S. Titanium dioxide nanotubes enhance bone bonding in vivo. *Journal of Biomedical Materials Research Part A* **92A,** 1218–1224 (2010).

34. Oh, S., Brammer, K. S., Li, Y. S. J., Teng, D., Engler, A. J., Chien, S. & Jin, S. Stem cell fate dictated solely by altered nanotube dimension. *PNAS* **106,** 2130–2135 (2009).

35. Brammer, K. S., Oh, S., Frandsen, C. J. & Jin, S. TiO2 nanotube structures for enhanced cell and biological functionality. *JOM* **62,** 50–55 (2010).

36. Nam, Y. Material considerations for in vitro neural interface technology. *MRS Bulletin* **37,** 566–572 (2012).

37. Schwartz, A. B. Cortical Neural Prosthetics. *Annual Review of Neuroscience* **27,** 487–507 (2004).

38. Gool, W. A. V., Walstra, G. J. M., Teunisse, S., Zant, F. M. V. der, Weinstein, H. C. & Royen, E. A. V. Diagnosing Alzheimer's disease in elderly, mildly demented patients: the impact of routine single photon emission computed tomography. *J Neurol* **242,** 401–405 (1995).

39. Temussi, P. A., Masino, L. & Pastore, A. From Alzheimer to Huntington: why is a structural understanding so difficult? *EMBO J* **22,** 355–61 (2003).

40. Nieuwenhuis-Mark, R. E. Diagnosing Alzheimer's dementia in Down syndrome: Problems and possible solutions. *Research in Developmental Disabilities* **30,** 827–838 (2009).

41. HajjHassan, M., Chodavarapu, V. & Musallam, S. NeuroMEMS: Neural Probe Microtechnologies. *Sensors* **8,** 6704–6726 (2008).

42. McCreery, D., Lossinsky, A., Pikov, V. & Liu, X. Microelectrode Array for Chronic Deep-Brain Microstimulation and Recording. *IEEE Transactions on Biomedical Engineering* **53,** 726–737 (2006).

43. Morin, F. O., Takamura, Y. & Tamiya, E. Investigating neuronal activity with planar microelectrode arrays: achievements and new perspectives. *Journal of Bioscience and Bioengineering* **100,** 131–143 (2005).

44. Veraart, C., Raftopoulos, C., Mortimer, J. T., Delbeke, J., Pins, D., Michaux, G., Vanlierde, A., Parrini, S. & Wanet-Defalque, M.-C. Visual sensations produced by optic nerve stimulation using an implanted self-sizing spiral cuff electrode. *Brain research* **813,** 181–186 (1998).

45. Akin, T., Najafi, K., Smoke, R. H. & Bradley, R. M. A micromachined silicon sieve electrode for nerve regeneration applications. *Biomedical Engineering, IEEE Transactions on* **41,** 305–313 (1994).

46. Jia, X., Zhen, G., Puttgen, A., Zhang, J. & Chen, T. Improved long-term recording of nerve signal by modified intrafascicular electrodes in rabbits. *Microsurgery* **28,** 173–178 (2008).

47. Saunders, E., Cohen, L., Aschendorff, A., Shapiro, W., Knight, M., Stecker, M., Richter, B., Waltzman, S., Tykocinski, M. & Roland, T. Threshold, comfortable level and impedance changes as a function of electrode-modiolar distance. *Ear and hearing* **23,** 28S–40S (2002).

48. Ahmed, R. & Reifsnider, K. Study of Influence of Electrode Geometry on Impedance Spectroscopy. *Int. J. Electrochem. Sci* **6,** 1159–1174 (2011).

49. De Levie, R. On porous electrodes in electrolyte solutions: I. Capacitance effects. *Electrochimica Acta* **8,** 751–780 (1963).

50. Moracchini, P. V., Cornacchia, D., Bernasconi, M., Tesorieri, M. C., Fabbri, M., Marzegalli, M., Baraldi, P., Corte, T., Giuliani, M. & Marotta, T. High Impedance Low Energy Pacing Leads: Long-Term Results With a Very Small Surface Area Steroid-Eluting Lead Compared to Three Conventional Electrodes. *Pacing and clinical electrophysiology* **22,** 326–334 (1999).

51. Hughes, H. C., Brownlee, R. R. & Tyers, G. F. Failure of demand pacing with small surface area electrodes. *Circulation* **54,** 128–132 (1976).

52. Furman, S., Parker, B. & Escher, D. J. Decreasing electrode size and increasing efficiency of cardiac stimulation. *Journal of Surgical Research* **11,** 105–110 (1971).

53. Hughes, M. L., Vander Werff, K. R., Brown, C. J., Abbas, P. J., Kelsay, D. M., Teagle, H. F. & Lowder, M. W. A longitudinal study of electrode impedance, the electrically evoked compound action potential, and behavioral measures in nucleus 24 cochlear implant users. *Ear and hearing* **22,** 471–486 (2001).

54. Franks, W., Schenker, I., Schmutz, P. & Hierlemann, A. Impedance Characterization and Modeling of Electrodes for Biomedical Applications. *IEEE Transactions on Biomedical Engineering* **52,** 1295–1302 (2005).

55. Dymond, A. M. Characteristics of the metal-tissue interface of stimulation electrodes. *Biomedical Engineering, IEEE Transactions on* 274–280 (1976).

56. Ovadia, M. & Zavitz, D. H. The Electrode–Tissue Interface in Living Heart: Equivalent Circuit as a Function of Surface Area. *Electroanalysis* **10,** 262–272 (1998).

57. Boer, R. W. de & Oosterom, A. van. Electrical properties of platinum electrodes: impedance measurements and time-domain analysis. *Medical & Biological Engineering & Computing* **16,** 1–10 (1978).

58. Schwan, H. P. Electrode polarization impedance and measurements in biological materials. *Annals of the New York Academy of Sciences* **148,** 191–209 (1968).

59. Cui, X., Hetkeb, J. F., Wilerc, J. A., Andersonb, D. J. & Martina, D. C. Electrochemical deposition and characterization of conducting polymer polypyrrole/PSS on multichannel neural probes. *Sensors and Actuators A* **93,** 18 (2001).

60. Cui, X., Lee, V. A., Raphael, Y., Wiler, J. A., Hetke, J. F., Anderson, D. J. & Martin, D. C. Surface modification of neural recording electrodes with conducting polymer/biomolecule blends. *Journal of biomedical materials research* **56,** 261–272 (2001).

61. Norlin, A., Pan, J. & Leygraf, C. Investigation of interfacial capacitance of Pt, Ti and TiN coated electrodes by electrochemical impedance spectroscopy. *Biomolecular engineering* **19,** 67–71 (2002).

62. Schmidt, E. M., Bak, M. J., Hambrecht, F. T., Kufta, C. V., O'rourke, D. K. & Vallabhanath, P. Feasibility of a visual prosthesis for the blind based on intracortical micro stimulation of the visual cortex. *Brain* **119,** 507–522 (1996).

63. Clark, G. M. The multiple-channel cochlear implant: the interface between sound and the central nervous system for hearing, speech, and language in deaf people--a personal perspective. *Philosophical Transactions of the Royal Society B: Biological Sciences* **361,** 791–810 (2006).

64. Prochazka, A., Mushahwar, V. K. & McCreery, D. B. Neural prostheses. *The Journal of physiology* **533,** 99–109 (2001).

65. Perlmutter, J. S. & Mink, J. W. Deep brain stimulation. *Annu. Rev. Neurosci.* **29,** 229–257 (2006).

66. Butson, C. R. & McIntyre, C. C. Tissue and electrode capacitance reduce neural activation volumes during deep brain stimulation. *Clinical Neurophysiology* **116,** 2490–2500 (2005).

67. Buzsáki, G. Large-scale recording of neuronal ensembles. *Nature Neuroscience* **7,** 446–451 (2004).

68. Werner, C., Maitz, M. F. & Sperling, C. Current strategies towards hemocompatible coatings. *Journal of Materials Chemistry* **17,** 3376 (2007).

69. Krishnan, S., Weinman, C. J. & Ober, C. K. Advances in polymers for anti-biofouling surfaces. *Journal of Materials Chemistry* **18,** 3405 (2008).

70. Brammer, K. S., Choi, C., Oh, S., Cobb, C. J., Connelly, L. S., Loya, M., Kong, S. D. & Jin, S. Antibiofouling, sustained antibiotic release by Si nanowire templates. *Nano Lett.* **9,** 3570–3574 (2009).

71. Kotov, N. A., Winter, J. O., Clements, I. P., Jan, E., Timko, B. P., Campidelli, S., Pathak, S., Mazzatenta, A., Lieber, C. M., Prato, M., Bellamkonda, R. V., Silva, G. A., Kam, N. W. S., Patolsky, F. & Ballerini, L. Nanomaterials for Neural Interfaces. *Advanced Materials* **21,** 3970–4004 (2009).

72. Michiels, C. Endothelial cell functions. *J. Cell. Physiol.* **196,** 430–443 (2003).

73. Heldman, A. W., Cheng, L., Jenkins, G. M., Heller, P. F., Kim, D.-W., Ware, M., Nater, C., Hruban, R. H., Rezai, B., Abella, B. S., Bunge, K. E., Kinsella, J. L., Sollott, S. J., Lakatta, E. G., Brinker, J. A., Hunter, W. L. & Froehlich, J. P. Paclitaxel stent coating inhibits neointimal hyperplasia at 4 weeks in a porcine model of coronary restenosis. *Circulation* **103,** 2289–2295 (2001).

74. Daemen, J., Wenaweser, P., Tsuchida, K., Abrecht, L., Vaina, S., Morger, C., Kukreja, N., Jüni, P., Sianos, G., Hellige, G., van Domburg, R. T., Hess, O. M., Boersma, E., Meier, B., Windecker, S. & Serruys, P. W. Early and late coronary stent thrombosis of sirolimus-eluting and paclitaxel-eluting stents in routine clinical practice: data from a large two-institutional cohort study. *The Lancet* **369,** 667–678 (2007).

75. Bavry, A. A., Kumbhani, D. J., Helton, T. J., Borek, P. P., Mood, G. R. & Bhatt, D. L. Late Thrombosis of Drug-Eluting Stents: A Meta-Analysis of Randomized Clinical Trials. *The American Journal of Medicine* **119,** 1056–1061 (2006).

76. Murphy, S. L., Xu, J. & Kochanek, K. D. National vital statistics reports. *National vital statistics reports* **61,** (2013).

77. Raval, A., Choubey, A., Engineer, C., Kotadia, H. & Kothwala, D. Novel biodegradable polymeric matrix coated cardiovascular stent for controlled drug delivery. *Trends in Biomaterials & Artificial Organs* **20,** (2007).

78. Stone, G. W., Ellis, S. G., Cannon, L., Mann, J. T., Greenberg, J. D., Spriggs, D., O'Shaughnessy, C. D., DeMaio, S., Hall, P., Popma, J. J. , Koglin, J. & Russell, M. E. Comparison of a polymer-based paclitaxel-eluting stent with a bare metal stent in patients with complex coronary artery disease: a randomized controlled trial. *Jama* **294,** 1215–1223 (2005).

79. Colombo, A. Randomized Study to Assess the Effectiveness of Slow- and Moderate-Release Polymer-Based Paclitaxel-Eluting Stents for Coronary Artery Lesions. *Circulation* **108,** 788–794 (2003).

80. Morice, M.-C., Serruys, P. W., Sousa, J. E., Fajadet, J., Ban Hayashi, E., Perin, M., Colombo, A., Schuler, G., Barragan, P., Guagliumi, G., Molnàr, F. & Falotico, R. A randomized comparison of a sirolimus-eluting stent with a

standard stent for coronary revascularization. *New England Journal of Medicine* **346,** 1773–1780 (2002).

81. Patel, M. R., Marso, S. P., Dai, D., Anstrom, K. J., Shunk, K. A., Curtus, J. P., Brennan, J. M., Sedrakyan, A., Messenger, J. C. & Douglas, P. S. Comparative Effectiveness of Drug-Eluting Versus Bare-Metal Stents in Elderly Patients Undergoing Revascularization of Chronic Total Coronary Occlusions. *JACC: Cardiovascular Interventions* **5,** 1054–1061 (2012).

82. Navarese, E., Kubica, J., Castriota, F., Gibson, C. M., De Luca, G., Buffon, A., Bolognese, L., Margheri, M., Andreotti, F., Di Mario, C. & De Servi, S. Safety and efficacy of biodegradable vs. durable polymer drug-eluting stents: evidence from a meta-analysis of randomised trials. *EuroIntervention* **7,** 985–994 (2011).

83. Moses, J. W., Leon, M. B., Popma, J. J., Fitzgerald, P. J., Holmes, D. R., O'Shaughnessy, C., Caputo, R. P., Kereiakes, D. J., Williams, D. O., Teirstein, P. S., Jaeger, J. L. & Kuntz, R. E. Sirolimus-eluting stents versus standard stents in patients with stenosis in a native coronary artery. *New England Journal of Medicine* **349,** 1315–1323 (2003).

84. Kamath, K. R., Barry, J. J. & Miller, K. M. The Taxus^{TM} drug-eluting stent: A new paradigm in controlled drug delivery. *Advanced Drug Delivery Reviews* **58,** 412–436 (2006).

85. Daemen, J. & Serruys, P. W. Drug-Eluting Stent Update 2007: Part II: Unsettled Issues. *Circulation* **116,** 961–968 (2007).

86. Yamamoto, M., Takano, M., Murakami, D., Inami, T., Kobayashi, N., Inami, S., Okamatsu, K., Ohba, T., Ibuki, C., Hata, N., Seino, Y., Jang, I.-K. & Mizuno, K. The possibility of delayed arterial healing 5 years after implantation of sirolimus-eluting stents: Serial observations by coronary angioscopy. *American Heart Journal* **161,** 1200–1206 (2011).

87. Lagerqvist, B., James, S. K., Stenestrand, U., Lindbäck, J., Nilsson, T. & Wallentin, L. Long-term outcomes with drug-eluting stents versus bare-metal stents in Sweden. *New England Journal of Medicine* **356,** 1009–1019 (2007).

88. Kimura, T., Morimoto, T., Nakagawa, Y., Kawai, K., Miyazaki, S., Muramatsu, T., Shiode, N., Namura, M., Sone, T., Oshima, S., Nishikawa, H., Hiasa, Y., Hayashi, Y., Nobuyoshi, M. & Mitudo, K. Very late stent thrombosis and late target lesion revascularization after sirolimus-eluting stent implantation five-year outcome of the j-Cypher Registry. *Circulation* **125,** 584–591 (2012).

89. Ong, A. T. L., Hoye, A., Aoki, J., van Mieghem, C. A. G., Rodriguez Granillo, G. A., Sonnenschein, K., Regar, E., McFadden, E. P., Sianos, G., van der

Giessen, W. J., de Jaegere, P. P. T., de Feyter, P., van Domburg, R. T. & Serruys, P. W. Thirty-day incidence and six-month clinical outcome of thrombotic stent occlusion after bare-metal, sirolimus, or paclitaxel stent implantation. *Journal of the American College of Cardiology* **45,** 947–953 (2005).

90. Stettler, C., Wandel, S., Allemann, S., Kastrati, A., Morice, M. C., Schömig, A., Pfisterer, M. E., Stone, G. W., Leon, M. B., de Lezo, J. S., Goy, J.-J., Park, S.-J., Sabaté, M., Suttorp, M. J., Kelbaek, H., Spaulding, C., Menichelli, M., Vermeersch, P., Dirksen, M. T., Cervinka, P., Petronio, A. S., Nordmann, A. J., Diem, P., Meier, B., Zwahlen, M., Reichenbach, S., Trelle, S., Windecker, S. & Jüni, P. Outcomes associated with drug-eluting and bare-metal stents: a collaborative network meta-analysis. *The Lancet* **370,** 937–948 (2007).

91. Acharya, G. & Park, K. Mechanisms of controlled drug release from drug-eluting stents. *Advanced Drug Delivery Reviews* **58,** 387–401 (2006).

92. De la Torre Hernández, J. M. & Windecker, S. Very Late Stent Thrombosis With Newer Drug-Eluting Stents: No Longer an Issue? *Revista Española de Cardiología (English Edition)* **65,** 595–598 (2012).

93. Garg, S. & Serruys, P. W. Coronary Stents. *Journal of the American College of Cardiology* **56,** S43–S78 (2010).

94. Khan, W., Thipparaboina, R., Farah, S., Weinberger, J. Z. & Domb, A. J. in *Focal Controlled Drug Delivery* (eds. Domb, A. J. & Khan, W.) 387–403 (Springer US, 2014).

95. McGillicuddy, F. C., Lynch, I., Rochev, Y. A., Burke, M., Dawson, K. A., Gallagher, W. M. & Keenan, A. K. Novel 'plum pudding' gels as potential drug-eluting stent coatings: Controlled release of fluvastatin. *Journal of Biomedical Materials Research Part A* **79A,** 923–933 (2006).

96. Guo, X., Chang, R.-K. & Hussain, M. A. Ion-exchange resins as drug delivery carriers. *J Pharm Sci* **98,** 3886–3902 (2009).

97. Guo, Q., Knight, P. T. & Mather, P. T. Tailored drug release from biodegradable stent coatings based on hybrid polyurethanes. *Journal of Controlled Release* **137,** 224–233 (2009).

98. CYPHER P020026 approval letter. U.S. Food and Drug Administration, Center for Devices and Radiological Health. April 24, 2003. Retrieved March 27, 2015, from www.accessdata.fda.gov/cdrh_docs/pdf3/P020026a.pdf.

99. TAXUS Express-2 P030025 approval letter. U.S. Food and Drug Administration, Center for Devices and Radiological Health. March 4, 2004. Retrieved March 27, 2015, from www.accessdata.fda.gov/cdrh_docs/pdf3/P030025a.pdf.

100. TAXUS Liberté P060008 approval letter. U.S. Food and Drug Administration, Center for Devices and Radiological Health. October 10, 2008. Retrieved March 27, 2015, from www.accessdata.fda.gov/cdrh_docs/pdf6/P060008a.pdf.

101. TAXUS Liberté Atom P060008/S008 approval letter. U.S. Food and Drug Administration, Center for Devices and Radiological Health. May 21, 2009. Retrieved March 27, 2015, from www.accessdata.fda.gov/cdrh_docs/pdf6/P060008s008a.pdf.

102. TAXUS Liberté Long P060008/S011 approval letter. U.S. Food and Drug Administration, Center for Devices and Radiological Health. July 13, 2009. Retrieved March 27, 2015, from www.accessdata.fda.gov/cdrh_docs/pdf6/P060008s011a.pdf.

103. Endeavor P060033 approval letter. U.S. Food and Drug Administration, Center for Devices and Radiological Health. February 1, 2008. Retrieved March 27, 2015, from www.accessdata.fda.gov/cdrh_docs/pdf6/P060033a.pdf.

104. Resolute Integrity P110013 approval letter. U.S. Food and Drug Administration, Center for Devices and Radiological Health. February 17, 2012. Retrieved March 27, 2015, from www.accessdata.fda.gov/cdrh_docs/pdf11/P110013a.pdf.

105. Mukherjee, D., Burgos & Farrag. Resolute Integrity drug eluting stent safety and efficacy for the treatment of coronary artery disease. *Research Reports in Clinical Cardiology* 23 (2013).

106. XIENCE V and PROMUS P070015 approval letter. U.S. Food and Drug Administration, Center for Devices and Radiological Health. July 2, 2008. Retrieved March 27, 2015, from www.accessdata.fda.gov/cdrh_docs/pdf7/P070015a.pdf.

107. XIENCE nano P070015/S054 approval letter. U.S. Food and Drug Administration, Center for Devices and Radiological Health. May 24, 2011. Retrieved March 27, 2015, from www.accessdata.fda.gov/cdrh_docs/pdf7/P070015s054a.pdf.

108. XIENCE Xpedition, XIENCE Xpedition SV, XIENCE Xpedition LL, and XIENCE Alpine P070015/S122 approval letter. U.S. Food and Drug Administration, Center for Devices and Radiological Health. October 3, 2014. Retrieved March 27, 2015, from www.accessdata.fda.gov/cdrh_docs/pdf7/P070015s122a.pdf.

109. XIENCE PRIME and XIENCE PRIME LL P110019 approval letter. U.S. Food and Drug Administration, Center for Devices and Radiological Health. November 1, 2011. Retrieved March 27, 2015, from www.accessdata.fda.gov/cdrh_docs/pdf11/P110019a.pdf.

110. PROMUS Element P110010 approval letter. U.S. Food and Drug Administration, Center for Devices and Radiological Health. November 22, 2011. Retrieved March 27, 2015, from www.accessdata.fda.gov/cdrh_docs/pdf11/P110010a.pdf.

111. PROMUS Element Plus P110010/S001 approval letter. U.S. Food and Drug Administration, Center for Devices and Radiological Health. June 1, 2012. Retrieved March 27, 2015, from www.accessdata.fda.gov/cdrh_docs/pdf11/P110010s001a.pdf.

112. ION P100023 approval letter. U.S. Food and Drug Administration, Center for Devices and Radiological Health. April 22, 2011. Retrieved March 27, 2015, from www.accessdata.fda.gov/cdrh_docs/pdf10/P100023a.pdf.

113. Zilver PTX P100022 approval letter. U.S. Food and Drug Administration, Center for Devices and Radiological Health. November 14, 2012. Retrieved March 27, 2015, from www.accessdata.fda.gov/cdrh_docs/pdf10/P100022a.pdf.

114. Davis, J. R. *Nickel, cobalt, and their alloys*. (ASM International, 2000).

115. Montgomery, D. C. Using fractional factorial designs for robust process development. *Quality Engineering* **3,** 193–205 (1990).

116. Köhler, K., Coburn, J. W., Horne, D. E., Kay, E. & Keller, J. H. Plasma potentials of 13.56-MHz rf argon glow discharges in a planar system. *Journal of Applied Physics* **57,** 59 (1985).

117. Ishmaku, A. & Han, K. Characterization of cold-rolled and aged MP35N alloys. *Materials characterization* **47,** 139–148 (2001).

118. Bharadwaj, S. R., Tripathi, S. N. & Chandrasekharaiah, M. S. The Ir-Pt (iridium-platinum) system. *Journal of phase equilibria* **16,** 460–464 (1995).

119. Sigmund, P. A mechanism of surface micro-roughening by ion bombardment. *Journal of Materials Science* **8,** 1545–1553 (1973).

120. Jayapriya, J., Gopal, J., Ramamurthy, V., Kamachi Mudali, U. & Raj, B. Preparation and characterization of biocompatible carbon electrodes. *Composites Part B: Engineering* **43,** 1329–1335 (2012).

121. Bockris, J. O., Devanathan, M. A. V. & Muller, K. On the Structure of Charged Interfaces. *Proceedings of the Royal Society A: Mathematical, Physical and Engineering Sciences* **274,** 55–79 (1963).

122. Fedorov, M. V. & Kornyshev, A. A. Ionic Liquid Near a Charged Wall: Structure and Capacitance of Electrical Double Layer. *The Journal of Physical Chemistry B* **112,** 11868–11872 (2008).

123. Jaehyun, L., Mincheol, S., Chang-Guen, A., Chil Seong, A., Chan Woo, P. & Gun Yong, S. Effects of pH and Ion Concentration in Phosphate Buffer Solution on the Sensitivity of the Silicon Nanowire BioFETs. *Journal of the Korean Physical Society* **55,** 1621 (2009).

124. Vrouwenvelder, W. C. A., Groot, C. G. & de Groot, K. Histological and biochemical evaluation of osteoblasts cultured on bioactive glass, hydroxylapatite, titanium alloy, and stainless steel. *Journal of Biomedical Materials Research* **27,** 465–475 (1993).

125. Bordjih, K., Jouzeau, J.-Y., Mainard, D., Payan, E., Delagoutte, J.-P. & Netter, P. Evaluation of the effect of three surface treatments on the biocompatibility of 316L stainless steel using human differentiated cells. *Biomaterials* **17,** 491–500 (1996).

126. Ammar, A., Lagenaur, C. & Jannetta, P. Neural tissue compatibility of Teflon as an implant material for microvascular decompression. *Neurosurg. Rev.* **13,** 299–303 (1990).

127. Anglin, E. J., Cheng, L., Freeman, W. R. & Sailor, M. J. Porous silicon in drug delivery devices and materials. *Advanced Drug Delivery Reviews* **60,** 1266–1277 (2008).

128. Charnay, C., Bégu, S., Tourné-Péteilh, C., Nicole, L., Lerner, D. A. & Devoisselle, J. M. Inclusion of ibuprofen in mesoporous templated silica: drug loading and release property. *European Journal of Pharmaceutics and Biopharmaceutics* **57,** 533–540 (2004).

129. Li, Y. Y., Cunin, F., Link, J. R., Gao, T., Betts, R. E., Reiver, S. H., Chin, V., Bhatia, S. N. & Sailor, M. J. Polymer Replicas of Photonic Porous Silicon for Sensing and Drug Delivery Applications. *Science* **299,** 2045–2047 (2003).

130. Tourné-Péteilh, C., Lerner, D. A., Charnay, C., Nicole, L., Bégu, S. & Devoisselle, J.-M. The Potential of Ordered Mesoporous Silica for the Storage of Drugs: The Example of a Pentapeptide Encapsulated in a MSU-Tween 80. *ChemPhysChem* **4,** 281–286 (2003).

131. Wu, E. C., Park, J.-H., Park, J., Segal, E., Cunin, F. & Sailor, M. J. Oxidation-Triggered Release of Fluorescent Molecules or Drugs from Mesoporous Si Microparticles. *ACS Nano* **2,** 2401–2409 (2008).

132. Zilberman, M., Kraitzer, A., Grinberg, O. & Elsner, J. J. in *Drug Delivery* (ed. Schäfer-Korting, M.) **197,** 299–341 (Springer Berlin Heidelberg, 2010).

133. Arosarena, O. Tissue engineering. *Curr Opin Otolaryngol Head Neck Surg* **13,** 233–241 (2005).

134. Wang, X., Venkatraman, S. S., Boey, F. Y. C., Loo, J. S. C. & Tan, L. P. Controlled release of sirolimus from a multilayered PLGA stent matrix. *Biomaterials* **27,** 5588–5595 (2006).

135. Ma, X., Oyamada, S., Gao, F., Wu, T., Robich, M. P., Wu, H., Wang, X., Buchholz, B., McCarthy, S., Gu, Z., Bianchi, C. F., Sellke, F. W. & Laham, R. Paclitaxel/sirolimus combination coated drug-eluting stent: In vitro and in vivo drug release studies. *Journal of Pharmaceutical and Biomedical Analysis* **54,** 807–811 (2011).

136. Stone, G. W., Moses, J. W., Ellis, S. G., Schofer, J., Dawkins, K. D., Morice, M.-C., Colombo, A., Schampaert, E., Grube, E., Kirtane, A. J., Cutlip, D. E., Fahy, M., Pocock, S. J., Mehran, R. & Leon, M. B. Safety and efficacy of sirolimus- and paclitaxel-eluting coronary stents. *New England Journal of Medicine* **356,** 998–1008 (2007).

137. Kothwala, D., Raval, A., Choubey, A., Engineer, C. & Kotadia, H. Paclitaxel drug delivery from cardiovascular stent. *Trends in Biomaterials & Artificial Organs* **19,** 88–92 (2006).

138. Ranade, S. V., Miller, K. M., Richard, R. E., Chan, A. K., Allen, M. J. & Helmus, M. N. Physical characterization of controlled release of paclitaxel from the TAXUS Express2 drug-eluting stent. *Journal of Biomedical Materials Research* **71A,** 625–634 (2004).

139. Shih, C.-C., Shih, C.-M., Chou, K.-Y., Lin, S.-J. & Su, Y.-Y. Electrochemical Behavior of MP35N Implant Alloy in Simulated Physiological Media. *Journal of The Electrochemical Society* **153,** B403 (2006).